4-18-2022

Tuning Properties of Topological Insulators: An Ab-initio Approach

Karunya Shailesh Shirali
Louisiana State University and Agricultural and Mechanical College

TUNING PROPERTIES OF TOPOLOGICAL INSULATORS: AN AB-INITIO APPROACH

A Dissertation

Submitted to the Graduate Faculty of the
Louisiana State University and
Agricultural and Mechanical College
in partial fulfillment of the
requirements for the degree of
Doctor of Philosophy

in

The Department of Physics and Astronomy

by
Karunya Shailesh Shirali
Integrated BS-MS in Physics, Indian Institute of Science Education and Research
Thiruvananthapuram, 2016
May 2022

ACKNOWLEDGMENTS

I wouldn't be where I am today without the help and support of so many people. First, I would like to thank my parents for their constant support and love, for listening to my worries, and for giving me faith in the world, always.

I would also like to thank my advisors, Ilya Vekhter and William Shelton, for their mentoring and guidance over the years, and Daniel Sheehy, for his support and mentorship. I have learned a lot about research, including writing research papers, giving good presentations, and have grown and matured a lot from the time when I arrived at LSU, fresh from my undergrad; your training and help have been essential in this process.

My teachers at Rishi Valley have been a very big part of my formative years, and I would like to especially thank Sharada akka, Anu akka and Rajan sir, Sreekala akka and Ramachandran sir, Lata akka and Deshpande sir, Nirmala akka and Ramola sir, Meena akka and Sunil sir, Chandrika akka and Alok sir, Usha akka, Venki and Sid for all their support and helping me grow.

I would also like to thank my colleagues and friends at LSU, Mahmoud, David and Eklavya. I have learned so much from having discussions with you, and your friendship has been a huge source of support for me.

I am also grateful to so many dear friends for being there for me over the years, through the good times and the bad times. I am so lucky to have made friends like you, and you will always be important to me. Thank you Saranya, Radha, Ruchi, Anisha, Ashni, Samyuktha, Muhil, Sindhura, Rukma, Shashank. You have been an integral part of my life since my childhood. Ayushi, Vahini, Aditi and Trupti: my life at IISER and after would have been so different if I hadn't met you, and you have made it richer. Eklavya, Sudarsan, Vishal K, Erin, Utkarsh, Vijith, Arun, Ritwika, Stav, Aby, Anshu, Akhil, Soorya, Prerna, Vishal S, Kunal, Siddharth, Allyson and Fred: thank you for all the amazing time we've spent together and the discussions we've had; you've made my PhD experience and life in Baton Rouge and at LSU very fulfilling and made me feel cared for.

There are many others whose names I cannot possibly cover in this short thank you note: I am eternally grateful for your support, and hope to pay it forward in the future.

TABLE OF CONTENTS

LIST OF TABLES

LIST OF FIGURES

ABSTRACT

This thesis develops a first-principles based approach to explore the tuning of topological properties of the tetradymite topological insulators. We begin by setting up a framework to systematically obtain the bulk and surface properties of topological insulators, treating the structural and electronic properties on an equal footing. We determine a consistent method for including the van der Waals interactions, which are responsible for the weak coupling between sets of atomic layers in this family of layered materials, which is important in obtaining accurate structural properties. We obtain close agreement with experimental values for both the bulk and surface states.

To further establish the applicability of our methodology over a wide range of parameters, we study the effects of strain on the topological nature of this family of materials. We use the c/a anisotropy ratio of lattice constants as a parameter to investigate strain, and find that the chalcogenides Bi_2Se_3, Sb_2Se_3, Bi_2Te_3 and Sb_2Te_3 display topological phase transitions from topological to trivial insulating phases as the c/a ratio is varied. We show that the transitions in each material display common features and that they are primarily driven by the competition between the Coulomb repulsion and the van der Waals attraction between the outer atomic layers of the basic layered units which comprise these materials.

The success of our methodology drives us to investigate the effects of alloying disorder in these materials. We consider supercells, including those where the atomic correlations between dopants vanish up to the third nearest neighbor shell, and establish the existence of multiple topological phase transitions as a function of doping. We investigate the electronic structure of these alloys with different compositions across the phase diagram.

These findings establish our framework as a method of choice for predictive ab-initio calculations of topological electronic materials in bulk and in heterostructures. The first steps towards using it for topological interfaces are also described in this thesis.

CHAPTER 1.

INTRODUCTION

1.1 Topological insulators

Topological insulators (TIs) [1] are materials that have the special properties of being insulators in the bulk, and conducting electricity at their surfaces or edges. They have strong Spin-Orbit Coupling (SOC), in addition to inversion symmetry and time-reversal symmetry. In the prototypical 3D topological insulators, the hybridization and crystal-field splitting lead to two opposite-parity atom-derived energy levels being close to the chemical potential, and the SOC causes these two levels to interchange positions somewhere in the Brillouin zone, which leads to "band inversion" between the valence and conduction bands which are derived from these states. The bulk band inversion is critical to the topological properties of these materials, and it can be used as a signature of the topological nature. There have been significant developments in the field of topological insulators in the past two decades, starting from their prediction and the establishment of theoretical models which describe the bulk and surface states analytically [2, 3, 4, 5, 6, 7, 8], their subsequent experimental observation through conductivity and ARPES measurements [9, 10, 11, 12, 13, 14], to first-principles studies on TIs in different geometries. The experimental verification [15] of the exotic axion insulating state that was predicted generated considerable interest recently, and the synthesis of alloyed TIs [16] poses the possibility of investigating how disorder affects the topological properties. Many proposed applications of topological insulators involve fabricating heterostructures combining these materials with other topologically trivial compounds, and creatively controlling the spin-momentum locked symmetry-protected states at the interface between the two. While the structural constants of bulk materials can be measured experimentally, heterostructures are a different instance in which the lattice constants depend on the substrate, growing conditions, etc. The properties of TIs are known to depend on the structure [17, 18, 19, 20], and this calls for a methodology through which to self-consistently calculate the properties of these materials beyond simpler scenarios such as the bulk and vacuum surfaces. Additionally, some interactions that are known to have small energy scales compared to the bandwidths have important effects on the lattice structure, and call for a systematic analysis.

The unique, topology-protected properties of TIs have resulted in numerous proposals to use them in making electronics and quantum computers. They are considered a viable platform for realizing qubits and encoding quantum information because a particular symmetry that they possess, time reversal symmetry, in addition to the spin-orbit coupling, guarantees that their spins are locked in a specific manner to their momentum. While a metal has spin-degenerate states at each momentum, a TI has only one state at each momentum in general (except at the Time Reversal Invariant Momenta), meaning it has no state to scatter into. This reduces the possibility of impurities causing scattering and errors which could switch the qubit. Scientists have been engaged in a pursuit of observing the Majorana fermion, a type of particle that was predicted in 1937 to exist, but whose observation has been difficult. There have been exciting proposals for platforms consisting of heterostructures of TIs and superconductors where Majorana fermions are predicted to exist. If realized, pairs of

Majorana fermions could be used as qubits.

In spite of the tremendous progress that has been made, there are many important avenues that remain to be explored. Making use of TIs in quantum technologies requires the ability to manipulate the topological states, and an underlying theme to many proposals based on TIs is the need for ways to control properties such as the bulk band inversion, spin-momentum locking, Dirac velocity, etc. In this thesis, my goal was to study different methods of tuning the topological states in TIs. The first step was to accurately reproduce the properties of bulk and surface TIs in a computationally efficient and self-consistent manner using first-principles based Density Functional Theory calculations. Upon successfully characterizing the bulk and surfaces, I developed a comprehensive picture that serves as a reference and starting point and enables predictive use of ab initio methods for first-principles calculations on topological insulators. Since the lattice structure was found to play an important role on the electronic (and thus topological) properties, the next question that arose was: what happens if the structure is changed? The application of pressure/strain has been proposed as one method of controlling the topological properties [17, 18, 19, 20]. It can be induced by alloying or doping elements of different atomic sizes that give rise to chemical pressure[21, 22, 23, 24, 25, 26]. It modifies the hybridization of atomic levels and crystal-field strength, leaving the (atomic) SOC strength mostly unchanged and as a result, it may induce a transition between a topological and a trivial state. I used the ratio of the out-of-plane to in-plane lattice constants, c/a, as a tuning parameter and studied the topological phase transitions in Bi_2Se_3, Sb_2Se_3, Bi_2Te_3 and Sb_2Te_3. I found that the transitions in all four materials exhibited common features, and were primarily driven by competing Coulomb and van der Waals interactions in between the layered units forming these materials. The results from this work had important implications on alloying TIs. Disordered topological insulators have come into increased focus, partly due to their usefulness in tuning the Dirac point in bulk TIs that are naturally n or p-doped. First principles calculations on alloyed TIs such as $(Bi_{1-x}Sb_x)_2Se_3$ [27] have predicted a topological phase transition beyond a particular concentration of impurity atoms due to a reduction in the strength of Spin-Orbit Coupling. While they predicted a range of values for the critical impurity concentration, we sought to apply our framework of ab initio calculations and insight gained from studying the phase transitions in the ordered materials on how the lattice structure affects the topological nature, to the disordered systems and compare our results with experiments. Finally, the interface states of TI heterostructures are often assumed to be helical and isotropically dispersing, in resemblance to their counterparts at surfaces [28, 29], but theoretical models show that symmetry breaking at the interface leads to substantial modifications of the properties of topological states [30, 31]. In real systems such symmetry breaking interface potentials may originate from strain and stress due to lattice mismatch, broken bonds, buckling, and surface reconstruction. To gain a detailed understanding of the topological states at interfaces, we also investigated lattice-matched heterostructures which do not experience significant strain.

In summary, in this thesis, I systematically lay the groundwork for the tuning of topological states in TIs by first implementing a comprehensive framework to perform ab initio calculations of TIs, analyze and determine the dependence of the topological nature of the bulk materials on the lattice structure, identify the effects of alloying on the 3D TIs, and study the topological states at interfaces between TIs and topologically trivial materials. My results establish the foundation for future work in which topological states can be manipu-

lated in different ways geared towards device-engineering.

The rest of this thesis is organized as follows: Chapter 2 describes the concepts of topology and band theory, and Chapter 3 describes the basics of Density Functional Theory and the methods that I use. Chapter 4 summarizes the results of the investigation of different methods of including the van der Waals interactions in first-principles calculations on topological insulators. Chapter 5 describes the study of topological phase transitions in the chalcogenide TIs under the application of strain, and Chapter 6 summarizes the investigation of disorder in the 3D TIs. Chapter 7 describes the results of the study of lattice-matched heterostructures of TIs and topologically trivial materials.

CHAPTER 2.

TOPOLOGY AND BAND THEORY

The importance of topology in solid state physics is centered on certain numbers called topological invariants which are calculated using the wavefunctions of the system. The wavefunctions of periodic systems can be obtained by band theory, which is central to condensed matter physics, and is able to predict in many cases whether a material is insulating, semiconducting or conducting. Band theory has been around for almost a century and is well accepted. However, the concept of topology in condensed matter physics, which has become a subject of great interest especially in the past two decades, has added a new facet to band theory. This is surprising, as band theory was thought to have been established and set in stone. One of the first such areas in which it led to a new understanding was with reference to the quantum Hall effect, which is topological in the sense that it has fundamental properties that cannot be changed unless the system undergoes a quantum phase transition.

Band theory makes use of single particle quantum mechanics, where an assumption is made that the particles or quasiparticles in a system are mostly independent and do not interact with each other. The Hamiltonian matrix is an operator which describes the total energy of the system in terms of various relevant physical quantities such as the kinetic energy and potential energy. One can solve for the energy eigenvalues and eigenvectors of a given Hamiltonian matrix, which give us the single particle energies and wave functions. One can then assume that we fill each band with one of the many particles in the system, and thus arrive at the ground-state after having accounted for all the particles. Single particle states have the property that their tensor products can be used as a basis for the many particle Hilbert space. For fermions, which must have anti-symmetric wave functions, the many-particle fermionic wave function is written as an anti-symmetrized combination of the single particle wave functions. Note that this methodology ignores the 'correlations' in a system, and it cannot directly be used for strongly-correlated materials which have many-body interactions.

The application of concepts from topology to band theory in, say, insulators has revealed that there are distinct classes of insulators - those which are 'topological' and those which are 'trivial'. Topological insulators are insulators in the bulk, meaning that they have a bulk energy gap, and conduct electricity at their surfaces or edges, meaning that there is no energy gap in the surface states. In band theory, the understanding of a material being an insulator is that it has an energy gap between the highest occupied band and lowest unoccupied band. On the other hand, a conductor either has a partially filled highest occupied band, or has no energy gap separating the highest occupied band and lowest unoccupied band. Trivial insulators do not possess the property of gapless electronic states.

A large number of the TIs we currently know of do not have strong interactions. Additionally, the existence of the single particle bulk band gap in topological insulators bestows them with the property that adding electron-electron interactions in the system will not change the topological states drastically. This paves the way for TIs to be studied using band theory. It is also worth mentioning that it is this property that makes it convenient to study topological insulators via first-principles computational methods such as Density Functional Theory.

TIs have strong spin-orbit coupling and, in addition to other crystallographic symmetries, inversion symmetry and time-reversal symmetry. The bulk band structures are gapped and have a characteristic inverted band structure due to the strong spin-orbit coupling. The surface states are massless, linearly dispersing Dirac-like states. Time reversal symmetry imbues the spins of the topological surface states with a specific orientation with respect to their momenta, leading to a phenomenon known as helical spin-momentum locking. This property guarantees that electrons in these states will not scatter off non-magnetic impurities, into states with different momenta, at T = 0. Magnetic disorder, on the other hand, breaks time-reversal symmetry, and leads to the surface states becoming gapped and acquiring a mass. This has been confirmed in experiments, in which non-magnetic impurities do not change the Dirac cone dispersion [32], whereas magnetic atoms cause it to acquire a gap [33, 34]. While ordinary semiconductors also sometimes possess states localized near their surfaces, these states are not protected by any symmetries.

2.1 Bloch's theorem

In band theory, we often deal with translationally invariant systems, where there exists a unit cell that can describe the entire system through translations along a set of vectors known as the direct lattice vectors. There is also a set of vectors known as the reciprocal lattice vectors of the system that can be constructed from the direct lattice vectors. The reciprocal lattice vectors yield plane waves that have the periodicity of the direct lattice. A crystal momentum $\vec{k}$ can be defined and constructed from the reciprocal lattice vectors. Bloch's theorem [35] states that in such a translation invariant system, the single particle wave functions may be written as $|\psi(\vec{k})\rangle = e^{i\vec{k}\cdot\vec{r}}|u(\vec{k})\rangle$, where $|u(\vec{k})\rangle$ is an eigenstate of the Bloch Hamiltonian with the same periodicity as the crystal. The Bloch Hamiltonian $H(\vec{k})$ obeys the symmetry $H(\vec{k}) = H(\vec{k} + \vec{G})$, where $\vec{G}$ is a reciprocal lattice vector. The crystal momentum $\vec{k}$ can thus be confined to the first Brillouin zone, as $\vec{k}$ is equivalent to $\vec{k} + \vec{G}$. Diagonalizing the Bloch Hamiltonian yields the energy eigenvalues $E_n(\boldsymbol{k})$, where n is the band index. These are the energy bands, and they disperse with the wave vector $\vec{k}$.

The classification of materials into metals, insulators and semiconductors is made on the basis of the filling of bands. The number of particles in the system determines the position of the chemical potential, which is placed at the highest filled level. If the chemical potential passes through a band, the band is then partially filled, which means that the states near the chemical potential have unoccupied states accessible to them for conduction, and the material is classified a metal. On the other hand, if the chemical potential lies in between two levels which have a large separation, conduction is nearly impossible, and the material is likely to be an insulator. If the two bands above and below the chemical potential are not very far apart, the material is classified as a semiconductor.

2.2 Calculation of topological invariants

The topological classification of Hamiltonians is done by calculating the Berry phase [36] and Chern invariant of the system. One can define the Berry connection

$$\vec{A}_j = -i\langle u_j(\vec{k})|\nabla_{\vec{k}}|u_j(\vec{k})\rangle, \tag{2.1}$$

which is a function of the eigenstates $|u_j(\vec{k})\rangle$, where j is the band index, and $\vec{A}_j$ is similar to the electromagnetic vector potential.

Thus, we can use Stokes' theorem to obtain the Berry phase over a closed contour C

$$\gamma_{j,C} = \oint_C \vec{A}_j \cdot d\vec{k} = \int \mathcal{F}_j d^2\vec{k}, \tag{2.2}$$

where $\mathcal{F}_j = \nabla \times \vec{A}_j$ is the Berry curvature.

Under a gauge transformation, $|u_j(\vec{k})\rangle \to e^{i\phi(\vec{k})}|u_j(\vec{k})\rangle$, where $\phi(\vec{k})$ is a real function of $\vec{k}$, and we see that the Berry connection transforms as $\vec{A}_j \to \vec{A}_j + \nabla_{\vec{k}}\phi(\vec{k})$. The Berry phase, on the other hand, is unchanged and thus gauge invariant.

We can then define the Chern invariant or the Chern number

$$n_j = \frac{1}{2\pi}\int_S \mathcal{F}_j d^2\vec{k}, \tag{2.3}$$

where the integral above is carried out over the entire first Brillouin zone, for the occupied bands. Thus, for an insulator, the integral would be for the valence band, over the Brillouin zone. On the other hand, a metal, whose highest occupied level is partially occupied, does not have a well-defined Chern number.

The Chern number is quantized, and a non-zero Chern number implies that the band for which it is calculated is topologically non-trivial. The total Chern number of the system is calculated as the sum of the Chern numbers of all the occupied bands

$$n = \sum_{j=1}^{N} n_j. \tag{2.4}$$

TIs belong to a class of materials, "topological" materials, that have come into focus due to their characteristic of having symmetry-protected properties. The statement of bulk-boundary correspondence makes use of these attributes, and relates certain properties of the bulk, known as bulk topological invariants, with robust gapless states localized at the surfaces or edges of the TI that are topologically protected. By the principle of adiabatic continuity, we infer that if we are able to continuously vary the parameters in the Hamiltonian between one insulating system to another, without closing the bulk energy gap, the two insulators are topologically equivalent. On the other hand, if, in such a process, the bulk energy gap closes for some value of the parameters, a quantum phase transition must occur.

The implication of the bulk-boundary correspondence is that the Chern invariant changes at surfaces and interfaces of TIs, where the vacuum (in case of a surface) or the adjacent material (for an interface) can be thought of as a material for which there is a sudden change in the Hamiltonian (when we start from the TI Hamiltonian), and there is no adiabatic transformation that can change one into the other. In this case, the change in the Chern invariant necessitates the existence of gapless conducting states which are bound to the region where it changes, and is also equal to the number of surface/interface states. The Hall conductivity of a system is proportional to the Chern number of the occupied bands.

TIs of different dimensionalities have been discovered experimentally. The first materials that were predicted to be topological insulators included $Bi_{1-x}Sb_x$ and strained HgTe [6],

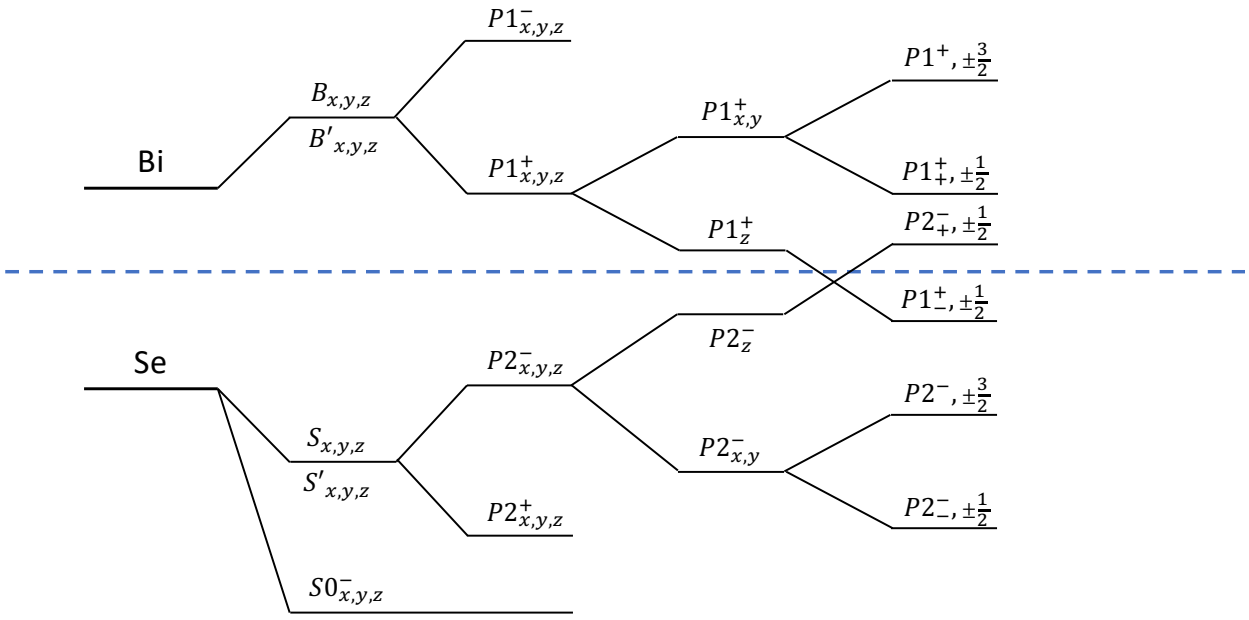

Figure 2.1. Schematic picture of the energy levels in the 3D TIs, starting from the atom-derived states, adapted from Ref. [8]. The various stages represent the effects of atomic hybridization, the formation of parity eigenstates, the crystal-field splitting, and finally the spin-orbit coupling.

and these predictions were confirmed soon after [11, 9]. HgTe/CdTe quantum wells were one of the first two-dimensional thin film TIs to be discovered. The bismuth chalcogenides Bi_2Se_3 and Bi_2Te_3 were the next materials to be confirmed to be TIs, and are the prototypical three-dimensional TIs. Bi_2Se_3 in particular has a large band gap of ~ 0.3 eV, which is equivalent to a temperature of ~ 3600 K, which makes it suitable for room temperature applications, and the Dirac cone in Bi_2Se_3 has been observed at temperatures of 300 K [13], supporting this. Incidentally, Bi_2Te_3 is well known due to its excellent thermoelectric properties and has been used in various cryogenic devices.

The main structural unit of the prototypical 3D TIs of the Bi_2X_3 (X=Se,Te) family is a "quintuple layer" (QL) X′−Bi−X−Bi−X′, where each atom represents a layer, and the respective pairs of X′ and Bi positions are related through inversion symmetry. Since each QL effectively has a "closed shell" [37], the coupling between QLs is believed to be largely due to van der Waals forces.

2.3 Model Hamiltonian

The 3D BHZ model Hamiltonian for TIs such as Bi_2X_3 (X=Se,Te) was developed in 2009 [8]. Starting from the atomic energy levels the authors inferred that the low-lying energy states

consisted of the p orbitals of Bi and Se, see Fig. 2.1. Next, taking into account the effects of atomic orbital hybridization and crystal field splitting, the authors found that the states with energies closest to the Fermi energy were $|P1_z^+\rangle$and $|P2_z^-\rangle$, where the P's are linear combinations of the p_z orbitals, and the superscripts $\pm$ refer to the parity. Finally, the SOC induces an inversion between these two states at the Γ point, and the states are now labeled as $|P1_z^+,+\frac{1}{2}\rangle, |P2_z^-,+\frac{1}{2}\rangle, |P1_z^+,-\frac{1}{2}\rangle, |P2_z^-,-\frac{1}{2}\rangle$ (the $\pm\frac{1}{2}$ refers to the total angular momentum). Since $j=\pm\frac{1}{2}$, it can be treated as a pseudo-spin. In matrix form, the Hamiltonian can be written as

$$H_0' = \epsilon_0(\vec{k})\mathbb{I}_{4x4} + \begin{pmatrix} \mathcal{M}(\vec{k}) & -iA_1k_z & 0 & iA_2k_- \\ iA_1k_z & -\mathcal{M}(\vec{k}) & iA_2k_- & 0 \\ 0 & -iA_2k_+ & \mathcal{M}(\vec{k}) & -iA_1k_z \\ -iA_2k_+ & 0 & iA_1k_z & -\mathcal{M}(\vec{k}) \end{pmatrix}, \tag{2.5}$$

where $k_\pm = k_x \pm ik_y$, $\epsilon_0(\vec{k}) = C + D_1k_z^2 + D_2k_\perp^2$, $\mathcal{M}(\vec{k}) = M - B_1k_z^2 - B_2k_\perp^2$, and $k_\perp^2 = k_x^2 + k_y^2$. The basis is $(|P1_z^+,+\frac{1}{2}\rangle, |P2_z^-,+\frac{1}{2}\rangle, |P1_z^+,-\frac{1}{2}\rangle, |P2_z^-,-\frac{1}{2}\rangle)$.

The parameters $A_1, A_2, C, D_1, D_2, M, B_1$ and B_2 are material-dependent, and have been estimated for Bi_2Se_3 and Bi_2Te_3. It has been shown [38] that the spin operators S_x, S_y, S_z are proportional to the matrices $\sigma_x, \sigma_y, \sigma_z$, so that the real spin is proportional to the expectation value of $\vec{\sigma}$. Thus, the A_2 terms, which can be written as $A_2(k_y\sigma_x - k_x\sigma_y)\otimes\tau_x$, represent the spin-orbit coupling, where σ represents the spin degree of freedom and τ represents the orbital degree of freedom. The Hamiltonian H_0' may be written concisely in terms of the σ and τ matrices as

$$H_0' = \mathcal{M}(\boldsymbol{k})\mathbb{I}\otimes\tau_z + A_1k_z\mathbb{I}\otimes\tau_y + A_2(\sigma_xk_y - \sigma_yk_x)\otimes\tau_x, \tag{2.6}$$

where $\mathcal{M}(\boldsymbol{k}) = M - B_1k_z^2 - B_2k_\perp^2$, and the $\epsilon_0(\boldsymbol{k})$ term has been discarded.

The Schrödinger equation $H_0'(\vec{k})|\psi(\vec{k})\rangle = E(\vec{k})|\psi(\vec{k})\rangle$ for the BHZ model Hamiltonian can be solved to obtain bulk bands with an energy gap and gapless surface states by applying the appropriate boundary conditions. When solving the Schrödinger equation, an assumption is usually made that $\epsilon_0(\vec{k})$ is zero.

To find the bulk energy dispersion, we diagonalize the Hamiltonian, and obtain two energy levels

$$E_{bulk} = \pm\sqrt{A_2^2k_\perp^2 + A_1^2k_z^2 + (B_2k_\perp^2 + B_1k_z^2 - M)^2}, \tag{2.7}$$

each of which is doubly degenerate. Note that the time-reversal operator $\mathcal{T} = i\sigma_y\mathbb{C}\otimes\tau_0$, where $\mathbb{C}$ is the complex conjugation operator. $\mathcal{T}$ commutes with the Hamiltonian H_0'. The Kramers degeneracy theorem guarantees that since we have a time-reversal symmetric system of spin-$\frac{1}{2}$ fermions, each energy is doubly degenerate. Two of the eigenvectors are

$$\psi_{1,-}(\vec{k}) = C_{1,-}\begin{pmatrix} i(M - B_2(k_x+k_y)^2 - B_1k_z^2 - \sqrt{A_2^2(k_x^2+k_y^2) + A_1^2k_z^2 + (B_2(k_x+k_y)^2 + B_1k_z^2 - M)^2}) \\ -A_1k_z \\ 0 \\ A_2k_+ \end{pmatrix}, \tag{2.8}$$

and

$$\psi_{1,+}(\vec{k}) = C_{1,+}\begin{pmatrix} i(M - B_2(k_x+k_y)^2 - B_1k_z^2 + \sqrt{A_2^2(k_x^2+k_y^2) + A_1^2k_z^2 + (B_2(k_x+k_y)^2 + B_1k_z^2 - M)^2}) \\ -A_1k_z \\ 0 \\ A_2k_+ \end{pmatrix}, \tag{2.9}$$

where C's are normalization constants, and the $\pm$ in their subscripts refers to the sign of the energy eigenvalue.

The other two eigenvectors are

$$\psi_{2,-}(\vec{k}) = C_{2,-}\begin{pmatrix} A_1k_z \\ -i(M - B_2(k_x+k_y)^2 - B_1k_z^2 + \sqrt{A_2^2(k_x^2+k_y^2) + A_1^2k_z^2 + (B_2(k_x+k_y)^2 + B_1k_z^2 - M)^2}) \\ A_2k_+ \\ 0 \end{pmatrix}, \tag{2.10}$$

and

$$\psi_{2,+}(\vec{k}) = C_{2,+}\begin{pmatrix} A_1k_z \\ -i(M - B_2(k_x+k_y)^2 - B_1k_z^2 - \sqrt{A_2^2(k_x^2+k_y^2) + A_1^2k_z^2 + (B_2(k_x+k_y)^2 + B_1k_z^2 - M)^2}) \\ A_2k_+ \\ 0 \end{pmatrix}. \tag{2.11}$$

Here, $\psi_{1,-}$ and $\psi_{2,-}$ are Kramers pairs, as are $\psi_{1,+}$ and $\psi_{2,+}$.

Let us look at the behavior of the two eigenvectors at the limits $k \to 0$ and $k \to \infty$.

In the limit $k \to 0$

$$\psi_{1,-}(k \to 0) = C_{1,-}\begin{pmatrix} i(M - |M|) \\ -A_1k_z \\ 0 \\ A_2k_+ \end{pmatrix} \text{ and } \psi_{1,+}(k \to 0) = C_{1,+}\begin{pmatrix} i(M + |M|) \\ -A_1k_z \\ 0 \\ A_2k_+ \end{pmatrix}. \tag{2.12}$$

In the limit $k \to \infty$

$$\psi_{1,-}(k \to \infty) = C_{1,-}\begin{pmatrix} i(-B_2(k_x+k_y)^2 - B_1k_z^2 - |B_2(k_x+k_y)^2 + B_1k_z^2|) \\ -A_1k_z \\ 0 \\ A_2k_+ \end{pmatrix}, \tag{2.13}$$

and

$$\psi_{1,+}(k\to\infty) = C_{1,+}\begin{pmatrix} i(-B_2(k_x+k_y)^2 - B_1k_z^2 + |B_2(k_x+k_y)^2 + B_1k_z^2|) \\ -A_1k_z \\ 0 \\ A_2k_+ \end{pmatrix}. \tag{2.14}$$

We can set $k_z = 0$ to obtain a simplified scenario.

$$\psi_{1,-}(k\to 0) = C_{1,-}\begin{pmatrix} i(M-|M|) \\ 0 \\ 0 \\ A_2k_+ \end{pmatrix}, \quad \psi_{1,+}(k\to 0) = C_{1,+}\begin{pmatrix} i(M+|M|) \\ 0 \\ 0 \\ A_2k_+ \end{pmatrix}, \tag{2.15}$$

$$\psi_{1,-}(k\to\infty) = C_{1,-}\begin{pmatrix} i((-B_2-|B_2|)(k_x+k_y)^2 \\ 0 \\ 0 \\ A_2k_+ \end{pmatrix}, \tag{2.16}$$

and

$$\psi_{1,+}(k\to\infty) = C_{1,+}\begin{pmatrix} i((-B_2+|B_2|)(k_x+k_y)^2 \\ 0 \\ 0 \\ A_2k_+ \end{pmatrix}. \tag{2.17}$$

Now consider the quantity MB_2, and say we want $MB_2 > 0$. If $M < 0$

$$\psi_{1,-}(k\to 0) = \begin{pmatrix} 1 \\ 0 \\ 0 \\ 0 \end{pmatrix} \text{ and } \psi_{1,+}(k\to 0) = \begin{pmatrix} 0 \\ 0 \\ 0 \\ 1 \end{pmatrix}. \tag{2.18}$$

Now, considering $B_2 < 0$ so that $MB_2 > 0$

$$\psi_{1,-}(k\to\infty) = \begin{pmatrix} 0 \\ 0 \\ 0 \\ 1 \end{pmatrix} \text{ and } \psi_{1,+}(k\to\infty) = \begin{pmatrix} 1 \\ 0 \\ 0 \\ 0 \end{pmatrix}. \tag{2.19}$$

Thus, we can see that the forms of $\psi_{1,-}$ and $\psi_{1,+}$ switch as k goes from 0 to ∞, a feature that is known as band inversion. We can interpret this as the eigenstates experiencing a winding as k goes from 0 to ∞, which makes this regime ($MB_2 > 0$) topologically nontrivial.

It is worth mentioning here that upon setting $k_z = 0$ in Eqs. (2.8), (2.9), (2.10) and (2.11), it is easy to see that the Kramers pairs $\psi_{1,-}$ ($\psi_{1,+}$) and $\psi_{2,-}$ ($\psi_{2,+}$) exist in different subspaces of the Hilbert space. This ensures that the Kramers pair of eigenstates $\psi_{1,-}$ ($\psi_{1,+}$) and $\psi_{2,-}$ ($\psi_{2,+}$) are not simply exchanging forms as k goes from 0 to ∞, and that there is actually a winding of the wave function.

On the other hand, if we consider $B_2 > 0$ so that $MB_2 < 0$

$$\psi_{1,-}(k \to \infty) = \begin{pmatrix} 1 \\ 0 \\ 0 \\ 0 \end{pmatrix} \text{ and } \psi_{1,+}(k \to \infty) = \begin{pmatrix} 0 \\ 0 \\ 0 \\ 1 \end{pmatrix}, \tag{2.20}$$

and so ψ_- and ψ_+ retain the same form as k goes from 0 to ∞, without band inversion. This is a topologically trivial regime.

We next turn to the slab geometry. We will consider a slab whose surface lies perpendicular to the z axis. Because of these boundary conditions, we must replace the momentum operator along the z direction with its derivative form, $-i\partial_z$.

Let us first consider the helicity operator $\hat{h}$.

$$\hat{\boldsymbol{h}} = \frac{(\boldsymbol{\sigma} \times \boldsymbol{k})_z}{k} \otimes \tau_0 = (\sigma_x k_y - \sigma_y k_x) \otimes \tau_0 = \begin{pmatrix} 0 & ie^{i\theta} \\ -ie^{i\theta} & 0 \end{pmatrix} \otimes \tau_0, \tag{2.21}$$

where k is the momentum in the k_x, k_y plane and $\tan\theta = \frac{k_y}{k_x}$.

The eigenvectors of $\hat{h}$ in the σ subspace are

$$\psi_{h,+} = \frac{1}{\sqrt{2}} \begin{pmatrix} i \\ e^{i\theta} \end{pmatrix}, \text{ and } \psi_{h,-} = \frac{1}{\sqrt{2}} \begin{pmatrix} i \\ -e^{i\theta} \end{pmatrix}. \tag{2.22}$$

For simplicity, we write them as

$$\psi_{h,\eta} = \frac{1}{\sqrt{2}} \begin{pmatrix} i \\ \eta e^{i\theta} \end{pmatrix}. \tag{2.23}$$

Now, we note that because the helicity operator $\hat{h}$ commutes with the Hamiltonian H_0', we can choose to write the eigenvectors of H_0' in terms of the eigenvectors of $\hat{h}$. Taking into account the boundary condition in the z direction which necessitates the wave function Ψ vanishing at $z = 0$, i.e. $\Psi(0) = 0$, and the fact that we are looking for solutions to the system that decay exponentially away from $z = 0$, we may write a general eigenvector of H_0' in the form

$$\psi_\eta = a(\boldsymbol{k})e^{\lambda z} \begin{pmatrix} i \\ \eta e^{i\theta} \end{pmatrix} \otimes \begin{pmatrix} 1 \\ 0 \end{pmatrix} + b(\boldsymbol{k})e^{\lambda z} \begin{pmatrix} i \\ \eta e^{i\theta} \end{pmatrix} \otimes \begin{pmatrix} 0 \\ 1 \end{pmatrix} = \begin{pmatrix} ia(\boldsymbol{k}) \\ ib(\boldsymbol{k}) \\ \eta a(\boldsymbol{k})e^{i\theta} \\ \eta b(\boldsymbol{k})e^{i\theta} \end{pmatrix} e^{\lambda z}. \tag{2.24}$$

We then write the Schrödinger equation

$$\begin{pmatrix} \mathcal{M}(\boldsymbol{k}) & -A_1\partial_z & 0 & iA_2k_- \\ A_1\partial_z & -\mathcal{M}(\boldsymbol{k}) & iA_2k_- & 0 \\ 0 & -iA_2k_+ & \mathcal{M}(\boldsymbol{k}) & -A_1\partial_z \\ -iA_2k_+ & 0 & A_1\partial_z & -\mathcal{M}(\boldsymbol{k}) \end{pmatrix} \begin{pmatrix} ia(\boldsymbol{k}) \\ ib(\boldsymbol{k}) \\ \eta a(\boldsymbol{k})e^{i\theta} \\ \eta b(\boldsymbol{k})e^{i\theta} \end{pmatrix} e^{\lambda z} = E_\eta(k) \begin{pmatrix} ia(\boldsymbol{k}) \\ ib(\boldsymbol{k}) \\ \eta a(\boldsymbol{k})e^{i\theta} \\ \eta b(\boldsymbol{k})e^{i\theta} \end{pmatrix} e^{\lambda z}. \tag{2.25}$$

This can be rewritten as

$$\begin{pmatrix} \mathcal{M}_\lambda(\boldsymbol{k}) - E_\eta(k) & -A_1\lambda & 0 & iA_2ke^{-i\theta} \\ A_1\lambda & -\mathcal{M}_\lambda(\boldsymbol{k}) - E_\eta(k) & iA_2ke^{-i\theta} & 0 \\ 0 & -iA_2ke^{i\theta} & \mathcal{M}_\lambda(\boldsymbol{k}) - E_\eta(k) & -A_1\lambda \\ -iA_2ke^{i\theta} & 0 & A_1\lambda & -\mathcal{M}_\lambda(\boldsymbol{k}) - E_\eta(k) \end{pmatrix} \begin{pmatrix} ia(\boldsymbol{k}) \\ ib(\boldsymbol{k}) \\ \eta a(\boldsymbol{k})e^{i\theta} \\ \eta b(\boldsymbol{k})e^{i\theta} \end{pmatrix} = 0, \tag{2.26}$$

where $\mathcal{M}_\lambda(\boldsymbol{k}) = M + B_1\lambda^2 - B_2k^2$.

We obtain the set of coupled equations

$$[\mathcal{M}_\lambda(\boldsymbol{k}) - E_\eta(k)]\, ia(\boldsymbol{k}) + [i\eta A_2k - iA_1\lambda]\, b(\boldsymbol{k}) = 0, \tag{2.27}$$

$$[iA_1\lambda + iA_2\eta k]\, a(\boldsymbol{k}) - [\mathcal{M}_\lambda(\boldsymbol{k}) + E_\eta(k)]\, ib(\boldsymbol{k}) = 0, \tag{2.28}$$

and, combining the two, arrive at an equation for the energy

$$E_\eta^2(k) = \mathcal{M}_\lambda^2(k) + A_2^2k^2 - A_1^2\lambda^2. \tag{2.29}$$

Thus

$$a(k) = \mathcal{M}_\lambda(k) + E_\eta(k), \tag{2.30}$$

$$b(k) = A_1\lambda + A_2\eta k, \tag{2.31}$$

is a solution for a and b.

The eigenvectors can be written as

$$\psi_{\eta,\lambda}(k) = \begin{pmatrix} i(\mathcal{M}_\lambda(k) + E_\eta(k)) \\ i(A_1\lambda + A_2\eta k) \\ \eta(\mathcal{M}_\lambda(k) + E_\eta(k))e^{i\theta} \\ \eta(A_1\lambda + A_2\eta k)e^{i\theta} \end{pmatrix} e^{\lambda z}. \tag{2.32}$$

Imposing the boundary condition on the wave function will now allow us to find an expression for λ. First, let us look at the equation for λ. It is

$$E_\eta^2(k) = (M + B_1\lambda^2 - B_2k^2)^2 + A_2^2k^2 - A_1^2\lambda^2. \tag{2.33}$$

$$\implies 0 = (B_1^2)\lambda^4 + (2B_1(M - B_2k^2) - A_1^2)\lambda^2 + (M - B_2k^2)^2 + A_2^2k^2 - E_\eta^2(k). \tag{2.34}$$

Thus,

$$\lambda^2 = \frac{-(2B_1(M - B_2k^2) - A_1^2) \pm \sqrt{(2B_1(M - B_2k^2) - A_1^2)^2 - 4(B_1^2)((M - B_2k^2)^2 + A_2^2k^2 - E_\eta^2(k))}}{2B_1^2} \tag{2.35}$$

Notice that this is a quadratic equation in λ^2. Setting $k = 0, E = 0$ in the equation above leaves us with

$$\lambda^2 = \frac{-(2B_1M - A_1^2) \pm \sqrt{(2B_1M - A_1^2)^2 - 4B_1^2M^2}}{2B_1^2} = \frac{(A_1^2 - 2B_1M) \pm A_1\sqrt{A_1^2 - 4MB_1}}{2B_1^2}. \tag{2.36}$$

The roots of this equation are

$$\lambda = \pm \frac{A_1 \pm \sqrt{A_1^2 - 4B_1 M}}{2B_1}. \tag{2.37}$$

For the topological surface states to exist, i.e., for the wave function to be normalizable and for the boundary condition to be satisfied, the values of λ must both have negative real parts or both have positive real parts, depending on the boundary condition. For this to be true, the absolute value of the quantity under the square root must be less than $|A_1|$. This imposes the condition that $MB_1 > 0$, and ensures normalizability. For example, if the material exists for $z > 0$, both the λ's must have negative real parts.

Thus, in this case and more generally, λ^2 will have two roots, which could be either real or complex, depending on the coefficients. If they are real, then λ will have two real negative and two real positive roots. If the solutions for λ^2 are complex, they must be complex conjugate numbers, and hence their square roots, λ, will also consist of complex conjugate numbers. The real parts of these roots will always consist of two positive and two negative numbers. Thus, depending on how we set up our system, we will be able to construct the wave function by choosing the two roots which lead to its exponential decay in the material. Let us say that we choose the material to exist for $z > 0$, and its surface to lie at $z = 0$. We choose the two roots for λ which have negative real parts, and label them $\lambda_{1,2}$.

We can then construct the wave function as a linear combination

$$\Psi(z) = \sum_\alpha C_\alpha \psi_{\eta,\lambda_\alpha}(k) = C_1 \begin{pmatrix} i(\mathcal{M}_{\lambda_1}(k) + E_\eta(k)) \\ i(A_1\lambda_1 + A_2\eta k) \\ \eta(\mathcal{M}_{\lambda_1}(k) + E_\eta(k))e^{i\theta} \\ \eta(A_1\lambda_1 + A_2\eta k)e^{i\theta} \end{pmatrix} e^{\lambda_1 z} + C_2 \begin{pmatrix} i(\mathcal{M}_{\lambda_2}(k) + E_\eta(k)) \\ i(A_1\lambda_2 + A_2\eta k) \\ \eta(\mathcal{M}_{\lambda_2}(k) + E_\eta(k))e^{i\theta} \\ \eta(A_1\lambda_2 + A_2\eta k)e^{i\theta} \end{pmatrix} e^{\lambda_2 z}, \tag{2.38}$$

which has the boundary condition $\Psi(0) = 0$. This leads to the equation determining the coefficients C_α:

$$\begin{vmatrix} \mathcal{M}_{\lambda_1}(k) + E_\eta(k) & \mathcal{M}_{\lambda_2}(k) + E_\eta(k) \\ A_1\lambda_1 + A_2\eta k & A_1\lambda_2 + A_2\eta k \end{vmatrix} = 0, \tag{2.39}$$

A solution of the above equation is

$$E_\eta(k) = A_2\eta k \text{ and } \mathcal{M}_{\lambda(k)} = A_1\lambda, \tag{2.40}$$

$$\text{and } E_\eta(k) = -A_2\eta k \text{ and } \mathcal{M}_{\lambda(k)} = -A_1\lambda. \tag{2.41}$$

Thus, we obtain linearly dispersing surface states, where E depends linearly on k. Note that in deriving these states, we had assumed that the solutions were made up of the eigenstates of the helicity operator, and the surface states we have derived are hence helical. The states we have obtained are for a surface, where the TI is adjacent to vacuum. However, an analogy can be made with cases in which the TI has an interface with a topologically trivial (or non-topological) material. In that case, an argument can be made that since the adjacent material is not topological, the bulk topological invariant, i.e. the Chern number, goes to zero across the boundary, and there must be gapless states at the interface. The boundary condition in this case is that the particle current across the interface must be

conserved. However, a loss of translational invariance at the interface can lead to even more complicated boundary conditions such as having to solve the Poisson equation.

With the existence of theoretical models such as the BHZ model which can accurately describe the low energy physics in TI structures, one might ask why we turn to computational techniques to approach such problems. The reason is partly that the BHZ model is a long wavelength $\vec{k} \cdot \vec{p}$ model that describes the system near the Γ point; however, we know that the band inversion is due to the difference in parities of the wavefunctions at the center and edge of the Brillouin zone. Thus, using DFT ensures that we have a good understanding of the physics throughout the Brillouin zone, including the edges. Additionally, another advantage of using DFT lies in the scaling with system size. DFT is able to provide a good tradeoff between the cost of computation and the precision of the results. For interface calculations, the number of electrons in a system can easily be in the thousands. The scalability is another reason why we don't use more accurate computational methods which are much more computationally expensive. Finally, analytical solutions of the interface problem can require solving complicated differential equations, which is another reason why DFT is advantageous.

CHAPTER 3.

METHODOLOGY

3.1 Density Functional Theory

Density Functional Theory (DFT) is a first-principles technique through which the physical, chemical and electronic properties of a material can be studied via numerical calculations. Walter Kohn was awarded the Nobel Prize in Chemistry in 1998 "for his development of the density-functional theory" along with John A. Pople "for his development of computational methods in quantum chemistry." DFT is a quantum mechanical approach which finds and uses the ground-state electron density to calculate various ground-state properties of systems of many electrons. The Kohn-Sham equations [39] transform the many-body problem into a set of single-particle noninteracting equations that all experience a common effective potential and need to be solved self-consistently. The many-body effects are grouped into a term known as the exchange-correlation functional. While DFT is an exact theory, in practice, the exact form of the exchange-correlation functional is not known, and must be approximated in some way. There are a number of exchange-correlation functionals available which describe the potential in the system to varying accuracies. The most common of these are the Local Density Approximation (LDA) and the Generalized Gradient Approximation (GGA), which include terms depending on the electron density and additionally the gradient of the electron density, respectively.

To gain a basic understanding of DFT, we describe below the formulation of the Kohn-Sham equations.

The many-body Hamiltonian is given by

$$\hat{H}_{MB} = -\sum_i \frac{\hbar^2}{2m_e}\nabla^2_{\vec{r}_i} - \sum_I \frac{\hbar^2}{2M_I}\nabla^2_{\vec{R}_I} + \frac{1}{2}\sum_{i\neq j}\frac{e^2}{|\vec{r}_i - \vec{r}_j|} - \sum_{i,I}\frac{Z_I e^2}{|\vec{r}_i - \vec{R}_I|} + \frac{1}{2}\sum_{I\neq J}\frac{Z_I Z_J e^2}{|\vec{R}_I - \vec{R}_J|}, \tag{3.1}$$

where the first two terms represent the kinetic energy of the electrons and nuclei, and the third, fourth and fifth terms represent the Coulomb interaction between electrons, between electrons and nuclei, and between nuclei respectively. m_e is the electron mass, $\hbar$ is the reduced Planck constant, M_I is the mass of the I^{th} nucleus, e is the electron charge, Z_I is the atomic number of the I^{th} nucleus, and $\vec{r}_i, \vec{R}_I$ are the locations of the i^{th} electron and I^{th} nucleus respectively. Upon applying the Born-Oppenheimer approximation which assumes that the nuclear motion is much smaller than the electronic motion because of the much larger nuclear mass, we arrive at the simplified Hamiltonian

$$\hat{H} = -\sum_i \frac{\hbar^2}{2m_e}\nabla^2_{\vec{r}_i} + \frac{1}{2}\sum_{i\neq j}\frac{e^2}{|\vec{r}_i - \vec{r}_j|} - \sum_{i,I}\frac{Z_I e^2}{|\vec{r}_i - \vec{R}_I|} + \frac{1}{2}\sum_{I\neq J}\frac{Z_I Z_J e^2}{|\vec{R}_I - \vec{R}_J|}. \tag{3.2}$$

Here we can set

$$V_{ext}(\vec{r}) = -\sum_I \frac{Z_I e^2}{|\vec{r} - \vec{R}_I|}, \tag{3.3}$$

as the potential that the electrons experience. It is considered as an external potential because the nuclei positions are now taken as external parameters in the system. We can

then write

$$\hat{H} = -\sum_i \frac{\hbar^2}{2m_e}\nabla^2_{\vec{r}_i} - \sum_i V_{ext}(\vec{r}_i) + \frac{1}{2}\sum_{i\neq j}\frac{e^2}{|\vec{r}_i - \vec{r}_j|} + E_{II}, \tag{3.4}$$

where E_{II} is the electrostatic interaction energy of the different nuclei.

The two central theorems of DFT are the Hohenberg-Kohn theorems [40]. The first theorem states that for an interacting system of electrons in an external potential $V_{ext}(\vec{r})$, apart from a trivial additive constant, the potential $V_{ext}(\vec{r})$ may be determined uniquely using the ground-state electron density $n_0(\vec{r})$.

The second theorem states that a universal functional $F[n]$ consisting of the kinetic energy and Coulomb interaction exists, independent of $V_{ext}(\vec{r})$, such that the energy functional $E[n]$

$$E[n] = F[n] + \int V_{ext}(\vec{r})n(\vec{r})d^3r + E_{II}, \tag{3.5}$$

where $E[n]$ has the properties that, for all densities $n(\vec{r})$ such that $\int n(\vec{r})d^3r = N$ (the number of electrons), $E[n]$ has a global minimum when $n(\vec{r})$ is the exact ground-state density; additionally, this minimum energy is the exact ground-state energy.

The implication of the first theorem is that for a given external potential $V_{ext}(\vec{r})$, the ground-state electron density is uniquely determined, and instead of having to use the many-body wave function, which depends on $3N$ coordinates, the ground-state properties can all be obtained using the ground-state electron density, which only depends on 3 coordinates. The second theorem relates to the variational principle that is used for the ground-state energy. It states that, starting with the energy functional $E[n]$, the exact ground-state density and exact ground-state energy can always be found via minimization.

The Kohn-Sham scheme [39] then asserts that the ground-state properties of an interacting many-electron system can be obtained by representing the ground-state density of this system as a ground-state density of an effective noninteracting system of electrons. The solution of this latter system will allow us to find the ground-state properties of the original system.

Let us consider a noninteracting system of N electrons. The most general Hamiltonian can be written as

$$H_{noninteracting} = -\frac{\hbar^2}{2m_e}\nabla^2 + V_{KS}(\boldsymbol{r}). \tag{3.6}$$

Here, V_{KS}, the Kohn-Sham potential, is chosen so that the ground-state electron density of this system is equal to the ground-state electron density of the interacting many-electron system. Letting the energy eigenvectors be labeled by $\phi_i(\boldsymbol{r})$, and the eigenvalues by ϵ_i, we can write the ground-state electron density as

$$n_0(\boldsymbol{r}) = \sum_{i=1}^{N} |\phi_i(\boldsymbol{r})|^2, \tag{3.7}$$

where N is the number of electrons.

Similarly, we can write the kinetic energy and Hartree energy

$$T_{KS}[n] = -\frac{\hbar^2}{2m_e}\sum_i \langle\phi_i|\nabla^2|\phi_i\rangle, \tag{3.8}$$

$$E_H[n] = \frac{e^2}{2} \int \frac{n(\boldsymbol{r})n(\boldsymbol{r'})}{|\boldsymbol{r} - \boldsymbol{r'}|} d^3r d^3r'. \tag{3.9}$$

Now, using the Kohn-Sham formalism, the energy functional of the many-electron interacting system can then be written as

$$E[n] = T_{KS}[n] + E_H[n] + \int V_{ext}(\boldsymbol{r})n(\boldsymbol{r})d^3r + E_{II} + E_{xc}[n], \tag{3.10}$$

where we have introduced the exchange-correlation functional $E_{xc}[n] = F[n] - T_{KS}[n] - E_H[n]$. It is important to note here that we cannot exactly calculate the exchange-correlation E_{xc} as a function of the electron density.

We then apply the variational technique and arrive at the single particle KS equation

$$H_{KS}\phi_i(\boldsymbol{r}) = \left[-\frac{\hbar^2}{2m_e} + V_{ext}(\boldsymbol{r}) + e^2 \int \frac{n(\boldsymbol{r'})}{|\boldsymbol{r} - \boldsymbol{r'}|} d^3r' + \frac{\delta E_{xc}}{\delta n(\boldsymbol{r})} \right] \phi_i(\boldsymbol{r}) = \epsilon_i \phi_i(\boldsymbol{r}). \tag{3.11}$$

Thus, the Kohn-Sham potential $V_{KS} = V_{ext}(\boldsymbol{r}) + V_H(\boldsymbol{r}) + V_{xc}(\boldsymbol{r})$, where

$$V_H(\boldsymbol{r}) = e^2 \int \frac{n(\boldsymbol{r'})}{|\boldsymbol{r} - \boldsymbol{r'}|} d^3r', \tag{3.12}$$

$$V_{xc}(\boldsymbol{r}) = \frac{\delta E_{xc}}{\delta n(\boldsymbol{r})}. \tag{3.13}$$

The single-particle Kohn-Sham equations need to be solved self-consistently. Initially, a starting guess for the charge density is assumed, based on which $V_H(\boldsymbol{r})$, $V_{xc}(\boldsymbol{r})$ and eventually the Hamiltonian are calculated. Solving the Hamiltonian leads to a new charge density; the procedure is then repeated until the self-consistency criterion (usually checking that the total energy is converged) is reached.

Note that the exchange-correlation functional is in principle an exact quantity, including all the many-body effects. However, in practice, some approximation must be made in calculating it, and the most common forms are the LDA and GGA exchange-correlation functionals.

In LDA, an approximation is made that the exchange-correlation energy is approximately equal to that of a homogeneous electron gas which has the same density at that point in space. The GGA makes this approximation better by including the gradient of the electron density in the expression for the exchange-correlation energy of the many-electron system.

In practice, the Kohn-Sham wave functions need to be expanded in terms of some basis sets. One of the common choices is the plane-wave basis set which is suitable for translation-invariant systems.

$$\Psi_{n,\boldsymbol{k}}(r) = \sum_{\boldsymbol{G}} C_{n,\boldsymbol{k}}(\boldsymbol{G}) e^{i(\boldsymbol{k}+\boldsymbol{G})\cdot\boldsymbol{r}}, \tag{3.14}$$

where $n, \boldsymbol{k}$ are as in the Bloch theorem, and the $\boldsymbol{G}$'s are taken from the grid of points in k-space. While the number of $\boldsymbol{G}$ vectors in the reciprocal lattice is infinite, in implementation, a cut-off has to be imposed on the number of plane waves that can be included. Because of this, one has to make sure that the results are converged with respect to the plane waves.

Similarly, the Brillouin zone must be sampled using a finite set of k-points. For self-consistent calculations, the usual choice is a regular grid of points. The number of k-points to include is another choice that needs to be made based on the convergence of the results. In practice, one would run calculations on different sizes of k-grids to test for this; when the total energy difference between the last two calculations is very small (less than some energy threshold value as the grid size is increased), one would declare the calculations converged, and choose the appropriate k-grid. Depending on the spatial symmetries of the system, most DFT packages sample k-points from a smaller part of the Brillouin zone called the "irreducible" part, and this is able to describe the physics across the entire Brillouin zone.

In our calculations, we choose to use an energy cut-off of 450 eV and a k-grid of 11x11x11 k-points based on convergence tests indicating that the total energies are converged to less than 5 meV.

DFT is one of many first-principles techniques available to study condensed matter systems. While there exist exact methods that take into account all the electrons in the system and solve for the energies by exactly diagonalizing the Hamiltonian matrix, in practice, the systems we study often have hundreds of electrons. This means that the Hamiltonian is a considerably large matrix making it harder to diagonalize. This is part of the reason why many implementations of DFT make a pseudopotential approximation, forming a theory for just the valence electrons and assuming that the core electrons participate by creating an effective potential. Though there are codes which have been optimized to diagonalize matrices of large dimensions, making the above assumptions about the valence and core electrons in calculations does not result in a considerable loss of accuracy. The appropriateness of DFT for a given material is of course dependent on the types of interactions present in the system. In our case, using DFT is especially useful as the heterostructures we study consist of materials with almost no many-body interactions, and contain thousands of electrons, making a fully many-body approach inefficient.

The layered structure of the 3D TIs suggests that the van der Waals interactions play a role in the binding between QLs and must thus be included in DFT calculations. There are two main classes of methods.

The first class accounts for the van der Waals interactions by adding a semi-empirical correction to the energy calculated using an exchange correlation functional such as GGA or LDA, and includes the methods DFT+D2 [41], DFT+D3 [42], Tkatchenko-Scheffler [43, 44] (TS), and Tkatchenko-Scheffler with Many-body Dispersion [45, 46] (TS-MBD). The energy correction for DFT+D2 [41] is shown below:

$$E_{disp} = -\frac{1}{2}\sum_{I=1}^{N_{atoms}}\sum_{J=1,J\neq I}^{N_{atoms}}\sum_{\boldsymbol{L}}\frac{C_{6IJ}}{r_{IJ,L}^{6}}f_{d,6}(r_{IJ,L}), \tag{3.15}$$

where N_{atoms} is the number of atoms in the unit cell, $\boldsymbol{L} = (l_1, l_2, l_3)$ are all the unit cell translations, C_{6IJ} are the semi-empirical dispersion coefficients for the atom pair I, J, and $r_{IJ,L}$ is the distance between atom I in unit cell $\boldsymbol{L} = 0$ and atom J in the unit cell L. $f(r_{IJ,L})$ is a damping function that ensures that the contribution from atoms located at distances of the order of bond lengths from each other is negligible. These pairwise energy corrections are calculated up to some cut-off distance beyond which they don't contribute significantly. The DFT+D3 vdW method has a similar form of the energy correction as

DFT+D2, but includes an additional term proportional to r^{-8}. Thus, the semi-empirical methods calculate an energy correction which is added to the total energy calculated using the exchange-correlation functional at the end of each iteration.

The second class of methods uses functionals which contain a nonlocal long-range vdW correlation, where the correlation depends on the electron density and its gradient, and includes, in our analysis, SCAN-rVV10 [47, 48] and Langreth-Lundqvist vdW-DF2 [49]. In these type of methods, the functional itself is modified.

Thus, the first class of methods add a vdW energy correction to the total energy during the optimization, whereas the second class of methods includes the vdW interactions in the exchange-correlation functional.

As mentioned in the previous chapter, it is advantageous to use DFT over analytical methods largely due to the scaling with system size. It is important to keep in mind that the method we choose must not make assumptions about the lattice constants or strain at the interface, since DFT is a ground-state theory and can end up predicting a metastable state which is unphysical. Our goal is to set up a systematic computational framework which makes as few assumptions as possible, with predictive power which can be used to motivate future experiments on TI-based heterostructures. Upon setting up this framework, we may then investigate the properties of TI-based heterostructures, including properties such as the energy dispersion, Dirac velocity and spin structure. A question of practicality often arises in the synthesis of such heterostructures - what types of heterostructures can be grown? In some situations, if the two layers being deposited at the interface are highly polar and repel each other, or suffer from a large strain, the two materials will simply peel apart. One of the first questions is hence to ask if a heterostructure is stable and can be grown. A useful indicator of stability is the surface or interface energy - positive values imply that the sample is stable.

CHAPTER 4.

IMPORTANCE OF VAN DER WAALS INTERACTIONS FOR AB INITIO STUDIES OF TOPOLOGICAL INSULATORS

This section is based on my work that has been published [50]. The electronic band dispersion in the 3D TIs in the direction normal to the layers is comparable to that in the plane, indicating that vdW interactions can be treated as a correction in the ab-initio calculations of the properties of the TIs. An important question is which of the many available forms of the vdW corrections satisfactorily describes both structural and electronic properties at the same time, and we comprehensively address it here within the framework of the density functional theory (DFT)-based ab-initio methods. While vdW interactions in layered TIs have been investigated, a complete picture has not been presented, and we have filled this gap.

Many previous DFT studies of Bi_2X_3 in bulk and at surfaces [51] used experimentally determined lattice constants [52, 53, 54, 55, 56, 57, 58], fixing the volume of the unit cell, and finding the relaxed atomic positions within this cell under the constraint of maintaining the crystal symmetry. The results reproduce salient features of the electronic spectra in bulk and at surfaces, although there is some debate about whether many body corrections are necessary to obtain both the correct magnitude of the gap and its character (direct vs indirect) [59, 60, 56]. In the same spirit, existing studies of interfaces either consider lattice matched cases [61] or make a priori assumptions about structural changes at the boundary, such as fixing the inter-QL distance to its experimental value [62].

The danger inherent to such approaches is that the standard DFT is a ground state theory. Applying it to a fixed set of parameters without allowing their values to attain their ground state values within the same theory may, in general, give the results for, e.g. electronic structure, that are not characteristic of the ground state of the material being studied.

There have been two principal reasons for continuing to make these assumptions. First, while it is known that full geometry relaxation of the bulk (when the unit cell volume is allowed to change) using standard exchange-correlation functionals such as the Local Density Approximation (LDA) or the Generalized Gradient Approximation (GGA) yields lattice parameters significantly different from those determined experimentally, which implies that the strain field is not correctly determined using these methods [37], using the experimental values allowed a quick (and perhaps somewhat fortuitous) access to the qualitative salient features. Second, since the electronic structure of bulk Bi_2X_3 only weakly varies (on the scale of the bandwidth) when vdW and similar corrections to the GGA and LDA are included, and since the existence of the topological Dirac state at the surface is protected by symmetry, there seemed to be little incentive to include them for basic analysis. At interfaces in prototype devices, however, the situation is different: strain leads to surface reconstruction and symmetry breaking, and changes the behavior of the topological states, so we need to be able to optimize the structure and investigate the dispersion and spin properties of the

This chapter was previously published as Karunya Shirali, William A Shelton, and Ilya Vekhter. "Importance of van der Waals interactions for ab initio studies of topological insulators," Journal of Physics: Condensed Matter, **33** 035702 (2021).

topological interface states within the same methodology. This is why we have performed a systematic investigation of the inclusion of vdW corrections in ab initio calculations of Bi_2X_3.

Other studies previously considered vdW interactions in first principles calculations of the bulk [63, 64, 65, 66] and surfaces [66, 67, 68, 69]. One of them [63] did not treat the lattice and electronic structure in the same framework: the authors first performed structural optimization including vdW but omitting the spin-orbit interaction (SOI), well known to be critical for band inversion in topological insulators; they then computed the electronic band structure with SOI (employing GGA), not changing the lattice. Other publications [67, 68, 69, 66] addressed the properties of the surface states considering, as is common in the ab-initio work, periodic structure consisting of a slab of a TI surrounded by vacuum. However, they used slab geometries with small vacuum thickness, and our results below imply that in those cases slabs interacted with each other, suggesting that the results were not applicable to a free surface. Indeed, some of these works obtained lattice constants and electronic dispersion which differ from both experiment and our results presented below, and are not compared to bulk results. The effects of strain on slabs of Bi_2Se_3, Bi_2Te_3, Sb_2Te_3 and Sb_2Se_3 have been investigated, including vdW interactions in the first principles calculations [70]. However, the authors of this investigation [70] only considered the DFT+D2 method, and did not compare with other techniques. The results of a study [65] on a large number of layered materials, which included the TIs that are the focus of our investigation, considered different vdW methods in the bulk, but did not analyze surface properties, and hence did not consider the slab geometry. As a result, the authors could not make a clear connection with surface and topological properties. We are aware of only one previous investigation [71], which considered several different implementations of vdW interactions in density functional theory, compared the outcomes, and argued for the most appropriate method for layered TIs. Our conclusions about the optimal methodology differ from theirs, and we provide a physical picture that supports our findings.

Meta-GGA functionals promise a better description of several classes of materials within the DFT approach, and a recent paper [66] reported the results for SCAN+vdW in comparison with GGA/LDA with and without D3 corrections for the 3D TIs. Their results for SCAN differ from ours, as discussed below: most dramatically, we find that this method yields a metallic ground state for the 3D TIs that we considered.

We have carried out a comprehensive comparison of different implementations of vdW interactions in bulk and surface DFT calculations of Bi_2Se_3 and Bi_2Te_3. We first show that the results of the LDA and GGA calculations are unable to fully describe the physics governing the structural and electronic properties of layered TIs. We then consider two classes of vdW methods. The first class are the semi-empirical energy correction methods, and the second class of methods use functionals which contain a nonlocal long-range vdW correlation.

We do not use here hybrid functionals [54] that take into account a fraction of the exact Hartree-Fock exchange energy, nor do we emply the techniques that compute the electron self-energy with the renormalized Coulomb potential (GW) [53, 59], which aim to improve the accuracy of these approximations. Both the (in principle very precise) GW method and its non-self-consistent counterpart, G_0W_0, are computationally expensive, rendering them impractical for surface and interface calculations [54]. Our goal is to set up a comprehen-

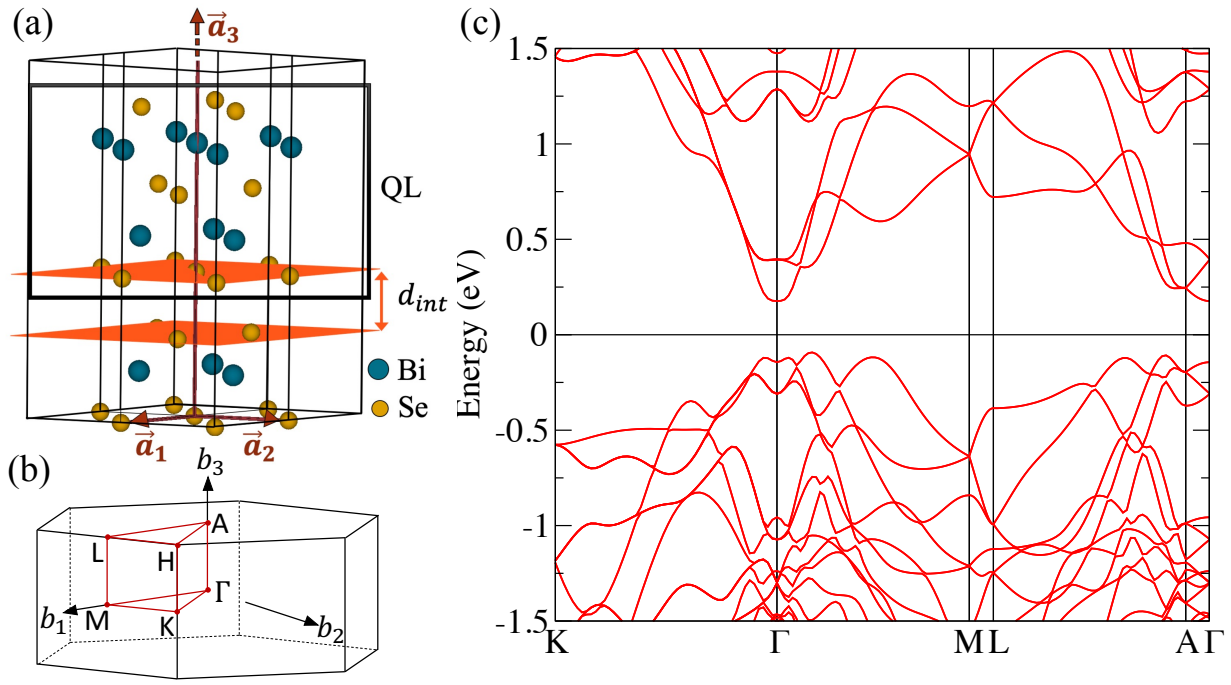

Figure 4.1. Bulk structure and electronic properties of Bi_2Se_3. (a) Crystal structure with hexagonal unit cell, including the inter-QL distance, d_{int}. We show the in-plane lattice vectors $\vec{a}_{1,2}$, but the dashed arrow for lattice vector $\vec{a}_3$ indicates that it extends beyond the range shown, as the unit cell in this representation contains 3 QLs. (b) Hexagonal Brillouin zone. (c) Electronic band structure calculated using GGA with van der Waals interactions (DFT+D2 method).

sive framework which treats structural and electronic properties on equal footing, which is necessary for first principles calculations of interfaces.

To evaluate the accuracy of different methods we compare the values for the bulk parameters, including, in addition to the lattice constants, the inter-QL distance d_{int}, as well as the band gap and the electronic density of states. We also used the value of the Dirac velocity for the surface states as a test of the quality of our approaches for the slab calculations.

We find that the semi-empirical methods are consistently more accurate than the the vdW functionals in yielding the lattice and electronic structures, as well as the correct and stable properties of the surface states for both Bi_2Se_3 and Bi_2Te_3. The unit cell volume and the electronic density of states obtained using vdW-DF2 functional differ significantly both from the experimental values and from the results obtained using semi-empirical methods. The SCAN functional and its variations predict Bi_2X_3 to be a metal.

4.1 Computational Details

We used hexagonal unit cells for Bi_2Se_3 and Bi_2Te_3 (see Figure 4.1(a)) which are convenient for the description of the surface states. All calculations below were carried out using the Vienna Ab initio Simulation Package [72, 73, 74, 75] (VASP), version 5.4.4. Crystal-

lographic information is taken from experimental data [76] retrieved from Crystallography Open Database [77, 78, 79, 80, 81]. In our calculations we use data on the Bi_2Se_3 and Bi_2Te_3 crystal structure of Nakajima [76], rather than earlier data [82, 83], based on a recent analysis [63]. We used Project Augmented Wave (PAW) potentials [84, 85] for Bi ($5d^{10}6s^26p^3$) and Se ($4s^24p^4$), for a total of 48 electrons, and a plane-wave basis. Convergence tests revealed that a Γ-centered k-point grid of 11x11x11 k-points and an energy cut-off of 450 eV for the plane wave basis are sufficient for high accuracy results. We performed fully relativistic calculations which include spin-orbit interaction (SOI). The convergence threshold for energy is taken to be 10^{-5} eV. Band structures are plotted with data processed using vaspkit [86]. We used GGA–PBE [87, 88], LDA [89], LDA+U and GGA+vdW, with full relaxation; for the last category, we compared the results of several methods including van der Waals interactions: DFT–D2 [41], DFT–D3 [42], DFT–TS [43, 44] (Tkatchenko-Scheffler), DFT–TS-MBD [45, 46] (Tkatchenko-Scheffler with Many-Body Dispersion). The vdW functionals studied consisted of the SCAN [47], SCAN–rVV10 [48] and vdW-DF2 [49] methods.

Semi-empirical methods add to the total energy corrections proportional to r_{ij}^{-6} (DFT+D2, DFT+TS) with additional terms varying as r_{ij}^{-8} (DFT+D3) for each pair of atoms i, j which are separated by less than a cutoff distance. To reduce the contribution from pairs of atoms that are bonded covalently, these methods employ a short-distance damping function. The method DFT+TS uses the same energy correction as DFT+D2, modifying the damping function and dispersion coefficients in the energy correction to reflect the local chemical environment around each atom. The method DFT+TS-MBD (MBD@rsSCS) uses a random phase approximation-like expression for the self-consistent screening, treating each atom as a fluctuating dipole, to arrive at the van der Waals energy correction.

The van der Waals functionals considered in this study are the SCAN, SCAN–rVV10, and the vdW-DF2 (Langreth - Lundqvist) functionals. SCAN is a type of semi-local exchange-correlation functional which includes the intermediate-range vdW interactions, while rVV10 is a nonlocal functional which accounts for the long-range vdW interactions by including a long range energy correlation term which depends on the electron density and its gradient. The vdW-DF2 method uses the exchange functional PW86 (which does not incorporate a van der Waals correction), and adds a nonlocal functional which contains the long-range van der Waals correction.

For slab calculations, the surfaces were modelled using slabs of thickness 5-7 QL ($\sim$ 50-70 Å). We find that slabs 5 QL thick are sufficient since the hybridization gap between topological states at different surfaces is small. With vdW interaction included we find that using a vacuum thickness roughly equal to twice that of the slab is sufficient to avoid interaction of the slab with periodic images of itself. Atoms in the outermost QLs of the slab are allowed to relax in all directions without restriction, while atoms in the "bulk" part of the slab are held fixed. Slab calculations were run using the methods DFT+D2, DFT+D3, DFT+TS and DFT+TS-MBD and compared based on features of the surface states such as the Dirac velocity and spin texture. A dipole correction along the z direction was tested and found to not contribute significantly, which is consistent with the picture of closed shell QLs.

Table 4.1. Results for the structural optimization of Bi_2Se_3 without the van der Waals corrections, using GGA and LDA. For each parameter we show the percentage difference relative to the experimental value.

	Expt.	GGA		LDA	
a (Å)	4.143 [76]	4.227	+2.0%	4.086	-1.4%
c (Å)	28.636 [76]	29.218	+2.0%	28.244	-1.4%
d_{int} (Å)	2.579 [76]	2.746	+6.5%	2.378	-7.8%
Gap E_g (eV)	0.3 [10]	0.1567	-48%	0.4594	+53%

Table 4.2. Results for the structural optimization of Bi_2Se_3 without the van der Waals corrections, using LDA+U. For each parameter we show the percentage difference relative to the experimental value.

	Expt.	LDA+U					
		$U = 3$		$U = 5$		$U = 7$	
a (Å)	4.143 [76]	4.115	-0.7%	4.144	+0.024%	4.159	+0.4%
c (Å)	28.636 [76]	28.445	-0.7%	28.646	+0.035%	28.750	+0.4%
d_{int} (Å)	2.579 [76]	2.429	-5.8%	2.475	-4.0%	2.514	-2.5%
Gap E_g (eV)	0.3 [10]	0.2891	-3.6%	0.2326	-22%	0.1143	-62%

Table 4.3. Results for the structural optimization of Bi_2Te_3 without the van der Waals corrections. For each parameter we show the percentage difference relative to the experimental value.

	Expt.	GGA		LDA	
a (Å)	4.386 [76]	4.476	+2.1%	4.339	-1.1%
c (Å)	30.497 [76]	31.124	+2.1%	30.167	-1.1%
d_{int} (Å)	2.613 [76]	2.783	+6.5%	2.484	-4.9%
E_g (eV)	0.165 [12]	0.137	-17%	0.103	-38%

4.2 Bulk properties

4.2.1 LDA and GGA

We start with the results for the most commonly used LDA and GGA-PBE approximations that do not include vdW corrections. Our results for the structural optimization of Bi_2Se_3 (Bi_2Te_3) are shown in Table 4.1 (Table 4.3). As often happens, LDA overbinds the electrons: for Bi_2Se_3, it leads to a contraction of the lattice constants compared to their experimental value. Our result for the volume change of the unit cell is in quantitative agreement with the value of 4% found before [37], albeit the values for the lattice constants differ due to different optimization procedures. In contrast, using GGA overestimates the unit cell volume by about 6% in our calculation vs. a reported value of almost 10% [37]. Another investigation [63] found the cell volume overestimated even more using PBE, but that is mostly due to a significant elongation of the c-axis lattice constant, perhaps related to the effectively two-dimensional k-point mesh (13x13x1) used in that work.

Similarly, for Bi_2Te_3, LDA reduces the unit cell volume by 3% compared to a value of 5% [63]. GGA follows very similar trends to those in Bi_2Se_3. The 6.3% increase in the unit cell volume is greater than a reported value of 4.9% [63]. Another publication [90] used GGA and found the out of plane lattice constant, c, and inter-QL distance, d_{int}, which deviated 4.6% and 18.7% respectively from their experimental values. Our values for the corresponding parameters are smaller, see Table 4.3, possibly due to the different type of pseudopotential they used (fully relativistic norm-conserving).

Notably, using both GGA and LDA we find that the difference between the experimental values and those obtained from first principles is much greater for the distance between adjacent QLs (see Figure 4.1(a)), d_{int} in Table 4.1, than for the lattice constants. This strongly suggests the need for inclusion of the van der Waals interactions between different quintuple layers.

Both GGA and LDA yield sizeable deviations for the bulk energy gaps, as is common for small gap semiconductors with strong spin-orbit coupling [91, 92]. The band gap of 0.137 eV that we find for Bi_2Te_3 using GGA is slightly closer to the experimental value than a gap of 0.12 eV [90]. Our band gap from an LDA calculation for Bi_2Te_3 is very close to the value of 0.106 eV reported for the LDA band gap [57].

For completeness, and to clearly show that local Coulomb interactions are not the origin for the discrepancy, we performed LDA+U calculations on Bi_2Se_3 with the on-site repulsion on Bi orbitals, see Table 4.2. For $U = 5$, the lattice constants a and c are very close to their experimental values, but the inter-QL distance still significantly deviates from that in experiment, and is only improved for $U = 7$, while the lattice constants increase for that value. In contrast, the gap magnitude is closest to experiment for $U = 3$. Therefore no single value of U consistently improves the results. Moreover, increasing values of U tend to collapse the energy gap, in contrast to the physical expectation that Coulomb repulsion localizes corresponding orbitals and pushes bands apart. The situation is even worse for GGA+U as we very quickly reach gap collapse and metallicity. We therefore conclude that the error in the inter-QL distance must be related to the long-range van der Waals part of the interaction.

Table 4.4. Results for the structural optimization of Bi_2Se_3 using different semi-empirical van der Waals corrections. For each parameter we show the percentage difference relative to the experimental value.

	Expt.	DFT+D2	DFT+D3	DFT+TS	DFT+TS-MBD
a (Å)	4.143 [76]	4.141	4.175	4.188	4.176
Devn. a	-	-0.05%	+0.77%	+1.1%	+0.79%
c (Å)	28.636 [76]	28.624	28.858	28.948	28.866
Devn. c	-	-0.04%	+0.77%	+1.1%	+0.80%
d_{int} (Å)	2.579[76]	2.547	2.587	2.623	2.584
Devn. d_{int}	-	-1.2%	+0.31%	+1.7%	0.19%
Gap E_g (eV)	0.3 [10]	0.2638	0.2273	0.2125	0.2337
Devn. E_g	-	-12%	-24%	-29%	-22%

Table 4.5. Results for the structural optimization of Bi_2Se_3 using different van der Waals functionals. For each parameter we show the percentage difference relative to the experimental value.

	Expt.	SCAN	SCAN-rVV10	vdW-DF2
a (Å)	4.143 [76]	4.182	4.177	4.489
Devn. a	-	+0.94%	+0.82%	+8.4%
c (Å)	28.636 [76]	28.907	28.872	31.029
Devn. c	-	+0.94%	+0.82%	+8.4%
d_{int} (Å)	2.579[76]	2.663	2.651	3.349
Devn. d_{int}	-	+3.3%	+2.8%	+30.0%
Gap E_g (eV)	0.3 [10]	Metal	Metal	0.1749
Devn. E_g	-	-	-	-42%

Table 4.6. Results for the structural optimization of Bi_2Te_3 using different forms of van der Waals corrections. For each parameter we show the percentage difference relative to the experimental value.

	Expt.	DFT+D2	DFT+D3	DFT+TS	DFT+TS-MBD	SCAN
a (Å)	4.386 [76]	4.382	4.419	4.422	4.419	4.418
Devn. a	-	-0.09%	+0.75%	+0.82%	+0.75%	+0.73%
c (Å)	30.497 [76]	30.472	30.724	30.747	30.726	30.719
Devn. c	-	-0.08%	+0.74%	+0.82%	+0.75%	+0.73%
d_{int} (Å)	2.613 [76]	2.616	2.636	2.660	2.621	2.678
Devn. d_{int}	-	+0.11%	+0.88%	+1.8%	+0.31%	+2.5%
Gap E_g (eV)	0.165 [12]	0.1608	0.1585	0.1572	0.1557	Metal
Devn. E_g	-	-2.5%	-3.9%	-4.7%	-5.6%	-

4.2.2 Inclusion of van der Waals interactions

Including van der Waals corrections semi-empirically in the structural optimization leads to a dramatic improvement in the agreement with experiment for values of the lattice constants and the inter-QL spacing, see Table 4.4, Table 4.5 and Table 4.6. The lattice constants deviate by less than about a percent from the experimental values, and the inter-QL spacing is also much closer to experiment. DFT+D2 produces particularly good results, where most deviations are below 0.1%, with the only exception being the inter-QL distance in Bi_2Se_3 which gives 1.2% error, greater than the corresponding value of −0.35% found earlier [63]. The unit cell volume we find differs from experiment by −0.14% for Bi_2Se_3 and −0.26% for Bi_2Te_3, compared to the respective reported values of −0.07% and −1.14% [63] and 0.70% and 0.82% [70] (obtained for a different crystal structure [83]). For Bi_2Te_3 a unit cell volume deviation of just −0.07% was found before [64], but the inter-QL distance in that calculation differed from experiment by 9.3%. In a calculation where the unit cell shape and volume were allowed to change [93], the deviation in the unit cell volume was found to be −1.8%. The significant difference with the latter result is likely due to the Monkhorst-Pack k-grid of 8x8x2 and scalar relativistic norm-conserving pseudopotentials they used.

DFT+TS-MBD and DFT+D3 also produce good results for the structural parameters. The lattice constants and unit cell volume (3.3% deviation for Bi_2Se_3 and 2.5% for Bi_2Te_3) that we find using DFT+TS are close to the 2.9% and 3.0% values obtained in another study [71] for the same method.

Our results using vdW functionals are in much poorer agreement with the experimental values. The vdW-DF2 method significantly overestimates cell volume, bond lengths and underestimates the band gap, a behavior also reported for bulk Bi_2Te_3 [64]. That work argued in favor of using optB86b-vdW method, which yields a deviation in unit cell volume of 2.0%, and a deviation in inter-QL distance of 3.5%. Also for Bi_2Te_3, using vdW-DF resulted in a unit cell volume and inter-QL distance deviating 2.6% and 1.5% from experiment respectively [90]. These deviations are an order of magnitude greater than what we find using DFT+D2.

We also carried out a calculation using a meta-GGA SCAN-rVV10 method. However, we found that for both materials it yields a metallic ground state. We checked that the SCAN method on its own also yields a metal as implemented in VASP, and confirmed this result for Bi_2Se_3 by checking that the same result is obtained in an all-electron calculation using Elk [94]. Therefore we conclude that at least the current implementation of the SCAN functional is not suitable for describing layered topological insulators. This is in sharp contrast to a recently published study [66] in which a meta-GGA SCAN-based structural relaxation yields an insulator in that paper. Since that study [66] does not give full details of their calculations, and, for example, does not specify the $\boldsymbol{k}$-point grid for bulk calculations, we cannot make a detailed comparison of the methodologies leading to this discrepancy.

Comparing the electronic band structures obtained by different methods provides a complementary check on their applicability. For Bi_2Se_3, the (indirect) band gap obtained using DFT+D2 is much closer to the experimental value than that obtained using other functionals, see Table 4.4. The band structure shown in Figure 4.1(c) exhibits, albeit not very strongly, a characteristic 'camelback' feature in the valence band at the center of the Brillouin Zone (Γ) due to Spin-Orbit Coupling. This feature is sensitive to the choice of the

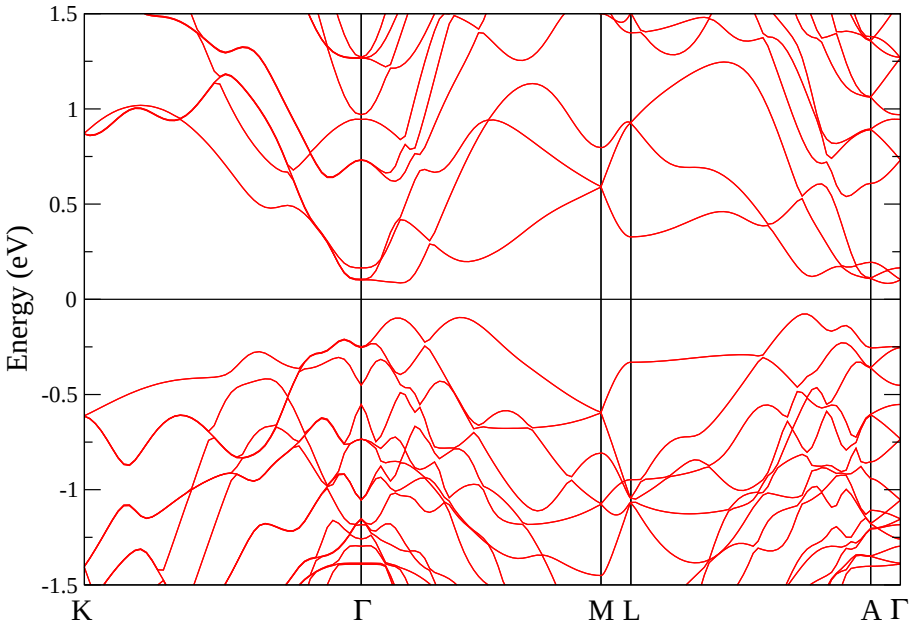

Figure 4.2. Bulk electronic structure of Bi_2Te_3 calculated using GGA with DFT+D2 vdW method, see text for details.

approximation: it nearly vanishes in GGA, and is over-emphasized in LDA to the extent that the conduction band acquires this feature as well. Many body GW corrections removes this feature and produces a direct gap that has been argued to agree with experiment [56]. Resolving this controversy is not the main focus of our work, but we note that the inclusion of a GW correction into LDA that "straightens" the camelback feature also leads to a substantial reduction of the gap magnitude [53, 60, 56], which is overestimated using LDA by over 50%, see Table 4.1). In contrast, the gap we find using DFT+D2 and similar methods is much closer to the experimental value, and therefore we expect that the features of the band structure we find remain robust to further many-body corrections.

For Bi_2Te_3, there exists an analogous 'camelback' feature in the valence band at Γ, and the value of the indirect gap from the DFT+D2 method is close to experiment [12]. We find the Valence Band Maximum to occur along the path $L \to A$ and the Conduction Band Minimum to occur along $A \to \Gamma$, as seen in Figure 4.2. While the indirect gap that we find agrees with optical measurements [95], other studies [64, 57, 96] have found the band gap to not occur along lines in reciprocal space which join high-symmetry points in the Brillouin Zone, whereas still others [53] have found the gap to occur along lines joining high-symmetry points. In the present study, we probed regions of the reciprocal space away from lines joining high-symmetry points, but did not find the band gap to occur close to the points reported in a previous study [64].

Note also that the band structure exhibits substantial energy dispersion along the k_z direction (M-L and A-Γ in Figure 4.1(c) and Figure 4.2). Therefore, in our opinion, k-point mesh with only one point along z used in some previous DFT-vdW calculations [63, 67] is

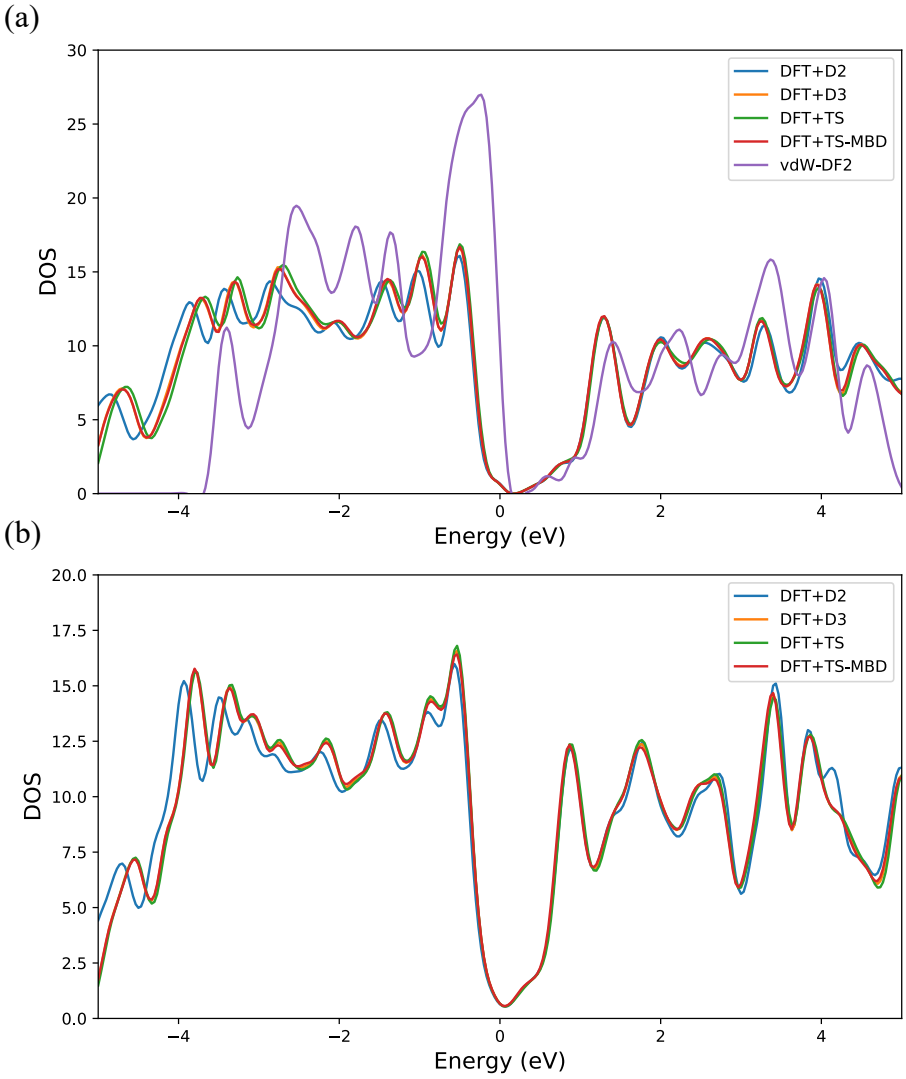

Figure 4.3. Density of states of bulk Bi_2Se_3 and bulk Bi_2Te_3 using different vdW methods. (a) Bi_2Se_3 and (b) Bi_2Te_3.

insufficient for an accurate description of these materials.

Our conclusions about the most appropriate methods are further supported by analyzing the Density of States (DOS), shown in Figure 4.3(a) and Figure 4.3(b) for Bi_2Se_3 and Bi_2Te_3 respectively. The obvious observation is that all semi-empirical methods produce DOS curves which overlap to large accuracy, while the DOS for vdW-DF2 Langreth-Lundqvist method (shown only for Bi_2Se_3) deviates markedly from the rest, with the valence band approaching the chemical potential, which results in a smaller gap value as listed in Table 4.1.

Therefore all the results on the bulk structural and electronic properties show that the semi-empirical methods perform well in reproducing electronic properties of layered topological insulators. In contrast the vdW functionals seem to yield a poor agreement with experiment. Recalling that the quintuple layers effectively act as closed shell units, we suggest that the empirical corrections capture the main physics of the vdW interaction between

different quintuple layers in Bi_2Se_3 and Bi_2Te_3. While all four methods DFT+D2, DFT+D3, DFT+TS and DFT+TS-MBD yield results close to the experiment, we found that DFT+D2 is the most accurate, followed closely by DFT-TS-MBD. The important feature of both methods is that they account only for the long-distance r^{-6} tail of the vdW interactions. This suggests that the vdW correction is indeed due to well-separated charge distributions in different quintuple layers. We choose DFT+D2 for further analysis of the topological surface states.

4.3 Slab calculations and the surface states

We mostly show below the results for the topological surface states obtained using DFT+D2. At first sight, the results are very close to those obtained using DFT+D3, DFT+TS and DFT+TS-MBD. The reason for the closeness, despite DFT+D2 being superior in determination of the structural properties, is that, as discussed below, relaxing the structure of the QLs closest to the surface does not yield appreciable atomic displacement. We expect this to be different for interface calculations. At the same time, we show that, on closer inspection, once again, the DFT+D2 method performs better than its counterparts.

To determine the structure of the surface states we ran calculations for 5-7 QL thick ($\sim$ 50-70 Å) slabs of Bi_2Se_3 and Bi_2Te_3, with a vacuum buffer of 100 Å. We found that 5 QL was the minimal slab thickness for which the surface states at opposite surfaces do not hybridize appreciably, so that the Dirac spectrum was not gapped at our energy resolution.

Irrespective of the number of QLs in the slab we consistently found that we needed to include an amount of vacuum that is approximately equal to twice the slab thickness in order to avoid electrostatic interaction of the slab with its own periodic images. Such an interaction generates a gap in the spectrum of the topological surface states, and yield a weak splitting of the top and bottom surface states. While we find that it is possible to fine tune a small vacuum thickness to minimize hybridization of the topological states at the slab interfaces across the vacuum, consistent results are obtained for the vacuum buffer of order twice the slab width. This is in contrast with other work that used $\sim$10$-$20 Å to obtain the surface state dispersion [66, 97, 98, 68]. We believe this hybridization across vacuum is enhanced by the long tails of the vdW interaction between closed shell QL layers, and checked that the gap at the Dirac point and the splitting of the bands is not affected by the inclusion of dipole corrections at surfaces.

In all our calculations the outermost QLs of the slab (five atomic layers closest to each surface) are allowed to relax, while the atoms in the remaining internal layers ("bulk") are kept fixed at the optimized bulk structure. We find that the atomic displacements in the outer layers are of order mÅ, not causing appreciable reconstruction, and having negligible effects on the electronic structure. This is consistent with a picture where each QL acts as a closed shell, so that the surface termination does not change bond lengths.

The slab band structures for Bi_2Se_3 (Bi_2Te_3) are shown in Figure 4.4(a) (Figure 4.5(a)). They show quasi-linearly dispersing Dirac-like states in the bulk gap arising from the surface states. For Bi_2Se_3, the Dirac point lies 0.21 eV below the conduction band minimum, in agreement with experiments [10, 99, 13, 100], and 0.06 eV above the valence band maximum. This is in qualitative agreement with experiment [8], although self-doping effects likely affect the location of the Dirac point. For Bi_2Te_3, the surface band rises above the Dirac point

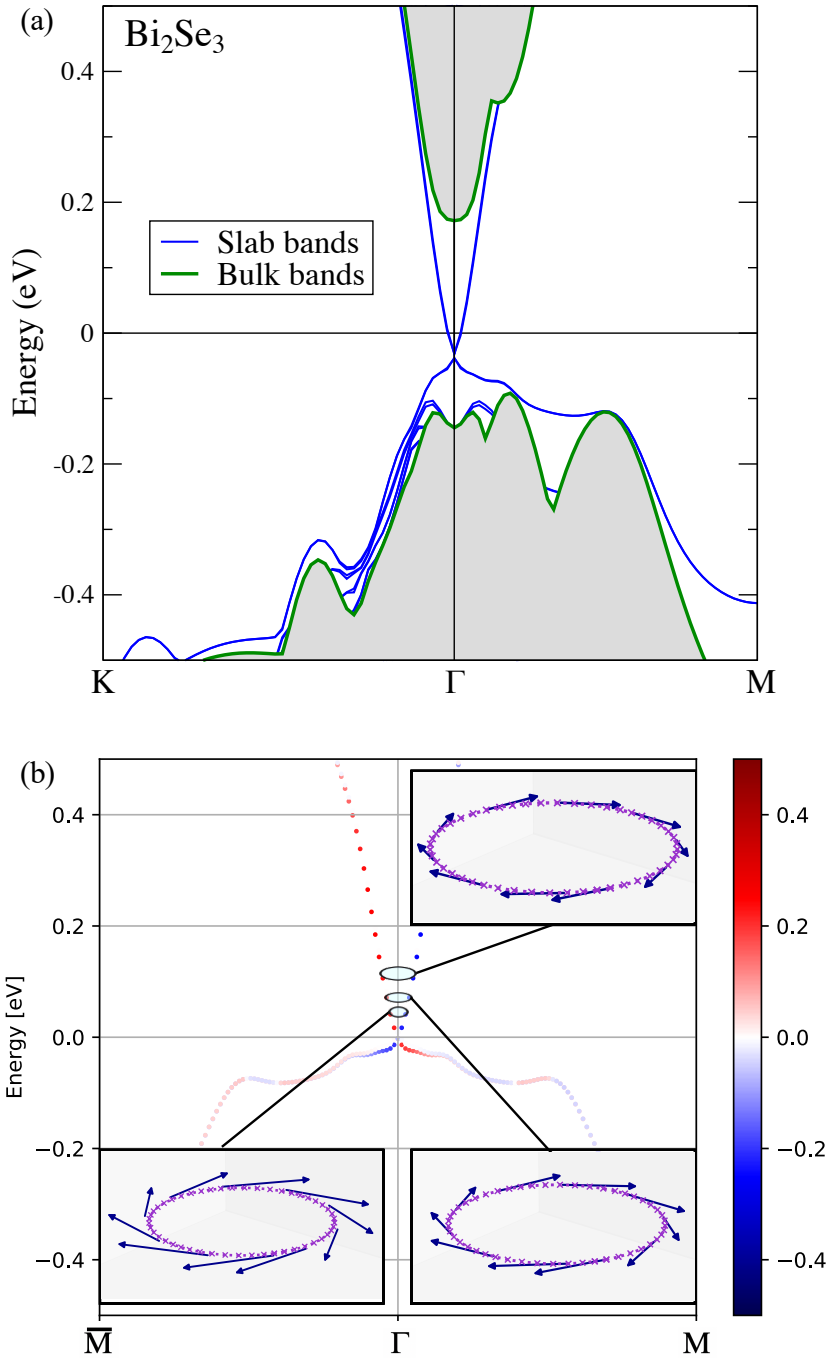

Figure 4.4. Topological surface states in 5QL thick Bi_2Se_3 slab with 100 Å vacuum using DFT+D2 van der Waals corrections. (a) Electronic band structure with bulk bands shaded. (b) y component of the spin for the state at the upper surface of the slab along $\bar{M} - \Gamma - M$. Inset: constant energy contours along with the spin textures at those energies, at the upper surface of the slab, for $E = 0.05$ eV, $E = 0.08$ eV, and $E = 0.125$ eV.

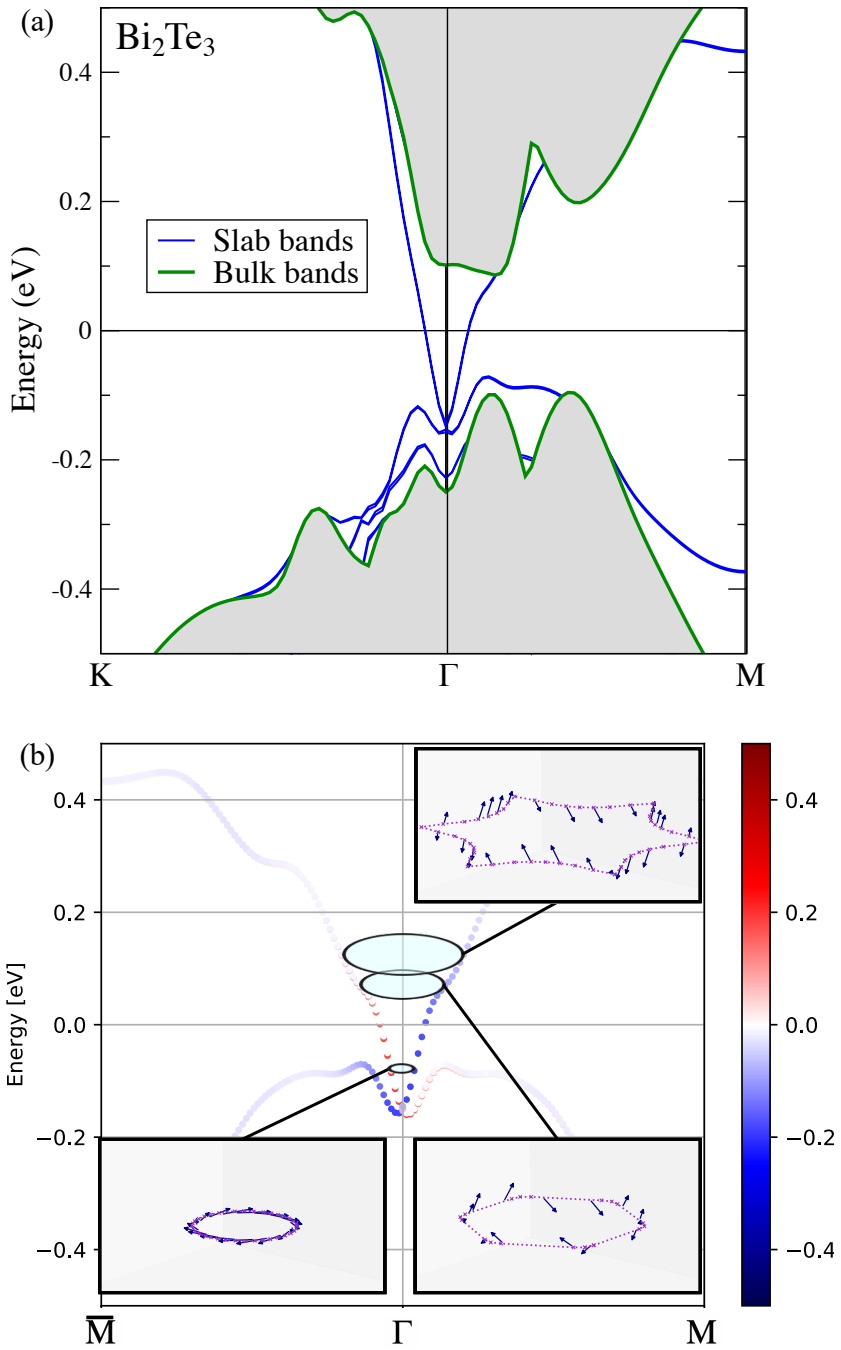

Figure 4.5. Topological surface states in 5QL thick Bi_2Te_3 slab with 100 Å vacuum using DFT+D2 van der Waals corrections. (a) Electronic band structure with bulk bands shaded. (b) y component of the spin for the state at the upper surface of the slab along $\bar{M} - \Gamma - M$. Inset: constant energy contours along with the spin textures at those energies, at the upper surface of the slab, for $E = -0.12$ eV, $E = 0.03$ eV and $E = 0.07$ eV. The hexagonal warping increases with increasing energy.

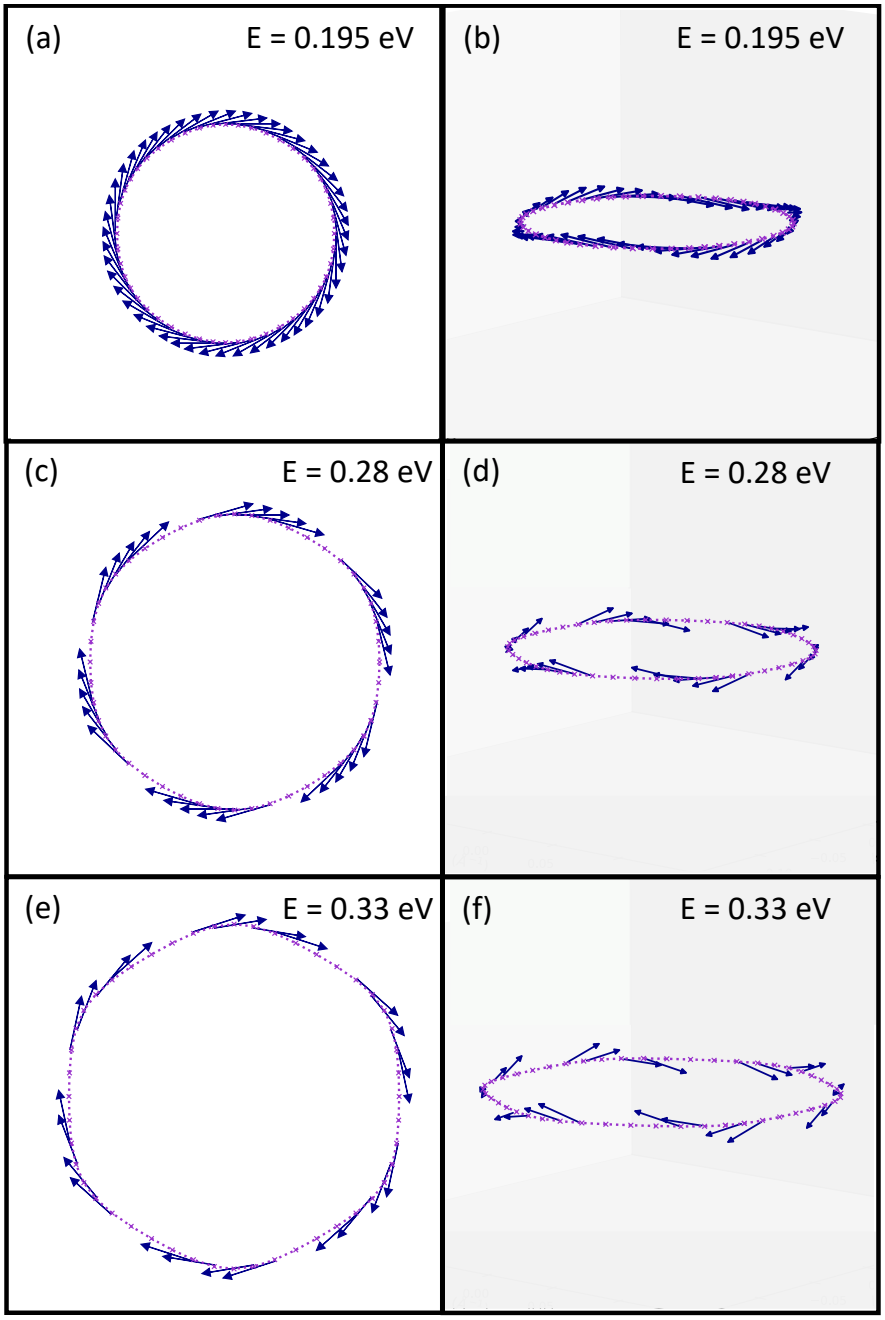

Figure 4.6. Spin textures and constant energy contours of the topological surface states at energies near and above the conduction band minimum, at the upper surface for a 5 QL thick slab of Bi_2Se_3 with 100 Å vacuum, calculated using DFT+D2 van der Waals corrections. Spin textures in the k_x-k_y plane are shown at energies (a) $E = 0.195$ eV, (c) $E = 0.28$ eV, and (e) $E = 0.33$ eV. Out-of-plane components of the spin textures are shown at energies (b) $E = 0.195$ eV, (d) $E = 0.28$ eV, and (f) $E = 0.33$ eV. The constant energy contours begin to display hexagonal warping at energies of around 0.28 eV and above.

Table 4.7. Calculated Dirac velocities of the surface states in slab calculations of Bi_2Se_3 and Bi_2Te_3 using different forms of van der Waals corrections.

	Bi_2Se_3	Bi_2Te_3
	v (m/s)	v (m/s)
Expt.	5.0×10^5 [10]	4.0×10^5 [106]
GGA	4.80×10^5	3.83×10^5
DFT+D2	5.10×10^5	4.04×10^5
DFT+D3	4.07×10^5	3.96×10^5
DFT+TS	4.00×10^5	4.19×10^5
DFT+TS-MBD	3.77×10^5	4.42×10^5

energy as we move along the path $\Gamma \to M$, a feature not seen in Bi_2Se_3. The Dirac point lies 0.05 eV below the valence band maximum (VBM), and 0.23 eV below the conduction band minimum. The latter value is lower than 0.26 eV obtained in an LDA calculation, and closer to the GW value of ~ 0.22 eV [101]. All these values are less than 0.29 eV obtained from optical measurements [12]. The energy difference between the Dirac point and VBM was theoretically found to be 0.10 eV in a previous study [53] and experimentally determined to be 0.13 eV [12].

To compare different semi-empirical vdW methods we evaluate the velocities of the surface Dirac quasiparticles, v. Since the dispersion is quasi-linear, we choose to compute it along the path $\Gamma - M$ close to the k-point $\vec{k} = 0.015\vec{b}_1$, and show the computed and experimental values in Table 4.7. For Bi_2Se_3, the value $v = 5.1 \times 10^5$ m/s obtained using the DFT+D2 method, is much closer to the experimental range of $5.0 - 5.5 \times 10^5$ m/s [102, 103, 104, 51, 105] than the values obtained using other methods (DFT+D3, DFT+TS, DFT+TS-MBD). Our value is also much closer to experiment than those reported in previous ab initio calculations [52, 54]. For Bi_2Te_3, the velocities calculated using different vdW implementations are nearly identical, and the velocity obtained using the DFT+D2 method is close to the values of 3.87×10^5 m/s and 4.0×10^5 m/s reported in experiment [12, 106].

Analyzing the spin structure of the topological states, we find, as expected, that the surface states are nearly perfectly helical close to the Γ point, as shown in Figure 4.4(b) (Figure 4.5(b)) for Bi_2Se_3 (Bi_2Te_3). The spins are normal to the direction of the momenta, and wind around the Dirac point. At higher energies, however, the difference between the two materials becomes evident. The insets in Figure 4.4(b) and Figure 4.5(b) show the *computed* spin orientations along different constant energy surfaces. For Bi_2Se_3, we find that at energies close to the Dirac point, the spins are helical, and there is no discernible evidence of hexagonal warping of the constant energy contours (for example, at $E = 0.125$ eV), in agreement with experiments [107, 104]. Only at energies close to 0.3 eV (where the Fermi level often lies in real Bi_2Se_3 films [108, 109, 99, 13]) and higher, when the energy is in the conduction band, the constant energy contour begins to take on a hexagonal shape, and the spins begin to develop out-of-plane components, as shown in Figure 4.6. In contrast, for Bi_2Te_3, the constant energy contour changes shape with increasing energy at much lower energies, changing from a circle ($E = -0.12$ eV), to a hexagon ($E = 0.03$ eV), to a star ($E = 0.07$ eV). At the same time the spins acquire a substantial out-of-plane component.

It is clear therefore that the hexagonal warping and non-helical behavior of the topological surface states appear together, but that happens at different energies in the two materials.

Figure 4.7 shows the spatial profiles of the probability amplitude for the surface states in comparison with the band states. While all states oscillate on atomic scale, the surface states are localized within approximately a single QL near the interfaces, while the amplitude of the band states is peaked in the central, bulk-like, QLs.

4.4 Slab calculation details

We analyzed the surface states by considering a symmetric slab of the topological insulator with a vacuum layer. Since we are interested in the properties of the linearly dispersing topological surface states, it is crucial to select the parameters so that the states at the opposite surfaces do not hybridize and do not open the gap.

This hybridization can occur via one of two pathways: across the slab or across the vacuum layer. In agreement with previous work [68, 52], we find that 5 QL thick slab of Bi_2X_3 (X = Se,Te) (approximately 48 Å), is sufficient to ensure negligible hybridization of the topological surface states across the slab. Thicker slabs do not substantially change the observed behavior.

Self-interaction across a vacuum buffer is of particular concern when including the van der Waals corrections to the energy since the long power-law tails of this interaction extend over substantial distances in the vacuum. Therefore, it is desirable in principle to increase the vacuum thickness. However, as this results in the increase of the effective unit cell size, at large vacuum thicknesses we may possibly see the effect of the finite FFT grid changes when the vacuum thickness varies.

While we found that we can selectively choose a small vacuum thickness (similar to that often used [68, 63, 67, 20]) where the hybridization across vacuum appears to vanish, see Figure 4.8a, small changes in the size of the vacuum buffer result in the opening of the hybridization gap, and in splitting of the bands, see Figure 4.8b.

In contrast, once we reach the vacuum thickness of about twice that of the slab, the hybridization is generally small, see Figure 4.8c. We still find some select vacuum thicknesses for which we observe gap opening and band splitting, but, in our observation, the results are generally more robust against small changes in the buffer size compared to small vacuum thicknesses.

4.5 Summary of results

We have performed a comprehensive high precision ab-initio analysis of the prototypical topological insulators Bi_2Se_3 and Bi_2Te_3, aiming to treat structural and electronic properties on equal footing. We used different methods of accounting for the van der Waals interactions within the framework of the density functional theory. In agreement with the expectation that vdW interactions play an important role in binding closed shell quintuple layers in layered topological insulators, we found that, in general, their inclusion strongly influences the structural properties, if the structure is allowed to relax and not fixed to the experimental values. Lattice constants, unit cell volume, and the distance between nearest quintuple layers are all sensitive to the inclusion and choice of the vdW interaction.

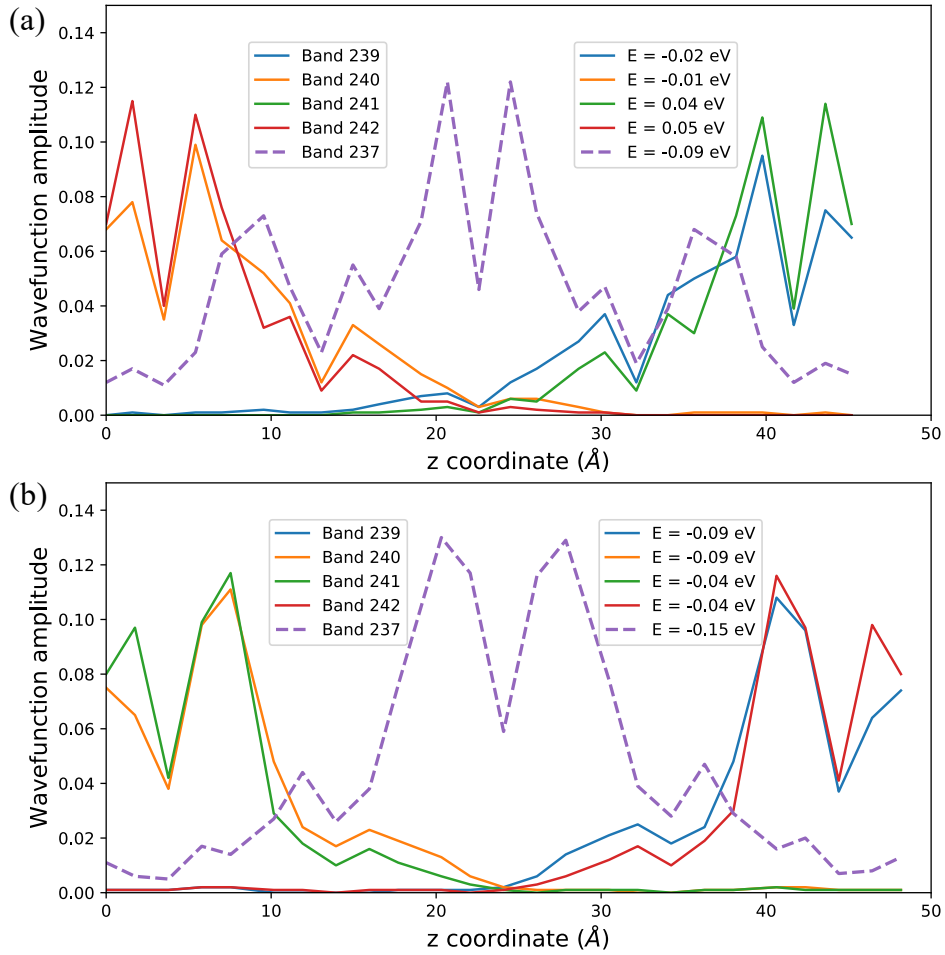

Figure 4.7. Spatial profile of surface (solid lines) and bulk (dashed lines) states (smooth lines) and a state in the bulk bands (dashed lines) at $\boldsymbol{k} = 0.0127\ \boldsymbol{b}_1$, for 5QL thick slabs with 100 Å vacuum. $\boldsymbol{b}_1$ is the in-plane reciprocal lattice vector for the hexagonal unit cell choice. Band 239/240 (241/242) belong to the upper (lower) half of the Dirac cone, while band 237 is near the top of the valence band. (a) Bi_2Se_3; (b) Bi_2Te_3.

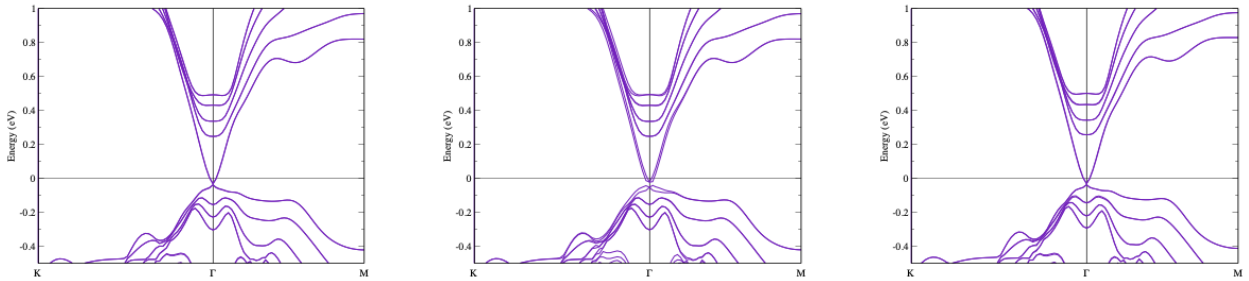

(a) 15 Å vacuum. (b) 33 Å vacuum. (c) 100 Å vacuum.

Figure 4.8. Band structure of a 5 QL thick slab of Bi_2Se_3 with different vacuum thicknesses.

Standard exchange-correlation functionals such as LDA and GGA, are inadequate for structural relaxations, leading to structural and electronic properties which deviate significantly from the experimental values.

We compared two different classes of methods that include vdW interactions in first principles calculations: those which include semi-empirical corrections to the total energy and forces, and those which modify the exchange-correlation functionals to include a vdW term. Our results strongly indicate superiority of the semi-empirical methods, which yield lattice parameters, energy gap, bulk density of states, and the Dirac velocity of the topological surface states in much better agreement with the experimental values. By comparing the errors in the lattice constants vs the inter-QL spacing, we conclude that the long-range energy correction due to interaction between QLs, is the dominant effect of van der Waals forces in layered TIs. Of the semi-empirical methods, the two which account solely for the long-range tail r^{-6} of the vdW interaction (DFT+D2, and DFT+TS-MBD) give much better structural parameters than the methods that attempt to augment it further by including also a shorter range r^{-8} correction (DFT+D3). To us this indicates that the dominant vdW interaction is between the quintuple layers, which act as closed shells.

Extending the comparison to include the electronic properties, we found that the DFT+D2 method in particular gives both very accurate electronic parameters, and yields dispersion and spin structure of the topological surface state that closely match experimental results. Overall, we observe an order of magnitude improvement in the lattice parameters in comparison to when van der Waals corrections are not included; we also obtain accurate values of the Dirac velocities, which indirectly implies that the DFT+D2 method is able to reproduce fine aspects of the electronic structure on scales smaller than the band gap. Therefore our result identifies the leading correction to the commonly used DFT functionals for ab initio calculations of surfaces and interfaces involving topological insulators of the Bi_2X_3 family.

We found that the vdW-DF2 functional yields structural and electronic parameters (cell volume and density of states) for the bulk which deviate significantly from experiments. Our interpretation of this result is that in this class of systems, modification of the exchange-correlation functional is not needed and only the vdW tails are important. The SCAN functional predicted the bulk 3D TIs to be metals.

We believe that the semi-empirical methods, such as DFT+D2 and TS succeed because the materials we study have two characteristic qualities: closed shell QLs, where all bonds are saturated within the QL, and the long-range r^{-6} correction is the most important, and the 3D band structure, where the vdW forces are a correction but not the principal source of the dispersion normal to the layers. The former is backed up by our observation that DFT+D3, which includes an r^{-8} correction in addition to the r^{-6} correction, does not perform as well as DFT+D2. Thus, for materials which possess both the attributes of closed shell layers and 3D interlayer dispersions, we expect such methods to yield accurate results. They are unlikely to perform as well in layered materials which do not possess both of these features, such as the transition metal dichalcogenides.

Methodologically, we found that inclusion of the long range van der Waals interactions requires a vacuum buffer of roughly twice the slab thickness in the system to accurately describe surface states. This suggests that in the calculations of interfaces and heterostructures one needs to pay special attention to the decay range of the interactions with the material thickness. Thus, for calculations involving surfaces, an appropriate amount of vacuum must

be included in the setup so as to not obtain erroneous results due to electrostatic interaction of the surfaces across the vacuum. We have also demonstrated here that the interlayer distance is tied to the strength of the vdW interactions in the system. Thus, obtaining inaccurate interlayer distances in a calculation is a possible indication that crucial vdW corrections are missing; if a heterostructure is constructed with those structural parameters, the values of stress and strain obtained at the interface are likely to be inaccurate.

While previous studies have included select vdW interactions in first principles calculations of specific aspects of the properties of topological insulators, there have not been many systematic investigations of the different ways of accounting for the van der Waals corrections. Determining the optimal vdW method is necessary for any calculation of TIs where the stress and strain fields must be calculated self-consistently. This would be especially important for ab-initio calculations of heterostructures based on topological insulators, where accounting for the stress and strain fields at the interface is crucial for predicting and analyzing possible surface reconstruction and concomitant changes in both dispersion and the spin-momentum locking properties of the topological states. Thus, the simultaneous optimization of the structural and electronic properties is essential for determining the properties of topological insulators. We also established a way to reliably run and analyze slab calculations better than existing works, as we found ways to minimize some possible computational errors that arise in such setups.

To reiterate, when performing calculations on proposed but not yet synthesized or not well characterized interfaces, a systematic approach that avoids assumptions about structural or electronic parameters is necessary. Making such assumptions is an approach that works a posteriori for the surface, but one that we explicitly deemed unsuitable for interface calculations, because of the loss of predictive power for systems where we do not have a priori knowledge of the lattice parameters. Such assumptions about structural or electronic parameters might result in obtaining a solution which is not the ground state. Thus, including the DFT+D2 vdW correction would be appropriate and important when investigating heterostructures of the 3D TIs studied here with other materials. If including DFT+D2 corrections in the other material leads to correctly reproduced bulk structural and electronic properties, it is straightforward to include this correction for the entire system. On the other hand, for systems involving interfaces between 3D TIs and materials in which vdW corrections are not needed, a suitable transition region could be constructed at the interface, over which the strength of the vdW correction goes to zero. When studying the topological interface states in such heterostructures, properties such as the Dirac velocity and the spin structure of surface states will be affected by the inclusion and type of the vdW corrections used, as we have shown here for surfaces.

CHAPTER 5.

INTER-QUINTUPLE LAYER COUPLING AND TOPOLOGICAL PHASE TRANSITIONS IN THE CHALCOGENIDE TOPOLOGICAL INSULATORS

This section is based on my work that has been submitted to a journal [110]. As we have seen in the previous chapter, the properties of the topological states such as the Dirac velocity and the spin-momentum locking depend on the structural lattice constants. In the simplest cases the two atomic-derived energy levels closest to the chemical potential (after accounting for the crystal-field splitting and hybridization) have opposite parity, and are sufficiently close in energy so that Spin-Orbit Coupling (SOC) can flip the energies of those localized levels, and induce inversion between the valence and conduction bands derived from these states in the Brillouin Zone (often close to the Γ-point) [4, 8, 38]. The SOC thus competes with the initial level splitting: if its magnitude is sufficient to generate an inverted band structure, there exists a non-zero bulk topological invariant that guarantees the existence of protected surface states. These states survive as long as the band gap persists, and a transition to a topologically trivial state requires closing of the energy gap.

Pressure and strain have emerged as promising avenues towards controlling topological properties [17, 18, 19, 20]. These may result from alloying or doping by elements of different atomic size that gives rise to chemical pressure[21, 22, 23, 24, 25, 26]. They also appear in heterostructures due to lattice mismatch. Both strain and pressure leave the (atomic) SOC strength mostly unchanged, but modify the hybridization of atomic levels and crystal-field strength. As a result, they may induce a transition between a topological and a trivial state. The physics of this transition is the focus of our work.

We use the ratio of the out-of-plane to in-plane lattice constants in layered compounds, c/a, as a tuning parameter that drives the topological transition, and study it using ab initio Density Functional Theory calculations. The advantage of such an approach is that the system is under no net hydrostatic pressure, albeit simultaneously experiences uni- or bi-axial pressure and strain. This allows us to focus on the physics driving the transition.

We apply this methodology to the family of layered tetradymite materials X_2Y_3 (X=Bi/Sb, Y=Se/Te). Among those, Bi_2Se_3, Sb_2Te_3, and Bi_2Te_3 have been confirmed via experiment [10, 111, 12, 13, 14, 8] to be topological insulators. The fourth member of this family, Sb_2Se_3, has not been grown in the same rhombohedral crystal structure, but was initially predicted to be a trivial insulator [8, 112, 113, 114]. More recent theoretical studies [70, 71] predicted the ground-state of rhombohedral Sb_2Se_3 to be topological. Our results confirm this, and we therefore focus on the common features of the topological transitions in all four members of the family.

The application of pressure was predicted to induce topological phase transitions in the 3D TIs in a number of first-principles [112, 115, 116, 113, 70, 117, 118] and analytical [119, 120] studies. However, a systematic physical picture has not emerged, in part because of strongly anisotropic and implementation-dependent [121], response of the structural parameters to the pressure and strain. This motivated our choice of the c/a ratio as the tuning parameter that eliminates the hydrostatic pressure effects.

For each of the Bi/Sb Te/Se compounds we find a critical value of c/a where the band

gap closes, and beyond that value the band inversion disappears so that the material becomes topologically trivial. In the vicinity of the transition all four materials exhibit similar behavior. In particular, the phase transition is due to the increased level splitting which prevents SOC from inducing the band inversion, and we find that the underlying physics is dictated by the Coulomb and van der Waals interactions between the quintuple layers, which are the basic structural building blocks of these materials. The quintuple layers themselves remain essentially unchanged across the transition, with minimal variation in the overall thickness and bond lengths. Consequently, the hybridization does not vary significantly, in contrast to the often used simplified picture. Instead, it is the inter-quintuple layer interaction that changes the energies of the outer (Se/Te -derived) states compared to their inner (Bi/Sb-derived) counterparts. We discuss the universal features of this inter-quintuple layer interaction and their implication for transitions in other stoichiometric and alloyed topological insulators.

5.1 Technical and Computational Details

Bi_2Se_3, Sb_2Se_3, Bi_2Te_3 and Sb_2Te_3 are rhombohedral compounds, crystallographic group $R\overline{3}m$ (166), point group D_{3d}. As shown in Fig. 4.1, they consist of stacked structural units of five atomic layers $Y1 - X - Y2 - X - Y1$ (X = Bi/Sb, $Y_{1,2}$ = Te/Se) called quintuple layers (QLs). The atomic layers follow an $...ABCABC...$ stacking in the c-axis direction. The pairs of atoms $Y1$ are related to each other through inversion symmetry, as are the X atoms. Each QL has a 'closed-shell' nature, leading to stronger bonding within QLs that is believed to be mainly covalent, and a weaker bonding between QLs. While van der Waals interactions contribute significantly to the inter-QL coupling, the electronic bandwidths in-plane and in the direction normal to the layers are comparable, so that these are structurally and electronically three-dimensional materials, in contrast to, for example, transition metal dichalcogenides.

Calculations were carried out using the Vienna Ab initio Simulation Package [72, 73, 74, 75] (VASP), version 5.4.4, and QUANTUM ESPRESSO v.6.7 [122, 123, 124].

Crystallographic information for Bi_2Se_3 [76] and Bi_2Te_3 [76], as well as for Sb_2Te_3 [125] is taken from experimental data retrieved from Crystallography Open Database [77, 78, 79, 80, 81]. In our calculations we use the Bi_2Se_3 crystal structure of Nakajima [76], rather than the earlier data of Refs. [82, 83]. A comparison of the two can be found in Ref. [63]. For Sb_2Se_3, we use a starting guess for the lattice parameters based on the values reported in Ref. [113].

For VASP calculations we used Projector Augmented Wave (PAW) potentials [84, 85] for Bi ($6s^26p^3$), Sb ($5s^25p^3$), Se ($4s^24p^4$) and Te ($5s^25p^4$), and a plane-wave basis. We also used PBE-GGA [87, 88] for the exchange-correlation functional, and van der Waals interactions were included using the DFT–D2 [41] method, following the framework in Ref. [50]. We confirmed that inclusion of Bi d electrons does not change our results for Bi_2Se_3. We used a Γ-centered k-point grid of 11x11x11 k-points and an energy cut-off of 450 eV for the plane wave basis.

We performed relativistic calculations which include spin-orbit coupling (SOC), with the convergence threshold for energy of 10^{-5} eV. In our calculations we used 15 atom hexagonal unit cells for Bi_2Se_3, Sb_2Se_3, Bi_2Te_3 and Sb_2Te_3.

To confirm the validity of our results we also ran a calculation using QUANTUM ESPRESSO, using the pseudopotentials Bi.rel-pbe-dn-kjpaw_psl.1.0.0.UPF and Se.rel-pbe-n-kjpaw_psl.1.0.0.UPF from `https://www.quantum-espresso.org`, k-grid of 15x15x15 k-points, and energy cut-offs of 653 eV and 6530 eV for the wave-functions and charge densities respectively. We found no substantial differences with the results obtained in VASP.

To calculate the ground-state lattice parameters of each material, we run full structural optimization in which the cell shape, volume, and atomic coordinates are allowed to relax. To investigate the dependence of the structural and electronic properties on c/a, we fix this ratio and carry out structural optimization by running alternate atom and volume relaxations (ISIF=2,7), while not allowing the cell shape to change.

Band structures are plotted with data processed using vaspkit [126], while the band structure projections are plotted using PyProcar [127]. Since we plot the electron bands along a chosen path in the Brillouin Zone, band gaps were also estimated from the density of states.

For Sb_2Se_3 slab calculations, the surfaces are modelled using a 12 QL-thick ($\sim$ 120 Å) slab. With vdW interaction included we find that using a vacuum thickness of $\sim$ 100 Å is sufficient to avoid interaction of the slab with periodic images of itself. Atoms in the three outermost QLs of the slab are allowed to relax in all directions without restriction, while atoms in the "bulk" part of the slab are held fixed.

5.2 Topological phase transition in Bi_2Se_3

In the absence of external strain, Bi_2Se_3 is a topological insulator. Minimization of the energy gives the ground-state at $c/a = 6.91$. In the ground-state, the system is topological, and its bands are inverted: the valence (conduction) band is dominated by the Bi $6p_z$ (Se $4p_z$) orbitals at Γ, but the orbital contribution to the bands switches away from the center of the Brillouin Zone. This inversion persists as we increase the c/a ratio. Figure 5.1(a), (b) shows the bulk bands projected onto the Bi p and Se p orbitals for $c/a = 7.0$, with the weights depicted according to the color scale on the right, and demonstrates this inversion. As expected on general grounds, the band inversion is always accompanied by the emergence of linearly dispersing surface states, see Ref. [50] and Sec. 5.3.1, and therefore we use it as a test for the topological electronic structure.

We confirmed that if we do not include relativistic SOC in our first-principles calculations, the bands are not inverted, and that the conduction band is composed of Bi p_z orbitals, whereas the valence band is composed of Se p_z orbitals.

When the c/a ratio is increased, upon relaxing the unit cell, the in-plane lattice constant a decreases whereas the lattice constant c increases. The detailed results are given in the later part of this chapter. Between $c/a = 7.0$ and $c/a = 7.5$ the value of a (c) decreases (increases) by 2% (6%). Within the QL, the Bi-Se1/Bi-Se2 bond lengths change by less than 0.4% over the same range of c/a values. As the out-of-plane lattice constant c increases, the most significant change happens in the inter-QL distance d_{QL} which grows by 13%, whereas the QL-thickness h_{QL} only increases by 3% between the same c/a values. Thus, the change in the inter-QL distance is about two orders of magnitude larger than the magnitude of changes within the QL.

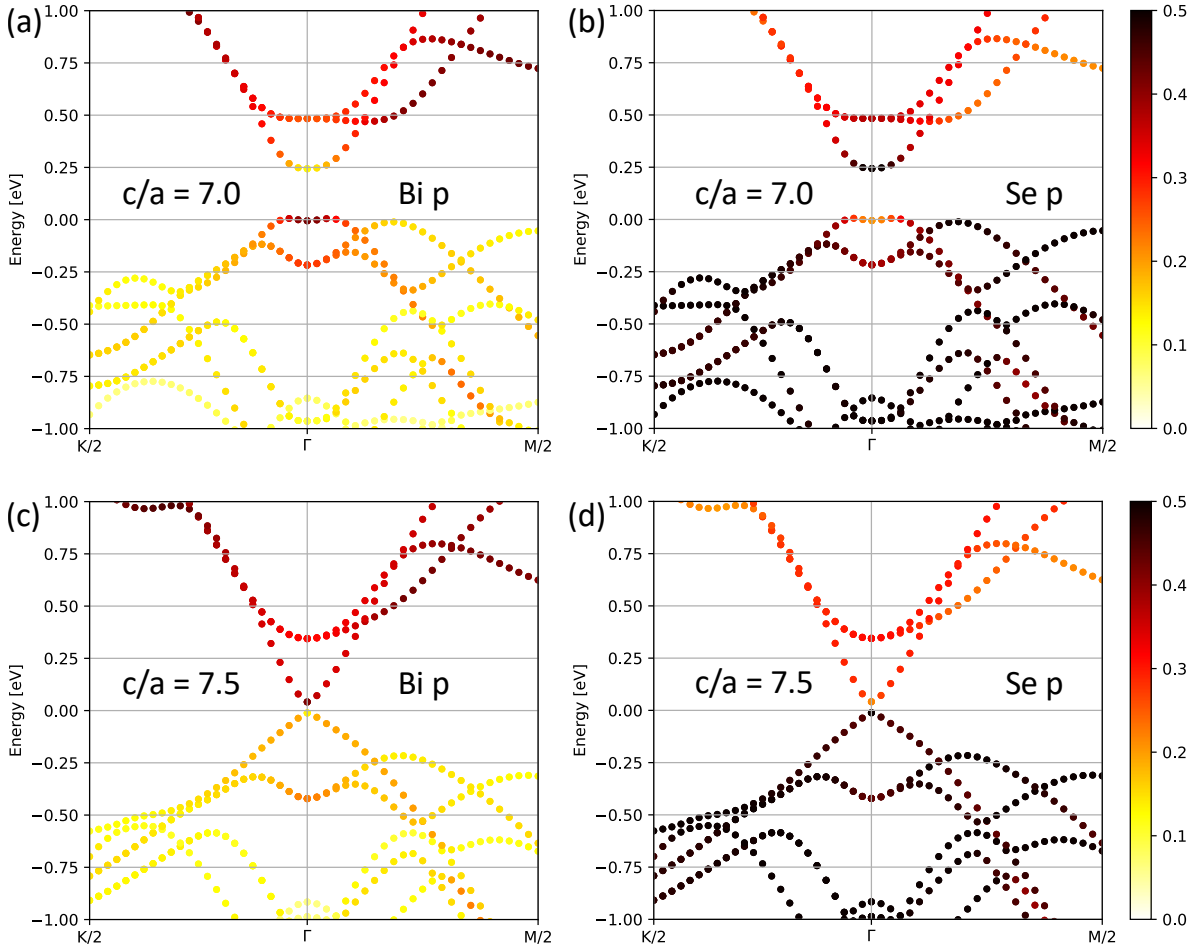

Figure 5.1. Bulk band structure of Bi_2Se_3 projected onto Bi p and Se p for different c/a values. (a), (b) Band structure projections onto Bi $6p$ and Se $4p$ for $c/a = 7.0$ (topological insulating state). (c), (d) Corresponding projections for $c/a = 7.5$ (trivial insulating state). The bands below the chemical potential in (a), (c) have very small weights of Bi p away from Γ, and hence have a very light shade.

As the c/a ratio is increased, the band gap at the Γ point, E_g, decreases, and closes at a critical value. Beyond this point, upon further increase of c/a, the gap reopens, but the energy bands do not show inversion – the conduction band is Bi $6p_z$-derived, and the valence band is mostly Se $4p_z$-derived throughout the Brillouin Zone, as shown in Fig. 5.1(c), (d). Thus, the system undergoes a transition from a topological state to a trivial state as c/a is increased. In Fig. 5.2(a), we plot the evolution of the bulk band gap E_g with c/a, and assign positive (negative) values to the case of inverted (non-inverted) bands. The gap varies almost linearly within the range we consider, and the critical c/a at which the transition occurs is approximately 7.42.

In Fig. 5.2(b), we show the evolution of the absolute (not relative to the chemical potential) energies of the Bi p_z- and Se p_z-derived states at Γ as a function of the c/a ratio. We find that the energies of the Bi p_z levels at Γ are almost unchanged as c/a is increased (slope 0.03 ± 0.02 eV) In contrast, the energy of Se p_z levels varies considerably, and is nearly linear in c/a with the slope -0.65 ± 0.03 eV. Since the slope of the Bi p_z-level is very close to zero, and the separation between the Bi and Se p_z-levels is almost equal to the band gap (though the 'camelback' structure near the valence band maximum, see Fig. 5.1, reduces the band gap slightly compared to this separation), the slope of the Se p_z levels in Fig. 5.2(b) is very close to that derived from the evolution of the band gap in Fig. 5.2(a), which is -0.58 ± 0.01 eV.

To investigate the roles of the relativistic spin-orbit coupling and van der Waals interactions, at each value of c/a, we turn off these two effects in our calculations, optimize the lattice parameters to stay in the ground state, and monitor the variations in the Bi p_z and Se p_z levels at Γ. Inclusion of van der Waals interactions changes the lattice constants and other structural parameters [63, 64, 50] and the total energy for each c/a. Therefore we find that the chemical potential shift between the calculations with and without vdW and SOC is also a function of the c/a ratio. To facilitate a comparison between the two cases, we now reference the energies of both Bi and Se states to the respective chemical potentials, set in the middle of the gap at $T = 0$, and plot both in Fig. 5.2(c).

Importantly, we find that the change in the energy of these states near the Γ-point depends only weakly on the SOC and vdW interactions. In Fig. 5.2(c), the empty (filled) symbols show the Bi (triangles) and Se (squares) p_z level energies at Γ without (with) SOC and vdW. As expected, we observe the inversion: without SOC+vdW, the Bi (Se) state is above (below) the chemical potential. Inclusion of spin-orbit interaction inverts the levels and leads to a topological state. What is striking in Fig. 5.2(c) is that the evolution (the slope) is nearly identical for both cases. The slopes of the Se p_z levels in Fig. 5.2(c) are -0.306 ± 0.004 eV and -0.32 ± 0.03 eV with and without SOC+vdW respectively. The slopes of Bi levels are also essentially the same, but with opposite signs. We conclude that the *change in the energy of* the states closest to the chemical potential does not depend strongly on SOC+vdW corrections.

In summary, as we tune Bi_2Se_3 towards the topological transition, the quintuple layers remain largely intact, while the interlayer distance changes significantly. The energy of the states dominated by the electrons in the outer (Se) atomic planes changes much more than the energy of those originating in the inner (Bi) layers, suggesting that the interlayer interaction is the main driver of the transition. Finally, the variations of these energies with c/a are not affected by the vdW and SOC corrections (even though the absolute energies

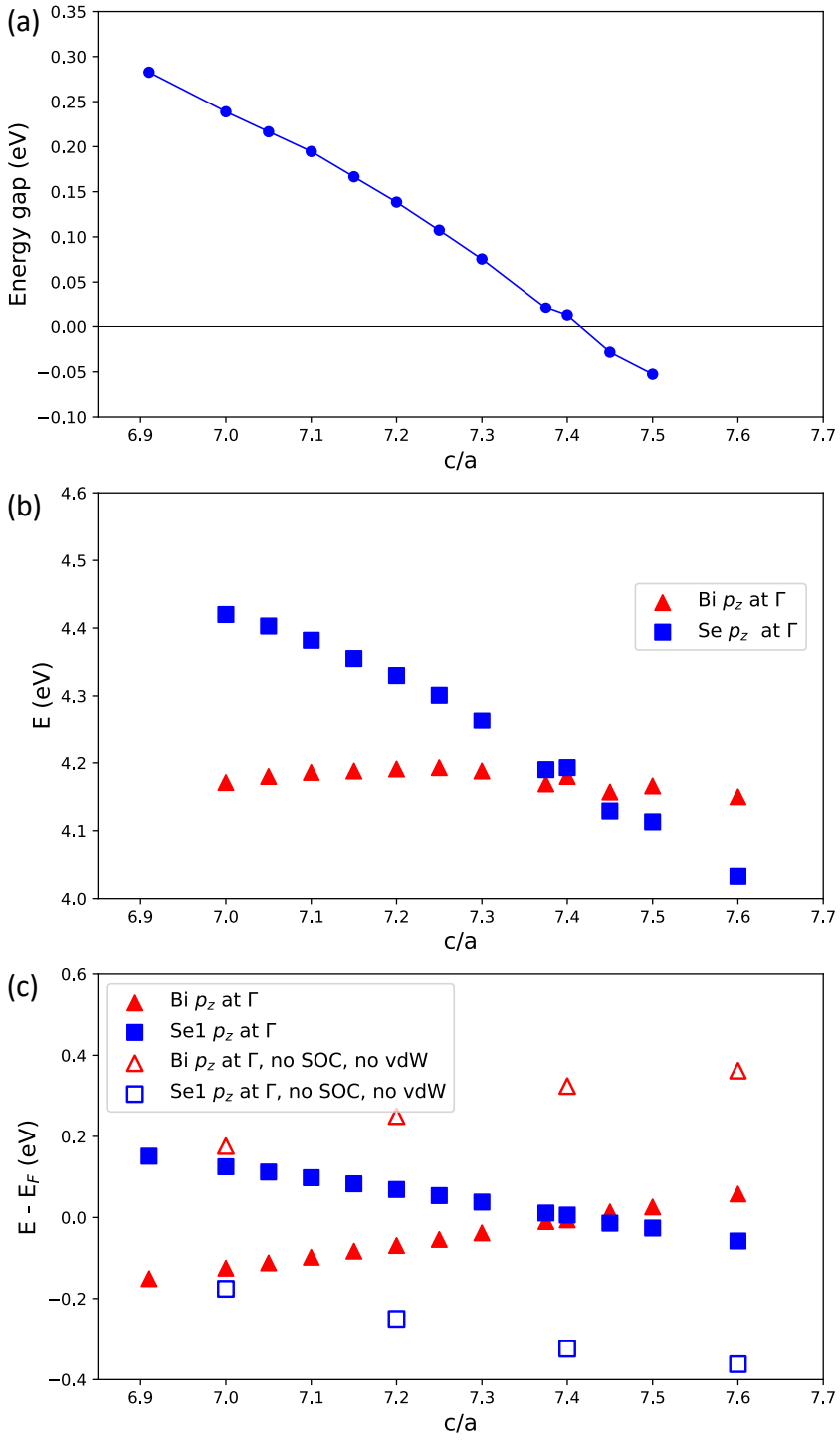

Figure 5.2. Evolution of parameters with c/a for the topological phase transition in Bi_2Se_3. (a) Variation of the band gap; (b) change in the Bi p_z and Se p_z states' energies at Γ; (c) change of these energies relative to the chemical potential. Red (blue) filled symbols show the energies of the Bi p_z (Se p_z) levels for calculations including SOC and vdW interactions, whereas red (blue) unfilled symbols in panel (c) show the energies of the Bi p_z (Se p_z) levels for calculations in which neither SOC nor vdW interactions are included.

are). We therefore conclude that the topological transition appears to be driven largely by the inter-QL Coulomb physics contained in the exchange-correlation functional. A natural question is whether these features are universal across the entire family of these compounds.

5.3 Topological phase transitions in Sb_2Se_3, Bi_2Te_3 and Sb_2Te_3

5.3.1 Predicted topological insulator Sb_2Se_3

Sb_2Se_3, in the rhombohedral structure identical to that of Bi_2Se_3, was initially thought to be a trivial insulator [8, 112, 116, 113, 114] in the ground state. These studies used the PBE-optimized structure in their calculations and did not include the van der Waals correction when obtaining this result (Ref. [112] optimized the structure including the van der Waals correction, but did not use that structure for the rest of their calculations). The effects of applying uniaxial [112] and hydrostatic [113] pressure on Sb_2Se_3 have been studied before. Ref [112] found a topological phase under compressive longitudinal strain, when the lattice constant c is decreased by more than 2% from its equilibrium value. Ref. [113] found that under hydrostatic pressures close to and greater than 1.0 GPa, the material is driven into a topological phase.

More recent studies [70, 71] included the van der Waals correction in the structural optimizations and predicted ground-state Sb_2Se_3 to be a topological insulator. They also studied the application of strain: Ref. [70] included the vdW interactions in the form of the DFT+D2 method, and reported that under a tensile strain of 3% along the c-axis, the material becomes a trivial insulator. Ref. [71] ran structural optimizations using various vdW methods (optB86b-vdW, optB88-vdW, optPBE-vdW and DFT-TS), and found that under the application of a tensile strain, the material is driven into a trivial phase and loses the inverted band structure.

Our results confirm the conclusions of these studies. When we use PBE-GGA for structural optimization, we obtain the ground-state to be a trivial insulator, in agreement with Refs. [112, 113]. Upon including the vdW interactions in our calculations, we find that the ground-state of Sb_2Se_3 is a topological insulator (see the later part of this chapter), with a band gap of $E_g \approx 0.152$ eV. This can be seen in Fig. 5.3(a) and Fig. 5.3(b), which show the inversion of the bulk bands when projected onto the Sb p and Se p orbitals in the ground state, $c/a = 7.137$.

To confirm the existence of the topological surface states for c/a values in which Sb_2Se_3 exhibits inverted bands, we run slab calculations using both 5 QL-thick and 12 QL-thick slabs with vacuum thicknesses of 100 Å. As an example, for $c/a = 7.0$, the surface states in a 5 QL-thick slab are gapped, and their spatial profile reveals a significant overlap between states localized at opposite surfaces of the slab. Hybridization between the two surface states is almost eliminated for a 12 QL-thick slab, where we obtain the Dirac-like gapless topological surface states, shown in Fig. 5.3(c). The atoms which are allowed to relax only have movements of the order of mÅ(milli-Angstrom), confirming that the slabs are stable and do not suffer from large forces. The longer decay length, ~ 3 QLs, in Sb_2Se_3 compared to ~ 1 QL in Bi_2Se_3 and Bi_2Te_3, is in agreement with Ref. [71], and is consistent with having a smaller bulk energy gap than in Bi-based materials.

When we run slab calculations using a 12 QL-thick slab using the optimized structure

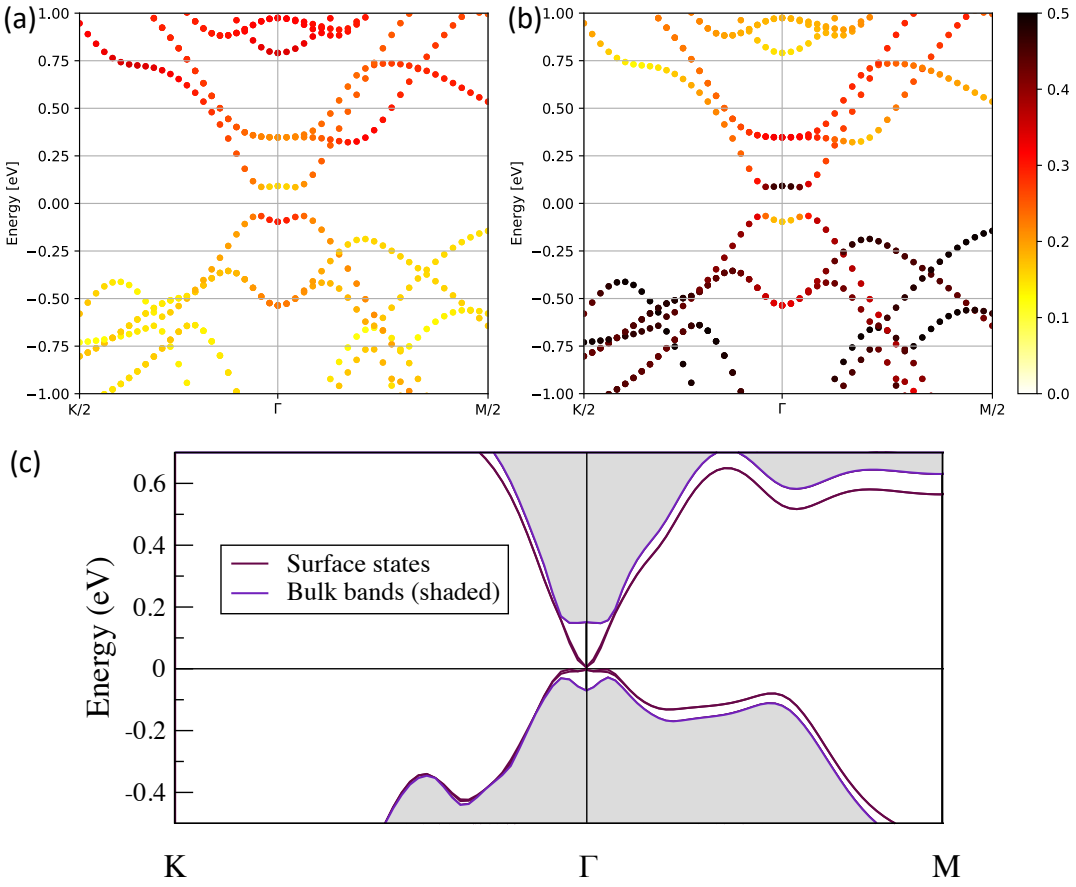

Figure 5.3. Bulk band structure projections and slab band structure for Sb_2Se_3. Band structure projections onto (a) Sb $5p$ and (b) Se $4p$ for $c/a = 7.137$ (topological insulating state). The bands below the chemical potential in (a) away from Γ have negligible contribution from Sb p, and can hence barely be seen. (c) Topological surface states for $c/a = 7.0$ for a 12 QL-thick slab, with 100 Å vacuum.

for $c/a = 7.549$, a value where the material does not display band inversion in the bulk, as expected we find that there are no topological surface states. Thus, we confirm that the band inversion in our calculations is a reliable test for the topological nature of these materials.

5.3.2 Topological phase transitions in Sb_2Se_3, Bi_2Te_3 and Sb_2Te_3

We are now in position to investigate the common features and differences of the topological phase transitions in the entire family of Bi/Sb Se/Te materials. We continue to use the ratio c/a as a tuning parameter that separates the effects of the hydrostatic pressure from that of strain and stress, and allows a more direct analysis of the competing energy scales. Bi_2Te_3 and Sb_2Te_3 are known [12, 14] to have inverted bands in their ground state, and we confirmed this in our calculations. When we allow the systems to fully relax, we find that the ground states of Bi_2Te_3 and Sb_2Te_3 occur at $c/a = 7.18$ and $c/a = 7.29$ respectively. The optimized ground-state volumes differ by 0.4% and 0.7% from their respective experimental values [76, 125].

Upon increasing c/a, we find phase transitions to trivial insulating states analogous to that in Bi_2Se_3 in all three materials, Sb_2Se_3, Bi_2Te_3 and Sb_2Te_3. While the QLs do not change substantially, the inter-QL distances increase significantly as c/a increases: the changes in the inter-QL distances are two orders of magnitude greater than those of the bond lengths, see the detailed results in the later part of this chapter. From these we determined the critical values of c/a as ≈ 7.46, 8.15, 7.86 for Sb_2Se_3, Bi_2Te_3 and Sb_2Te_3 respectively.

Similar to Bi_2Se_3, to elucidate the role of SOC and vdW interactions, we carried out the calculations where we turned them off for comparison. For example, in Sb_2Se_3 we compared the results for the cases of including (i) SOC and vdW, (ii) vdW but no SOC, (iii) SOC but not vdW, and (iv) neither SOC nor vdW, see the later part of this chapter. We find that the SOC has negligible effect on the lattice constants, and the optimized lattice constants for a given c/a value for cases (i) and (ii) are almost identical, as are (iii) and (iv). The bond lengths differ by less than $\sim$0.03%. The optimized inter-QL distance is only slightly more sensitive to the spin-orbit coupling: it is $\sim$0.5% smaller with SOC than when SOC is not included. This is consistent with the picture of spin-orbit as a local interaction. It is responsible for the band inversion, but does not affect the lattice constants significantly.

In contrast, the vdW correction changes the lattice constants: for a fixed c/a, both c and a decrease by $\sim$1.9%, while the inter-QL distance decreases by $\sim$7.3%, with the bond lengths decreasing by $\sim$0.8%. Thus, the vdW correction has a significant effect on the structural parameters. We verified that vdW interaction only changes the electronic structure via its effect on the lattice: if we compute the electronic structure for a fixed set of lattice parameters with and without vdW interaction, the band gap and other electronic parameters remain essentially unchanged.

We summarize these results in Figure 5.4, which shows the energies of the Bi/Sb p_z and Se/Te p_z states at Γ, as a function of c/a. In analogy to Fig. 5.2(c) we set the chemical potential in the middle of the gap in all cases. While in Sb_2Se_3, just as in its Bi counterpart, only the absolute energy of the band states originating from the outer Se layers change with c/a, in the Te compounds both Te and Bi/Sb p_z level energies vary despite the QL layers and bond lengths remaining essentially unchanged. This is likely due to the closer electronegativities and atomic sizes of Bi/Sb and Te, and leading to a more covalent (less

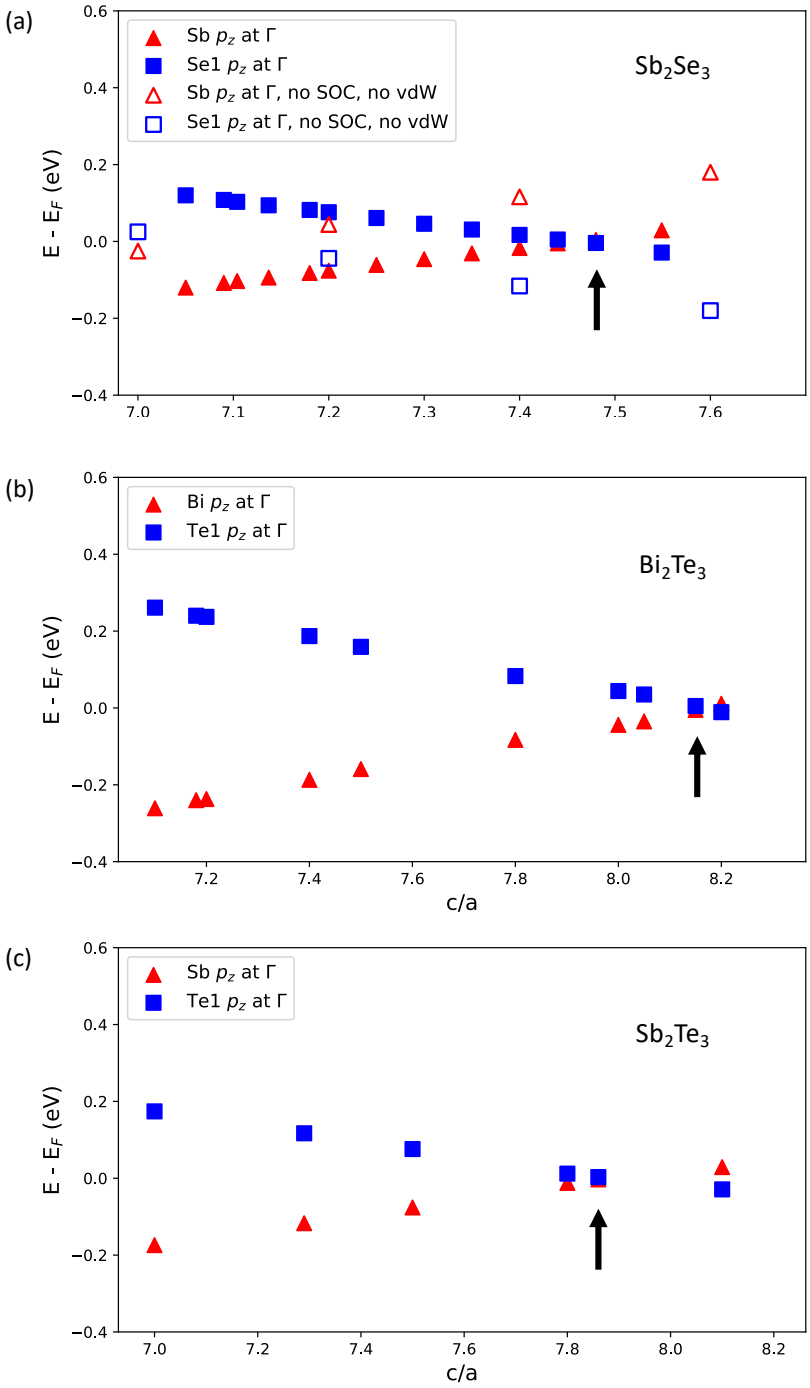

Figure 5.4. Dependence of the energies of the Bi/Sb p_z and Te/Se p_z states on c/a in Sb_2Se_3, Bi_2Te_3 and Sb_2Te_3 at Γ. Red (blue) filled markers show the energies of the Bi/Sb p_z (Te/Se p_z) levels for calculations including SOC and vdW interactions. Black arrows indicate the closing of the band gap and occurrence of the topological phase transition. (a) The red and blue unfilled markers show the energy levels of Sb_2Se_3 in calculations including neither SOC nor vdW. (b) Bi_2Te_3. (c) Sb_2Te_3.

ionic) bond between them. As a result, the shift in the energy of the electrons in the outer atomic sheet of the QL is reflected in the corresponding change of Bi/Sb levels. Plotting the energies relative to the mid-gap allows comparison across all four members of the family.

In analogy to Bi_2Se_3, we find that the energies of the states derived from the Se/Te and the Bi/Sb p-electrons in all three materials vary linearly with c/a. Bi_2Te_3 has the largest initial splitting between the Bi and Te p_z levels at Γ of ~ 0.5 eV. While the energy and relative position of the levels depend on the inclusion of SOC and vdW, these only weakly influence the slope of the line. For example, in Sb_2Se_3, this slope is 0.294 ± 0.002 eV (0.344 ± 0.006 eV) with (without) including SOC+vdW, relatively close to the value for Bi_2Se_3. We find that the slopes of the Te p_z levels in the Te compounds are smaller than those for the Se p_z levels in the Se-based TIs: -0.243 ± 0.003 eV for Bi_2Te_3 and -0.190 ± 0.007 eV for Sb_2Te_3. This suggests that the evolution of the material towards the topological phase transition depends more on the nature of the elements in the outer atomic planes of the quintuple layers (Se and Te).

1. Data for Bi_2Se_3 with SOC, DFT-D2 correction: (GGA-PBE + DFT-D2 vdW + SOC)

Table 5.1. The table below contains the results for the minimum energy, lattice constants a and c, inter-QL distance (d_{QL}), Se-Se atom spacing between QLs, Bi-Se1 and Bi-Se2 bond lengths, volume V, and band gap of Bi_2Se_3 as a function of c/a.

c/a	E_0 (eV)	a (Å)	c (Å)	d_{QL} (Å)	d_{Se-Se} (Å)	d_{bond} (Å)	V (Å^3)	E_g (eV)
6.75	-68.590	4.164	28.108	2.451	3.433	2.873, 3.056	422.10	0.296
6.91*	-68.611	4.139	28.611	2.545	3.491	2.871, 3.057	424.56	0.283
7.00	-68.610	4.128	28.896	2.607	3.532	2.870, 3.057	426.45	0.239
7.05	-68.606	4.120	29.049	2.633	3.548	2.869, 3.058	427.13	0.217
7.10	-68.600	4.113	29.205	2.661	3.566	2.869, 3.059	427.92	0.195
7.15	-68.592	4.107	29.363	2.692	3.587	2.868, 3.060	428.85	0.167
7.20	-68.581	4.100	29.519	2.722	3.608	2.868, 3.060	429.68	0.138
7.25	-68.568	4.093	29.676	2.756	3.630	2.868, 3.060	430.58	0.107
7.30	-68.552	4.088	29.839	2.791	3.655	2.866, 3.062	431.76	0.076
7.375	-68.524	4.080	30.092	2.854	3.701	2.866, 3.062	433.86	0.021
7.40	-68.513	4.076	30.161	2.861	3.704	2.866, 3.063	433.92	0.013
7.45	-68.491	4.072	30.338	2.912	3.743	2.865, 3.063	435.69	-0.028
7.50	-68.466	4.065	30.488	2.935	3.758	2.865, 3.065	436.33	-0.053
7.60	-68.411	4.055	30.816	3.012	3.815	2.864, 3.067	438.78	-0.116

*: ground-state

We find the ground-state to be at $c/a = 6.91$. We also find that as the c/a ratio increases, c increases and a decreases, see table. The inter-QL distance (between QLs) increases significantly ($\sim 13\%$ from $c/a = 7.0$ to 7.5), whereas the bond lengths (within the QL) change very little ($\sim 0.2\%$ from $c/a = 7.0$ to 7.5), see Fig. 5.5. The volume increases almost linearly with c/a. Finally, we find that the band gap (in the topological case, we assign a positive sign to the value, whereas for the trivial case, we assign a negative sign) decreases and closes at a critical value of c/a. Upon increasing c/a further, the gap reopens without band inversion. We predict that a topological phase transition occurs near $c/a = 7.4$.

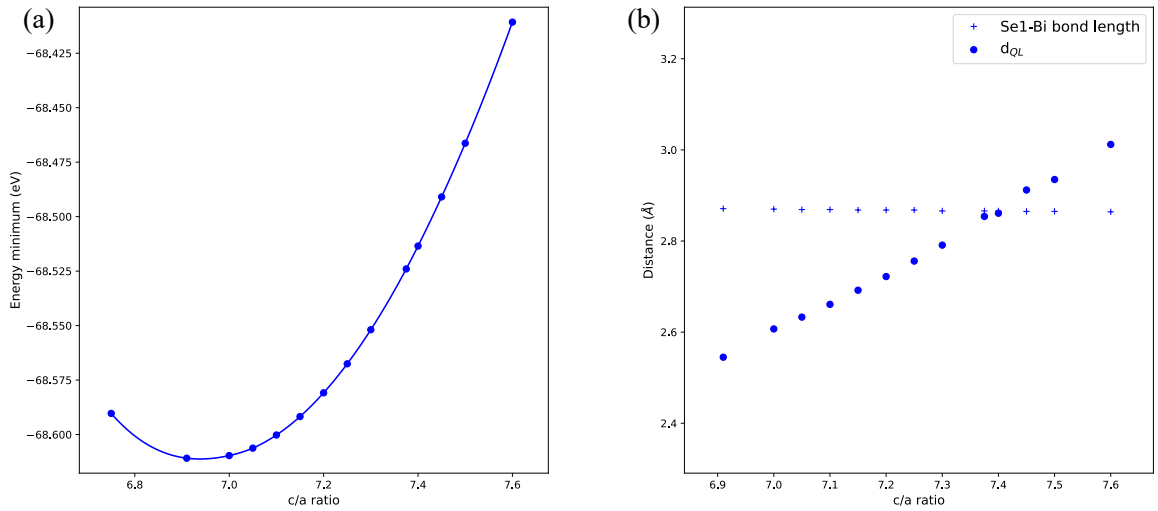

Figure 5.5. (a) Energy minimum for each c/a for Bi_2Se_3 and (b) inter-QL distance and bond length, as a function of c/a.

Close to the topological phase transition, we find the stresses in the (xx, yy, zz) directions to be approximately (+0.60, +0.60, -1.19) GPa.

2. (a) Data for Sb_2Se_3 with SOC, DFT-D2 correction: (GGA-PBE + DFT-D2 vdW + SOC)

Table 5.2. The table below contains the results for the minimum energy, lattice constants a and c, inter-QL distance (d_{QL}), Se-Se atom spacing between QLs, Sb-Se1 and Sb-Se2 bond lengths, volume V, and band gap of Sb_2Se_3 as a function of c/a.

c/a	E_0 (eV)	a (Å)	c (Å)	d_{QL} (Å)	d_{Se-Se} (Å)	d_{bond} (Å)	V (Å^3)	E_g (eV)
7.050	-65.176	4.038	28.464	2.682	3.553	2.803, 2.974	401.84	0.179
7.090	-65.179	4.032	28.588	2.707	3.570	2.802, 2.975	402.53	0.166
7.104	-65.179	4.031	28.637	2.718	3.578	2.802, 2.975	402.99	0.160
7.137*	-65.180	4.026	28.734	2.736	3.590	2.801, 2.975	403.33	0.152
7.180	-65.179	4.020	28.866	2.764	3.609	2.801, 2.976	404.08	0.139
7.200	-65.178	4.018	28.929	2.777	3.619	2.801, 2.976	404.47	0.130
7.250	-65.173	4.012	29.088	2.811	3.643	2.800, 2.976	405.52	0.108
7.300	-65.166	4.006	29.241	2.843	3.665	2.799, 2.979	406.33	0.087
7.350	-65.156	4.000	29.398	2.877	3.689	2.799, 2.977	407.30	0.062
7.400	-65.143	3.994	29.556	2.912	3.714	2.798, 2.978	408.31	0.033
7.425	-65.136	3.991	29.636	2.930	3.728	2.798, 2.978	408.87	0.018
7.440	-65.132	3.990	29.683	2.941	3.736	2.798, 2.979	409.19	0.009
7.460	-65.125	3.987	29.747	2.953	3.745	2.798, 2.980	409.61	0.002
7.480	-65.118	3.984	29.800	2.959	3.747	2.798, 2.980	409.62	-0.009
7.549	-65.093	3.979	30.037	3.024	3.798	2.797, 2.980	411.85	-0.057

*: ground-state

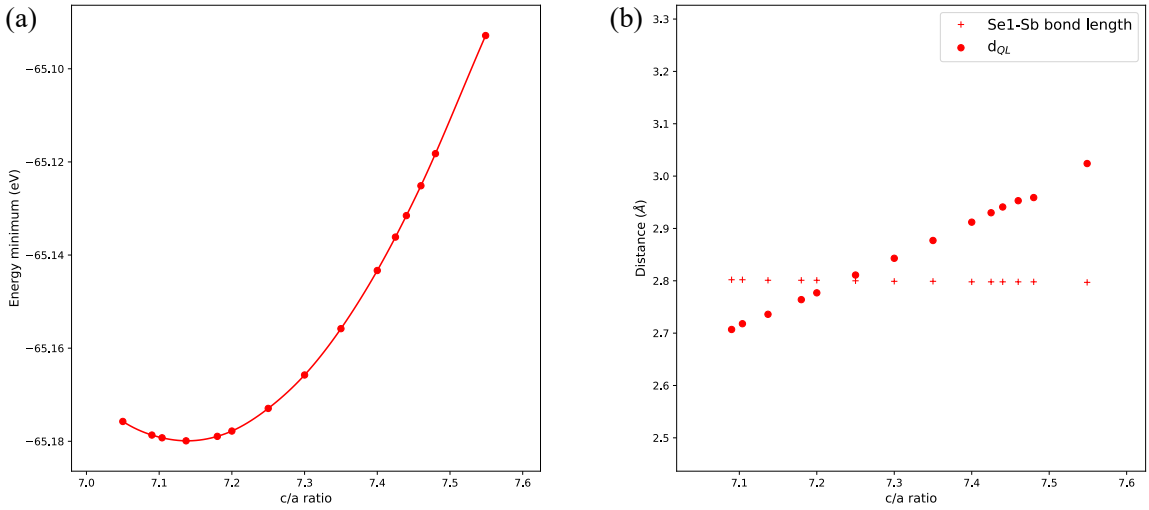

Figure 5.6. (a) Energy minimum for each c/a for Sb_2Se_3 and (b) inter-QL distance and bond length, as a function of c/a.

We predict the ground-state to be at $c/a = 7.14$. We find that the inter-QL distance (between QLs) increases significantly ($\sim$ 13% from $c/a = 7.0$ to 7.5), whereas the bond lengths (within the QL) change very little ($\sim$ 0.2% from $c/a = 7.05$ to 7.55), similar to Bi_2Se_3, see Fig. 5.6. The volume increases almost linearly with c/a. We predict the critical value of c/a to be near $c/a = 7.46$.

We find that the stress values in the (xx, yy, zz) directions near the phase transition at $c/a \sim 7.46$ are (+0.48, +0.48, - 0.97) GPa.

2. (b) Data for Sb_2Se_3 with DFT-D2 correction, no SOC: (GGA-PBE + DFT-D2 vdW)

Table 5.3. In the table below, we show the results for the minimum energy, lattice constants a and c, inter-QL distance (d_{QL}), Sb-Se1 and Sb-Se2 bond lengths, volume V, and band gap of Sb_2Se_3 as a function of c/a.

c/a	E_0 (eV)	a (Å)	c (Å)	d_{QL} (Å)	d_{bond} (Å)	V (Å^3)	E_g (eV)
7.00	-64.656	4.046	28.321	2.668	2.801, 2.973	401.46	0.024
7.20	-64.666	4.018	28.928	2.778	2.800, 2.976	404.43	0.030
7.40	-64.633	3.993	29.545	2.907	2.798, 2.978	407.88	0.059
7.60	-64.560	3.972	30.958	3.053	2.795, 2.981	412.32	0.181

2. (c) Data for Sb_2Se_3 with SOC, without DFT-D2 correction: (GGA-PBE + SOC)

Table 5.4. In the table below, we show the results for the minimum energy, lattice constants a and c, inter-QL distance (d_{QL}), Sb-Se1 and Sb-Se2 bond lengths, volume V, and band gap of Sb_2Se_3 as a function of c/a.

c/a	E_0 (eV)	a (Å)	c (Å)	d_{QL} (Å)	d_{bond} (Å)	V (Å^3)	E_g (eV)
7.00	-60.756	4.112	28.784	2.800	2.828, 3.016	421.49	0.111
7.20	-60.796	4.093	29.469	2.979	2.824, 3.017	427.54	0.003
7.40	-60.814	4.080	30.190	3.186	2.821, 3.017	435.12	0.147
7.549	-60.817	4.069	30.717	3.331	2.819, 3.019	440.44	0.238

2. (d) Data for Sb_2Se_3 without DFT-D2 correction, without SOC: (GGA-PBE)

Table 5.5. In the table below, we show the results for the minimum energy, lattice constants a and c, inter-QL distance (d_{QL}), Sb-Se1 and Sb-Se2 bond lengths, volume V, and band gap of Sb_2Se_3 as a function of c/a.

c/a	E_0 (eV)	a (Å)	c (Å)	d_{QL} (Å)	d_{bond} (Å)	V (Å^3)	E_g (eV)
7.00	-60.240	4.113	28.790	2.814	2.826, 3.015	421.74	0.000
7.20	-60.282	4.093	29.470	2.988	2.823, 3.016	427.57	0.088
7.40	-60.302	4.080	30.189	3.194	2.820, 3.017	435.12	0.232
7.60	-60.306	4.068	30.917	3.404	2.817, 3.018	443.08	0.338

3. Data for Bi_2Te_3 with SOC, DFT-D2 correction: (GGA-PBE + DFT-D2 vdW + SOC)

Table 5.6. The table below contains the results for the minimum energy, lattice constants a and c, inter-QL distance (d_{QL}), Te-Te atom spacing between QLs, Bi-Te1 and Bi-Te2 bond lengths, volume V, the band gap and the energy gap at Γ of Bi_2Te_3 as a function of c/a.

c/a	E_0 (eV)	a (Å)	c (Å)	d_{QL} (Å)	d_{bond} (Å)	V (Å^3)	E_g^1 (eV)	E_Γ (eV)
6.95	-64.791	4.384	30.482	2.625	3.075, 3.239	507.3	-	0.475
7.10	-64.812	4.358	30.941	2.709	3.072, 3.239	508.9	0.134	0.415
7.18*	-64.816	4.343	31.200	2.758	3.070, 3.239	510.2	-	0.387
7.20	-64.816	4.341	31.255	2.766	3.070, 3.240	510.1	0.128	0.365
7.40	-64.797	4.307	31.874	2.877	3.067, 3.242	512.1	-	0.315
7.50	-64.774	4.292	32.188	2.932	3.066, 3.244	513.4	0.126	0.279
7.80	-64.649	4.247	33.123	3.116	3.062, 3.246	517.3	-	0.164
8.00	-64.520	4.217	33.734	3.216	3.061, 3.254	519.5	0.086	0.087
8.05	-64.483	4.209	33.882	3.239	3.060, 3.257	519.8	-	0.070
8.15	-64.403	4.199	34.218	3.325	3.059, 3.257	522.4	-	0.009
8.20	-64.361	4.194	34.396	3.370	3.059, 3.258	524.1	-	-0.021

[1]: band gap calculated using tetrahedron DOS method using k-point grid of 15x15x15 for representative c/a values
-: the band gap was not calculated using the tetrahedron method for these c/a values
*: ground-state

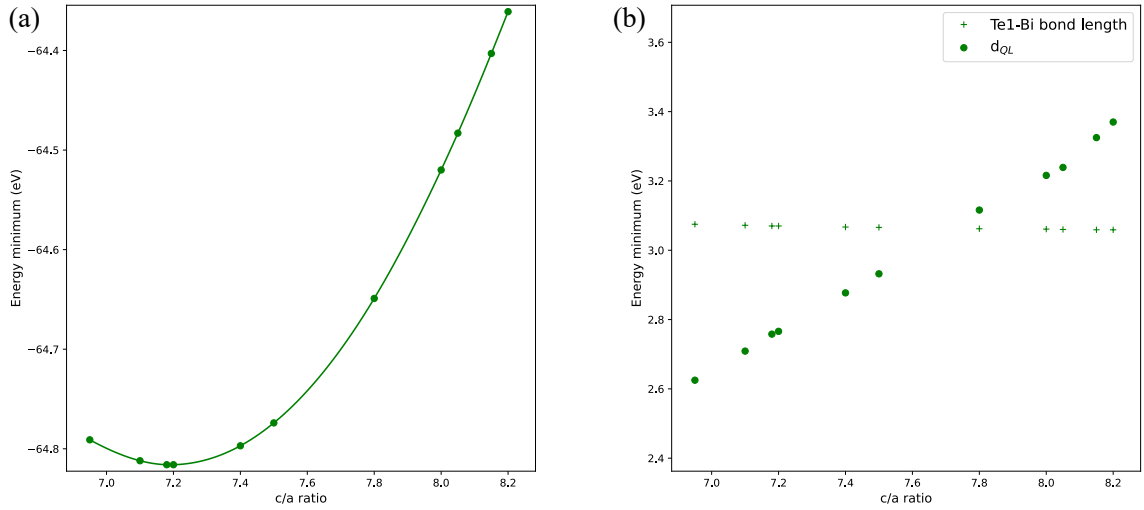

Figure 5.7. (a) Energy minimum for each c/a for Bi_2Te_3 and (b) inter-QL distance and bond length, as a function of c/a.

For this material, we obtain the ground-state to lie at $c/a = 7.18$. The ground-state volume that we obtain is 0.4% larger than that measured in experiment [76]. As c/a is increased, we find, as for the Se compounds, that the inter-QL distances increase ($\sim 24\%$ from $c/a = 7.10$ to 8.20) much more than the bond lengths ($\sim 0.4\%$ from $c/a = 7.10$ to 8.20), see Fig. 5.7. Note that the percentage increase in the inter-QL distance is much larger here than for the Se compounds simply because we examine a larger range of c/a values. We predict that a topological phase transition occurs near $c/a = 8.15$. In addition to calculating the energy gap near the Gamma point, we estimate the band gap from Density of States calculations, using a finer k-grid and the accurate tetrahedron method.

Near the topological phase transition at $c/a \sim 8.15$, we find the stresses in the (xx, yy, zz) directions to be (+1.1, +1.1, -2.1) GPa.

4. Data for Sb_2Te_3 with SOC, DFT-D2 correction: (GGA-PBE + DFT-D2 vdW + SOC)

Table 5.7. The table below contains the results for the minimum energy, lattice constants a and c, inter-QL distance (d_{QL}), Sb-Te1 and Sb-Te2 bond lengths, volume V, the band gap and the energy gap at Γ of Sb_2Te_3 as a function of c/a.

c/a	E_0 (eV)	a (Å)	c (Å)	d_{QL} (Å)	d_{bond} (Å)	V (Å^3)	E_g^1 (eV)	E_Γ (eV)
7.00	-61.620	4.296	30.072	2.763	3.006, 3.144	480.6	0.104	0.332
7.29*	-61.665	4.246	30.941	2.910	2.999, 3.148	483.0	0.148	0.235
7.50	-61.641	4.212	31.587	3.023	2.995, 3.151	485.2	0.118	0.151
7.80	-61.527	4.169	32.520	3.209	2.990, 3.156	489.5	0.023	0.023
7.86	-61.491	4.160	32.700	3.236	2.989, 3.159	490.1	-	0.006
8.00	-61.398	4.144	33.153	3.342	2.988, 3.161	493.1	-	-0.057

[1]: band gap calculated using tetrahedron DOS method using k-point grid of 15x15x15

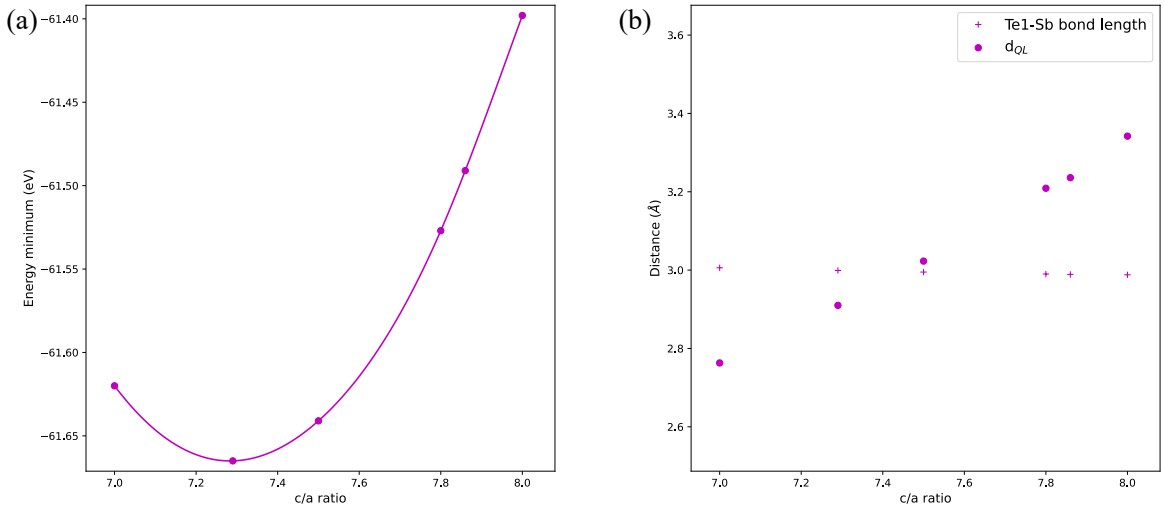

Figure 5.8. (a) Energy minimum for each c/a for Sb_2Te_3 and (b) inter-QL distance and bond length, as a function of c/a.

for certain c/a values
-: the band gap was not calculated using the tetrahedron method for these c/a values
*: ground-state

We obtain the ground-state to be at $c/a = 7.29$. We obtain a ground-state volume that is 0.7% larger than that measured in experiment [125]. We find that the inter-QL distance (between QLs) increases significantly ($\sim$ 21% from $c/a = 7.0$ to 8.0), whereas the bond lengths (within the QL) change very little ($\sim$ 0.6% from $c/a = 7.0$ to 8.0), see Fig. 5.8. Note that the percentage increase in the inter-QL distance is again larger here than for the Se compounds because we examine a larger range of c/a values. We predict the critical value of c/a to be near $c/a = 7.86$.

We find that the stress values in the (xx, yy, zz) directions near the phase transition at $c/a \sim 7.86$ are (+0.82, +0.82, –1.6) GPa.

5.4 Discussion

Our results show that the topological phase transitions, driven by tuning the ratio of the out-of-plane to in-plane lattice constants, c/a, exhibit common features in all of the chalcogenides Bi_2Se_3, Sb_2Se_3, Bi_2Te_3 and Sb_2Te_3. Structurally, as we increase this ratio, the lattice is elongated along the c-axis, with most of the change in the c-axis lattice constant due to the increase in the inter-QL distance. The compression that happens in the plane to the QLs is accompanied by small changes in the QL thickness, but the changes in the bond lengths within the QL are almost two orders of magnitude smaller than the corresponding variations in the inter-QL distances in all these compounds. The charge density along the line connecting Te1 atoms in adjacent QLs of Bi_2Te_3 exhibits small rearrangement for two different values of c/a corresponding to topological and trivial states, with faster drop-off for greater value of c/a, as shown in Fig. 5.9(a). Meanwhile the charge density along the

Bi-Te1 bond within the QL remains unchanged, see Fig. 5.9(b). Hence, structurally and electronically, the quintuple layers remain unchanged across the topological transition.

The topological transition is manifested in vanishing and reopening of the band gap, with the band inversion disappearing simultaneously. Electronic band structure calculations show that near the Γ point the energy gap, as well as the Bi/Sb-derived and the Se/Te-derived p_z-states depend quasi-linearly on c/a in the vicinity of the transition. In the topological state, these Bi/Sb-derived (Se/Te-derived) sit at the top of the valence (bottom of the conduction) band, while their order is reversed in the trivial state. The band inversion is due to the spin-orbit coupling, and without it the Se/Te p_z-states are always lower in energy than the Bi/Sb p_z-states.

Remarkably, in all four materials we find that the the slope of that linear dependence does not depend strongly on the inclusion of spin-orbit coupling. This is consistent with the picture of the quintuple layers being unchanged as c/a is varied, so that the SOC which originates mostly from Bi/Sb in the inner atomic layers is unaffected. However, our result contrasts with the scenario suggested in Ref. [112], where the strength of the SOC was argued to change with the inter-QL distance. We find no evidence of this.

We also find that the same slope is slightly affected by the inclusion of the van der Waals corrections, mostly via the change in the lattice parameters and the interlayer distance.

The emergent picture is that the initial value of the band gap, at the ground state, is strongly influenced by the interplay of the van der Waals interactions between the quintuple layers and the spin-orbit-induced band inversion. However, the evolution from that state towards the topological transition is influenced primarily by the inter-QL physics, which is determined mostly by the Coulomb interaction (contained in the density functional) with corrections due to the van der Waals interactions.

Consider, for example, the slope of the energy of the Se-derived states in Sb_2Se_3 obtained using different DFT-based methods, shown in Table 5.8, based on the data in the later part of this chapter. We find that the inclusion of SOC does not change the energy evolution of these states, while inclusion of van der Waals forces does, albeit weakly. The relative decrease in the slope upon including vdW supports our view of the dominant role of the inter-QL physics. PBE-GGA often underbinds, and hence, upon optimization, the Coulomb repulsion due to the overlapping electron clouds of the nearest neighbors in different QLs and the gradient terms cause the inter-QL spacing to increase, decreasing the band gap, and lowering the energy of the Se p_z level. In contrast, the inclusion of the attractive van der Waals interaction reduces d_{QL} when compared to that obtained by PBE-GGA, and increases the band gap (thereby increasing the energy of the Se p_z level). Therefore the slope of the dependence of the energy of Se p_z levels on c/a is smaller with the vdW corrections. Thus, it is the inter-QL coupling which influences how the energies of the Bi/Sb- and Se/Te-derived p-states at the Γ point vary with c/a. Finally, we also note that the minor differences between the slopes in Table 5.8 with and without SOC are due to the small differences between the optimized inter-QL distances in each case.

We find that the inter-QL distances d_{QL} also vary linearly with c/a (see also Ref. [118]), and find that the corresponding slopes for the two Se compounds are almost identical, as are those of the two Te compounds (see second column in Table 5.9, and the full data in the later part of this chapter). This shows that the changes in d_{QL} are determined by the type of atom in the outermost planes of the quintuple layers, Te or Se.

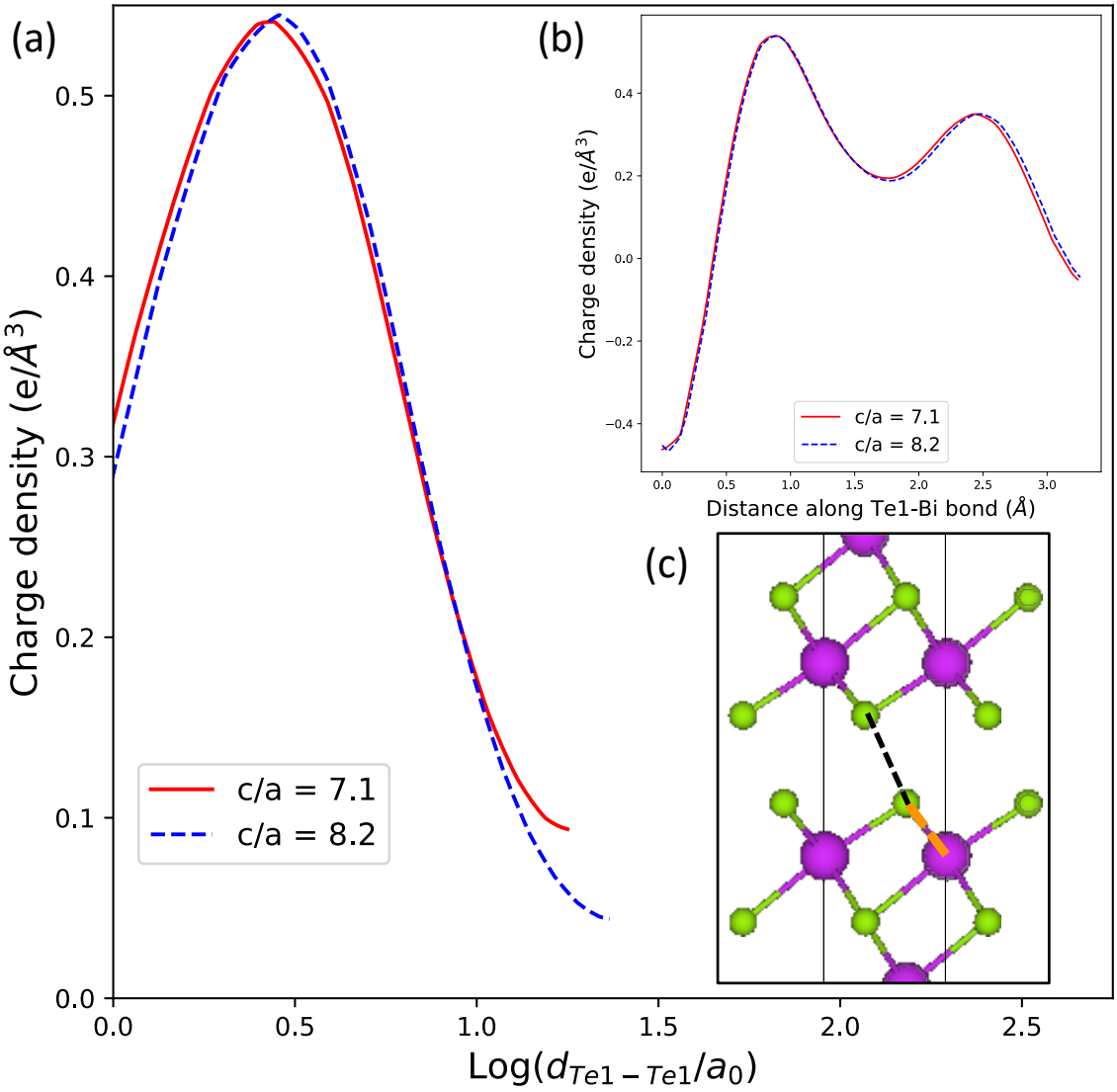

Figure 5.9. (a) Charge density of Bi_2Te_3 along line connecting Te atoms in neighboring QLs for $c/a = 7.1$ (red, solid line) and $c/a = 8.2$ (blue, dashed line), plotted up until half the atom spacing. (b) Inset shows charge densities along Te1-Bi bonds for $c/a = 7.1$ (red, solid line) and $c/a = 8.2$ (blue, dashed line). (c) Inset shows black dashed line connecting Te1 atoms between adjacent QLs ($d_{Te1-Te1}$), and orange dashed line along Te1-Bi bond.

Table 5.8. Slopes of Se p_z levels in Sb_2Se_3 as a function of c/a for calculations incorporating (i) vdW + SOC, (ii) vdW but no SOC, (iii) SOC but no vdW, and (iv) neither vdW nor SOC.

Method	Slope II (eV)
PBE-GGA + vdW + SOC	0.294±0.002
PBE-GGA + vdW, no SOC	0.290±0.004
PBE-GGA + SOC, no vdW	0.346±0.008
PBE-GGA, no vdW, no SOC	0.344± 0.006

Table 5.9. Rate of change of inter-QL distances as a function of c/a. Last two columns show the critical value of atom spacings between QLs $d_{y\text{-}y}$ (y = Te/Se), and critical atom spacings between QLs minus the corresponding ionic radii of Te/Se.

Material	Slope interlayer	Critical value	
	distance d_{QL}	$d_{y\text{-}y}$ (Å)	$(d_{y\text{-}y} - r_y^{ion})$ (Å)
Bi_2Se_3	0.66	3.7	2.7
Sb_2Se_3	0.67	3.7	2.7
Bi_2Te_3	0.58	4.1	2.9
Sb_2Te_3	0.57	4.0	2.8

Table 5.10. The slope of linear change in the chalcogenide p_z energy levels (Y1 = Se1/Te1) and band gaps E_g as a function of c/a correlates with the relative variation of the interlayer distance.

Material	Slope with respect to c/a of		
	Y1 p_z at Γ (eV)	d'_{QL}/d_{QL}	Band gap E_g (eV)
Bi_2Se_3	0.31	0.259	-0.58 ± 0.01
Sb_2Se_3	0.29	0.245	-0.46 ± 0.01
Bi_2Te_3	0.24	0.210	-0.38 ± 0.01
Sb_2Te_3	0.19	0.195	-0.39 ± 0.01

If we focus on the distances between atoms in adjacent QLs, $d_{y\text{-}y}$ (y = Te/Se, see Fig. 5.9(c) for illustration), at the value of c/a where the topological transition occurs in each material, we find that they are identical for the two Se-based compounds, and also identical, albeit at a different value, for the two Te-based materials, see Table 5.9. Change of Bi for Sb does not affect this distance. Moreover, if we account for the difference in the ionic radii between Se and Te, we find that the topological transition in all four compounds occurs at approximately the same "critical" separation between the QLs, ~ 2.8 Å. This gives predictive power to our analysis, as measurements of the changes in the lattice constants in a given experimental setup can be extrapolated to the "universal" critical value to predict the parameters for the topological transition.

We find that the energetics of the p_z levels supports the crucial role of the interlayer coupling. Among the four materials, Bi_2Se_3 displays the largest variation in the p_z level energies with respect to changing the c/a ratio, followed by Sb_2Se_3 and Bi_2Te_3, while Sb_2Te_3 displays the least variation, see the second column in Table 5.10. We conjecture that the large electronegativity difference between Bi and Se (0.53), which implies significant electron density closer to the Se atom in the Bi-Se bond, makes the Coulomb repulsion between Se atoms in different QLs stronger. In contrast, Sb and Te have close electronegativity (difference 0.05), which results in a more covalent distribution of the electrons between the two, smaller electron densities near the outermost Te, and hence weaker sensitivity to changing the inter-QL distance. Fitting the band gaps linearly yields slopes for the Te compounds which are very close, whereas the corresponding slopes for the Se compounds have a larger difference, see the third column in Table 5.10. The band gaps in the four materials are close in value to the separation between the Bi/Sb and Te/Se p_z level energies

at Γ. However, the 'camelback' structure in the valence band causes the band gap to be smaller than this separation. Small changes in the camelback structure causes the slope of the band gap to differ slightly from the slopes of the p_z levels in Table 5.10.

Both the variation of the energy gap and the change in the p_z level energy correlate with the normalized rate of change of the inter-QL distance, d'_{QL}/d_{QL} as shown Table 5.10. The ground-state inter-QL distance is the smallest in Bi_2Se_3, with Sb_2Se_3, Bi_2Te_3 and Sb_2Te_3 following in order of increasing d_{QL}. The materials with the greater relative change in the interlayer distance exhibit stronger dependence of the energy of the band states near the Γ point. This strongly supports the view that the inter-QL physics is responsible for the evolution of these energy levels.

5.5 Conclusions

While our results are in general agreement with interpreting the transition from topological to a trivial insulator as a consequence of the competition between level splitting due to hybridization and spin-orbit coupling that promotes band inversion, the underlying mechanism of inter-QL interactions is different from that suggested previously. Refs. [38, 8] considered the atomic p orbitals of Bi and Se in a single QL, and suggested the steps towards band inversion that were largely based on intra-QL physics. They first included crystal field splitting, hybridization, and level repulsion between Bi and Se, followed by inclusion of SOC. Our main conclusion here is that the QLs remain largely unchanged, and therefore SOC and Bi-Se hybridization strength do not vary almost at all within the considered range of the lattice constants. In that language, the ligand-induced splitting of the p-electron manifold of Se/Te is the driving force behind the topological phase transition, with the important caveat that the changes in this splitting are almost entirely due to inter-QL interaction. While the pressure effect on the splitting of the energy levels obviously has been identified before [112, 113] we are not aware of any work making unambiguous connection of the topological transition with the inter-QL physics.

Our results allow us to make conjectures about the topological phase transitions in the alloys of the materials we studied. The original interest in alloying arose because, with Sb_2Se_3 predicted to be a trivial insulator, the alloy $(Bi_{1-x}Sb_x)_2Se_3$ was expected [69] to undergo a topological phase transition (TPT) at a critical value of x. Given the current results showing that this end material is a topological insulator, the question of whether the transition in the alloys exists, and, if yes, what its nature is, remains open, and will be addressed by us in detail in future work.

In Fig. 5.10, we show the variation of the gaps near Γ as a function of c/a. Note that, while in the Se compounds the minimal gap is always near the Γ point, we find that, away from the critical value of c/a, the gap in the Te compounds is not at the center of the Brillouin Zone. Hence we plot the gap in the density of states and the gap at the Γ point separately, as only the latter is relevant for the topological transition. We can think of alloying as both producing the chemical pressure and introducing disorder in the on-site energies of the p_z levels. The critical c/a values of Bi_2Se_3 and Sb_2Se_3 are very close, and hence it is not likely that (Bi-Sb) alloying in Se-based material at ambient pressure yields a topological phase transition. It is possible, of course, that the difference in the SOC strength on Bi and Sb conspires with the optimized lattice constants at a given x to remove the band inversion,

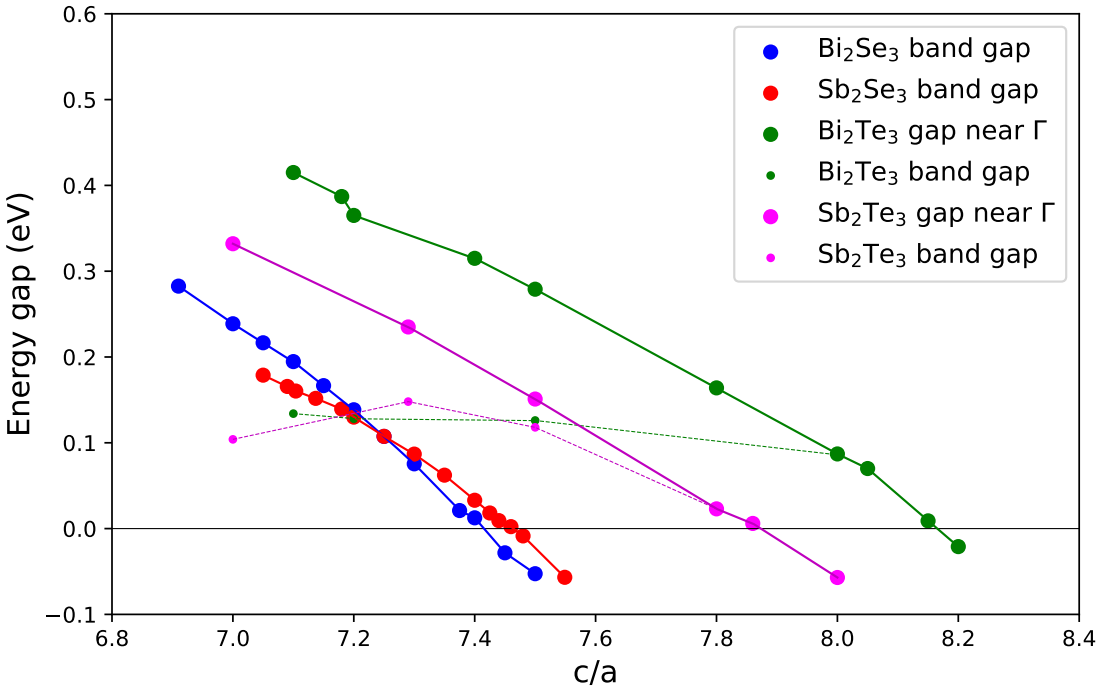

Figure 5.10. Bulk band gaps and gaps near Γ of Bi_2Se_3, Sb_2Se_3, Bi_2Te_3 and Sb_2Te_3 as a function of c/a.

but this would be accidental fine-tuning of parameters in the bulk. Ref. [69] reported that in $(Bi_{1-x}Sb_x)_2Se_3$ semimetallic states appear over a range of concentrations between $x = 0.78$ and $x = 0.83$, rather than at the single transition point, as would be expected. Hence it is important to revisit this issue.

Experiments [16] have shown the existence of the Dirac surface states in $(Bi_{1-x}Sb_x)_2Se_3$ grown on Bi_2Se_3 up to at least x=0.7. Note that we performed a bulk calculation with full relaxation of the volume for each value of c/a. In thin films grown on a substrate the in-plane lattice constant is fixed, and hence the critical inter-QL distance will differ from that in the bulk. We also leave this for future studies, and are currently carrying out calculations to investigate the topological nature of the alloys under these conditions.

Returning to the bulk systems, the topological transitions for Bi_2Te_3 and Sb_2Te_3 happen at quite different c/a values, and an alloy of the two could thus display a TPT as the concentrations of Bi and Sb atoms are varied. For the same reason, we suggest that it might be possible to observe a TPT in $Bi_2(Te_ySe_{1-y})_3$ by varying the concentration y. In fact, additional work is needed to determine whether such alloying yields a different concentration of Se and Te in the middle and outer atomic sheets of the quintuple layers, and whether it induces reconstruction of the outer atomic layers, which would, according to our results, have a strong effect on the topological properties.

In summary, we investigated the topological transition in stoichiometric tetradymite topological insulators using the ratio of the lattice constants as a tuning parameter. Our main conclusion is that in all the materials studied this transition is driven by the inter-QL Coulomb and van der Waals interactions between the outer atoms in the quintuple layers, and therefore the inter-QL distance is the key tuning parameter that controls this transition. We identified van der Waals forces and the nature of the intra-QL bonding that determines the charge distribution between the layers as main factors in controlling the approach to such transitions. Our results suggest pathways towards realization of the topological phase transitions in bulk materials and thin films.

CHAPTER 6.

EFFECTS OF DISORDER IN THE CHALCOGENIDE TOPOLOGICAL INSULATORS

In the previous chapter, the topological phase transitions arising from the application of strain on the lattice structure were investigated as a function of the c/a ratio. A related question that arises is: what effect will disorder, which induces chemical pressure[21, 22, 23, 24, 25, 26], have on these materials? In practical situations, samples of Bi_2Se_3 and Bi_2Te_3 are conductors in the bulk because their Fermi levels lie in the bulk conduction and valence bands respectively [128]. This is aided by the formation of Se vacancies in Bi_2Se_3 and Bi/Te anti-site defects in Bi_2Te_3. However, to observe and use the topological surface states of these materials, it is important for them to be insulating in the bulk, so as to be able to isolate the conduction from the surface. Alloying the 3D topological insulators is relevant in the current context because the Fermi level can be tuned to fall within the bulk band gap by carefully choosing the alloy composition. Ref. [69] ran first-principles calculations and reported that the alloy $(Bi_{1-x}Sb_x)_2Se_3$ undergoes a topological phase transition at a critical value of the Sb concentration x. Since they didn't include the van der Waals interactions in their DFT calculations, they found Sb_2Se_3 to be a trivial insulator in its ground state. However, Sb_2Se_3 has been subsequently predicted to be a topological insulator in its ground state in more recent studies [70, 71], and thus both end-point materials are topological. This brings about the question of whether a topological phase transition occurs at intermediate concentrations. In this chapter, I describe the results of investigating the topological nature of alloyed 3D TIs at different compositions.

To estimate the alloy's lattice constants, the authors in Ref. [69] linearly interpolated between those of Bi_2Se_3 and Sb_2Se_3. As a result, at $x = 0.78$, a concentration at which they report that the gap is closed, the lattice constants would be $a = 4.116$ Å, and $c = 30.707$ Å, with a c/a ratio of 7.46. This value of c/a is the critical c/a at which Sb_2Se_3 undergoes a topological phase transition to a trivial insulating state and Bi_2Se_3 is already in a trivial state. Thus, it is unknown whether the predicted semimetallic states in the alloy arise due to a topological phase transition or whether it is an accidental closing of the band gap.

In this chapter, I describe the results of a study of the ground-state of the $(Bi_{1-x}Sb_x)_2Se_3$ alloy at different compositions. While the calculations and analysis are ongoing, the results show that the intermediate concentrations $x = 0.5$, $x = 0.625$ and $x = 0.75$ are all trivial insulators in their ground states, whereas the end-point materials $x = 0.0$ and $x = 1.0$ are topological insulators. Partially ordered supercells were used in the first-principles calculations to study the alloy.

6.1 Computational Details

The unit cell for the alloy consists of a 4x4x1 supercell of the conventional hexagonal unit cells for the ordered materials generated using the SCRAPS technique [129]. It contains 240 atoms and has been set up in such a way that the atomic pair correlations are zero up to the third nearest neighbor. Simulating disordered materials usually involves running calculations for an ensemble of different configurations to mimic the random arrangement

Table 6.1. Results for the optimized structural and electronic parameters of $(Bi_{1-x}Sb_x)_2Se_3$ for different compositions x. The end-point materials are also included. The band gaps in the trivial insulating state are assigned a negative sign.

x	E_0 (eV)	c/a	a (Å)	c (Å)	d_{QL} (Å)	d_{Se-Se} (Å)	E_g (eV)
0.0	-1097.77	6.91	4.139	28.611	2.545	3.491	0.283
0.5	-1065.87	7.31	4.084	29.852	3.056	3.860	-0.110
0.625	-1060.67	7.32	4.069	29.804	3.051	3.851	-0.099
0.75	-1054.39	7.31	4.059	29.682	3.039	3.837	-0.088
1.0	-1042.88	7.137	4.026	28.734	2.736	3.590	0.152

of impurities. However, the supercells in these calculations do not require configurational averaging because the short-range order is negligible up to the third nearest neighbors.

Structural optimization is carried out by running cell shape and volume relaxation. For each composition, I used Vegard's law [130] to predict a starting guess for the lattice constant a of the alloy:

$$a_{(Bi_{(1-x)}Sb_x)_2Se_3} = (1-x)a_{Bi_2Se_3} + xa_{Sb_2Se_3}, \tag{6.1}$$

in which I used the ground-state lattice constants of Bi_2Se_3 and Sb_2Se_3.

For the composition $x = 0.75$, we run a calculation in which the lattice constants are fixed such that the c/a ratio is 6.9, a value close to the ground-state c/a value of Bi_2Se_3.

Calculation for 2x2x1 supercells of Bi_2Se_3 are also run in which a single Bi atom is replaced by Sb, corresponding to a concentration of $x \sim 0.02$. In this calculation, the atoms, cell shape, and volume are allowed to relax.

Band structure projections are plotted using PyPROCAR [127] and band inversion is used to determine the topological nature of the alloys.

6.2 Predicted phase transitions in $(Bi_{1-x}Sb_x)_2Se_3$

The results for the ground-state energies, lattice parameters and band gaps are shown in Table 6.1. When the atoms are kept fixed and the cell shapes and volumes are allowed to relax, the ground-states of the $x = 0.5$, $x = 0.625$ and $x = 0.75$ compositions surprisingly all have c/a values that lie close to 7.3, indicating that the change in composition close to these values does not affect the optimum c/a value. The lattice constant a decreases as the concentration x is increased, but the lattice constant c and the inter-QL distance d_{QL} first increase from $x = 0.0$ to $x = 0.5$, and then drop for the remaining compositions until $x = 1.0$.

The ground-states for the intermediate concentrations $x = 0.5$, $x = 0.625$ and $x = 0.75$ included here are found to be trivial insulators, whereas the end-points are topological.

In Fig. 6.1, the bulk band structure for the ground-state of the 2x2x1 supercell corresponding to $x \sim 0.02$ is shown, projected onto the Bi p orbitals. The bands are inverted, with the Bi p orbitals being located below the chemical potential near Γ. Note that at $x = 0.0$, the bands are inverted.

In Fig. 6.2, the bulk band structure for $x = 0.75$ for $c/a = 6.9$ is shown projected onto the Bi p orbitals. The obtained band structure is metallic; however, we can see that the

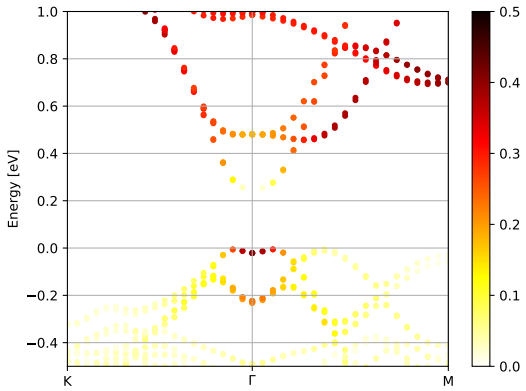

Figure 6.1. Bulk electronic structure of $(Bi_{1-x}Sb_x)_2Se_3$ at $x \sim 0.02$, projected onto Bi p orbitals, showing a topological insulating state.

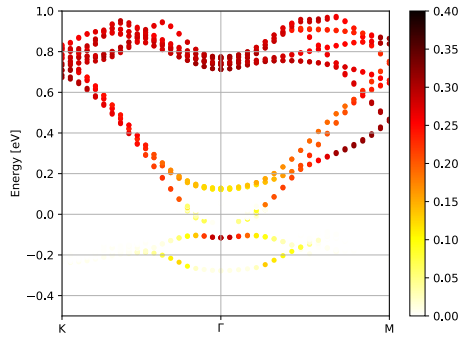

Figure 6.2. Bulk electronic structure of $(Bi_{1-x}Sb_x)_2Se_3$ at $x = 0.75$, $c/a = 6.9$, projected onto Bi p orbitals, showing a metallic state with band inversion.

bands are inverted. However, this is not the ground-state of this system, and the lattice constants and cell shape are then relaxed to obtain the ground-state.

In Fig. 6.3, the bulk band structure for the ground-state for $x = 0.75$ is shown projected onto the Bi p and Se p orbitals. It is clear that there is no band inversion (the Bi p_z orbitals are higher in energy than the Se p_z orbitals at Γ), and that the material is thus a trivial insulator. For $x = 1.0$, the material is a topological insulator.

6.3 Discussion

In summary, the ground-state properties of the alloy $(Bi_{1-x}Sb_x)_2Se_3$ were investigated as a function of the composition x. While the end-point materials are topological insulators, the intermediate concentrations $x = 0.5$, $x = 0.625$ and $x = 0.75$ were found to be trivial insulators. This suggests that there are two topological phase transitions that occur in the alloy as x is varied, the first from a topological to trivial state at a low value of x, and the second from a trivial to topological state at a large value of x. Upon projecting the bands onto different atomic orbitals, Bi and Sb were found to have weights in the same bands,

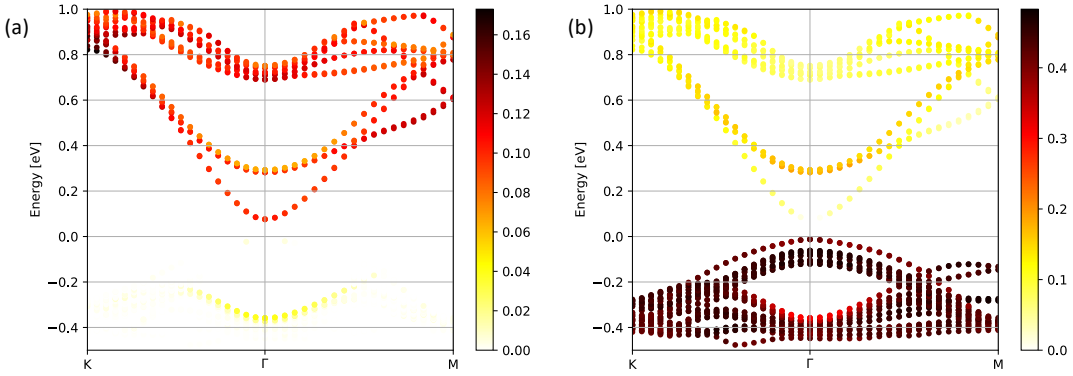

Figure 6.3. Bulk electronic structure of $(Bi_{1-x}Sb_x)_2Se_3$ at $x = 0.75$, projected onto (a) Bi p and (b) Se p orbitals, showing a trivial insulating state.

indicating that they have common-band behavior.

In the previous chapter, the topological phase transitions in the ordered Se compounds were found to occur at a critical value of the atomic spacing between QLs before subtracting the ionic radii, ~ 3.7 Å. The transitions were found to be driven by the competition of the Coulomb repulsion between the Se/Te atoms and the vdW attraction between them. While calculations are still being run for different compositions of the alloy, the values for the Se-Se spacings between QLs in Table 6.1 show that as soon as they become greater than the critical spacing, the material is driven into a trivial insulating state. This supports the conclusion from the previous chapter, and might also be useful to predict the compositions at which the transitions occur.

Also of note is the fact that the ground-state lattice constant a of the alloy, which is 4.084 Å (obtained by interpolating), is almost identical to the value of 4.083 Å obtained from using the ground-state lattice constants a of Bi_2Se_3 and Sb_2Se_3 in Vegard's law. This suggests that disorder does not strongly affect the structural properties of the alloy.

Finally, note that the alloy relaxes in a different manner from the ordered materials due to the presence of atoms of different sizes on one sublattice, which affects the ground-state lattice structure and subsequently the topological nature of these materials, and can lead to differences when compared to the optimization in the ordered materials. In ongoing work, I am investigating the compositions $x = 0.25$, $x = 0.375$ for this alloy, and also investigating the alloying of Se/Te in the chalcogenide TIs.

CHAPTER 7.

STOICHIOMETRIC AND LATTICE-MATCHED TI HETEROSTRUCTURES

Having established a framework with which to analyze topological insulators in bulk and slab geometries, we can proceed with the analysis of topological heterostructures. An interesting and open question is to determine what the effects of substrates are on topological interface states. Will there be charge transfer at the interface, and will this make the topological states move from being localized in the outermost QLs of the TI to inner QLs? Will there arise trivial interface states which are pulled towards the chemical potential μ by charge transfer? Will the properties of the topological interface states change if the surface is strongly polar? How do the various atomic layers of the materials stack with respect to each other when they are grown on top of each other? It is desirable to choose a material with a large bulk energy gap: the large gap helps screen fields well, and also means that it is harder to pull charges from the bulk to the surface. While there exist theoretical predictions pertinent to these proposed heterostructures, and people have modelled them using ab initio calculations, we have in hand a systematic and accurate methodology to study them.

The n-type semiconductor CdSe has become common for applications in nanotechnology in recent years, as its nanoparticles have been found to display quantum confinement at sizes less than 10 nm. It is a popular choice of material for the synthesis of quantum dots, which have bound states with discrete energy levels. By virtue of these properties, it has been used in Light Emitting Diodes (LEDs) and solar cells. InP is another semiconductor which is used to make quantum dots, with additional applications in solar cells, transistors and LEDs. Both materials have an energy band gap that is considered large for semiconductors, with the energy gap of CdSe being ≈ 1.8 eV and that of InP being ≈ 1.4 eV. They are both well understood materials due to their widespread utilization in electronics. Recent experiments [131, 132] have demonstrated MBE growth of lattice-matched heterostructures of TIs and large gap semiconductors. Examples of these heterostructures include $(Bi_{1-x}Sb_x)_2Se_3$/InP(111), and $Bi_2Se_3/Zn_xCd_{1-x}Se$. Tunnelling spectroscopy measurements on the former [132] have revealed the existence of topological interfacial states, and that the Fermi velocity and Dirac point energy depend on the composition parameter x. Transport measurements on the latter [131] have indicated that a single Dirac cone is intact at the Se-terminated surface of $Zn_xCd_{1-x}Se$, whereas charge transfer at the other interface destroys the topological state. Our goal is to gain an understanding of how the properties of the topological interface states are affected by the substrate (the semiconductor). InP is known to be a polar material, and we want to investigate how the use of a material with a polar surface affects the properties of the heterostructure. We consider the stoichiometric cases and run calculations on heterostructures of Bi_2Se_3/InP(111) and Bi_2Se_3/CdSe, creating interfaces between the (001) surface of Bi_2Se_3 and the other materials. We choose to study stoichiometric materials to gain an understanding of the properties of a fully ordered interface between a TI and another material.

Gaining an understanding of the properties of the topological interface states will help in predicting which materials to use in such heterojunctions. Additionally, there aren't many semiconducting materials which have large band gaps that are as closely lattice-matched

Table 7.1. Results for the structural optimization of CdSe using GGA-PBE and the van der Waals method DFT+D2. For each parameter we show the percentage difference relative to the experimental value.

	Expt.	GGA	DFT+D2
a (Å)	4.299 [133]	4.389	4.318
Devn. a	-	+2.1%	+0.43%
c (Å)	7.010 [133]	7.157	7.040
Devn. c	-	+2.1%	+0.43%
d_{int} (Å)	2.641 [133]	2.691	2.648
Devn. d_{int}	-	+1.9%	+0.27%
Gap E_g (eV)	1.85 [134]	0.42	0.53
Devn. E_g	-	-77%	-71%

with the 3D TIs we study. A large lattice mismatch implies the existence of a large strain at the interface, which will cause reconstruction in the atomic layers in the vicinity of it. This motivates us to investigate the properties of the heterostructure as well as later probe the effect of strain on the interfacial states. An interesting question would be to ask if there is a transition from a topological system to a non-topological system upon the increased application of strain, and if so, at what value of the strain. The electronic structure, spin structure and Dirac velocity of the states are analyzed. We also investigate whether the topological states remain localized close to the interface or are pulled towards the 'bulk' layers due to charge redistribution.

The bulk structural and electronic properties of InP and CdSe are first analyzed below. Upon characterizing the bulk properties, we construct slabs and study their properties, including looking for the development of strain at the surface atomic layers, redistribution of charge towards or away from the surface atomic layers, and the electronic band structure. We also study the effect of passivating the In-terminated surface of the InP slab with Hydrogen atoms, such that no bonds are left dangling at that surface. Next, different types of stacking configurations are considered to determine how the atomic layers of the semiconductor grow with respect to the atomic layers of the TI. Finally, we set up heterostructures in the preferred stacking configurations, and are in the process of obtaining and analyzing these results.

7.1 Bulk properties of InP and CdSe

CdSe is a II-VI semiconductor that is found in different crystalline forms. The hexagonal wurtzite structure is the most stable form, and its lattice constant is 3.7% larger than that of Bi_2Se_3. The difference in lattice constants is responsible for a finite strain at the interface.

InP is a III-V semiconductor, with a face-centered cubic crystal structure of the zincblende variety. Slicing the crystal along the [111] direction yields a hexagonal unit cell whose lattice constant is just 0.1% smaller than that of Bi_2Se_3. Thus, making an interface between the two materials would yield negligible strain arising from lattice mismatch. We use this unit cell for our calculations.

In Table 7.1, we present the results for the structural optimization of CdSe using GGA-

Table 7.2. Results for the structural optimization of InP using GGA-PBE and the van der Waals method DFT+D2. For each parameter we show the percentage difference relative to the experimental value.

	Expt.	GGA	DFT+D2
a (Å)	4.137 [135]	4.212	4.127
Devn. a	-	+1.8%	-0.24%
c (Å)	10.132 [135]	10.317	10.109
Devn. c	-	+1.8%	-0.24%
d_{int} (Å)	2.533 [135]	2.579	2.527
Devn. d_{int}	-	+1.8%	-0.24%
Gap E_g (eV)	1.42 [136]	0.42	0.75
Devn. E_g	-	-70%	-47%

PBE and DFT+D2. DFT+D2 yields values of the lattice parameters that are much closer to experiment than GGA. In Table 7.2, we show the results for the structural optimization of InP using GGA-PBE and DFT+D2. DFT+D2 predicts the lattice constants and interlayer distances much more accurately than GGA. The band gaps of both materials are underestimated, as is common in DFT calculations of semiconductors [91].

Figure 7.1 shows the bulk electronic structure of CdSe, calculated using PBE-GGA with DFT+D2 vdW corrections. It has a direct gap at the Γ point where the valence band is very close to the chemical potential. There is a four-fold degeneracy of the valence bands at the chemical potential.

Figure 7.2 shows the bulk electronic structure of InP, calculated using PBE-GGA with DFT+D2 vdW corrections. It also has a direct gap at the Γ point. The valence bands show six bands at very close energies at Γ, with a four and two-fold degeneracy. If we don't include SOC in the calculation, they combine to have a six-fold degeneracy at Γ [137].

7.2 Properties of InP and CdSe in slab geometries

Having characterized the structural and electronic properties of InP and CdSe in the bulk geometry, we now turn to slabs. We set up the CdSe slab using 24 atomic layers of Cd and Se each, with 80 Å of vacuum as a buffer. Six atomic layers at each surface are allowed to relax. Upon relaxation, we find that near the Se-terminated surface, the atoms reposition themselves in such a way as to slightly expand the slab along the c-axis, whereas near the Cd-terminated surface, the Cd layer moves closer to the slab. The movement at the Cd-terminated surface is of the order of 0.1 Å, whereas that near the Se-terminated surface is of the order of 0.01 Å. This indicates that there is some charge accumulation at the surfaces.

We can see that the electronic structure, shown in Figure 7.3 contains many bands crossing the chemical potential. There are a number of flat bands close to the chemical potential which suggests to us that these arise from localized charges. Additionally, there are many bands with the same shape which are shifted with respect to each other; these are bands arising from the 'bulk-like' layers, which have different energies due to charge redistribution. The number of repetitions is proportional to the number of layers in the slab.

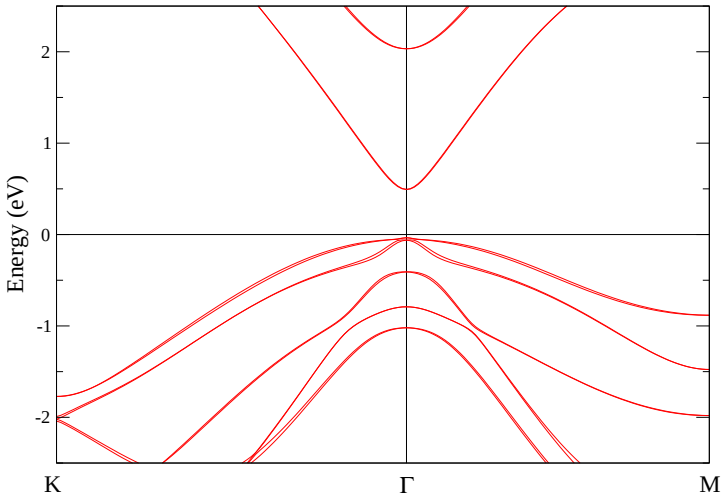

Figure 7.1. Bulk electronic structure of CdSe calculated using GGA with DFT+D2 vdW method.

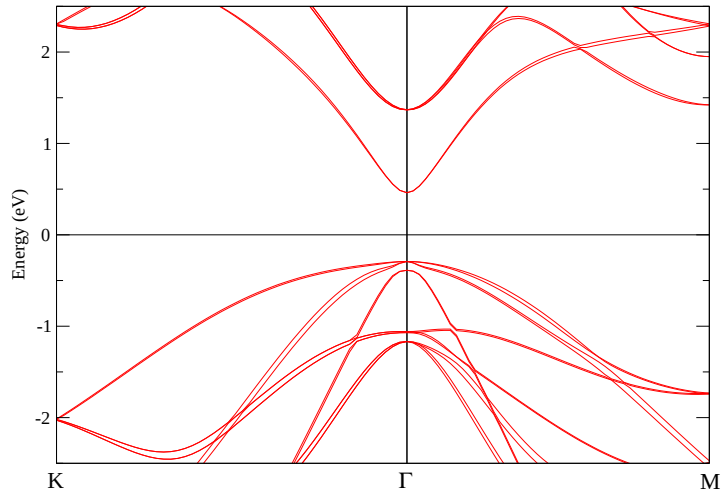

Figure 7.2. Bulk electronic structure of InP calculated using GGA with DFT+D2 vdW method.

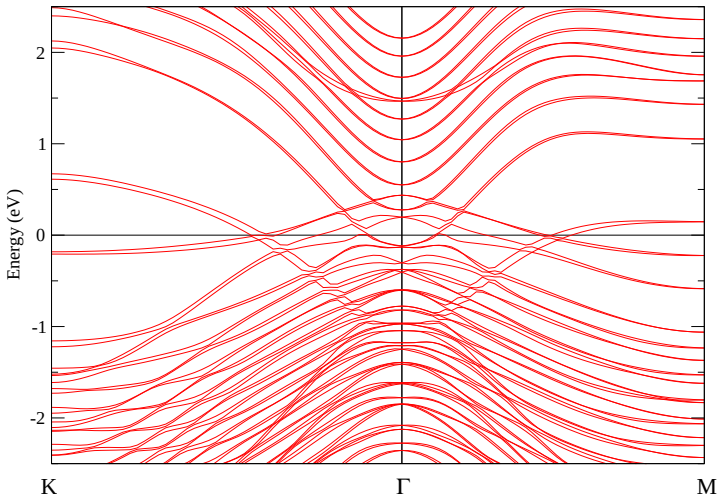

Figure 7.3. Electronic band structure of 24 atomic layer thick CdSe slab with 80 Å vacuum, calculated using GGA with DFT+D2 vdW method.

We set up the InP slab using 24 atomic layers of In and P each, with 60 Å of vacuum as a buffer. Six atomic layers at each surface are allowed to relax. Upon relaxation, we find that the atoms do not relax significantly. We can see that the band structure, shown in Figure 7.4 is quite complicated, with a lot of bands crossing the chemical potential. We notice that, similar to the case of CdSe, there are flat bands close to the chemical potential. We project the InP slab band structure onto the surface atomic layers, to look for states with a large contribution from those layers. Doing this reveals that most of the flat bands near the chemical potential arise from the surface layers. This indicates that there is considerable charge redistribution happening. To mitigate the effect of this, we try passivating one of the surfaces, in this case, the In-terminated one.

7.3 Passivation of In-terminated surface of InP slab

Passivation of a surface or molecule refers to the inclusion of pseudo-atoms of a different element, usually Hydrogen, for the purpose of providing a compensating charge density which will neutralize any dangling bonds. Passivation is usually carried out using pseudo-Hydrogen potentials. There exist different pseudo-Hydrogen potentials, named as such because they are computed assuming that they have various possible fractional numbers of electrons. The appropriate pseudo-H potential for a particular system is chosen so that it will complete the dangling bonds in a system.

It is worth reminding ourselves here that the QLs of the TIs are 'closed-shell', meaning that each atom in a QL has the exact number of electrons, hence bonds, that it requires. Thus, there was no need to passivate the TI surfaces.

In our case, to passivate the In-terminated surface, we choose the pseudo-H potential with 1.25 electrons, which provides the same number of electrons that a P atom would in bulk

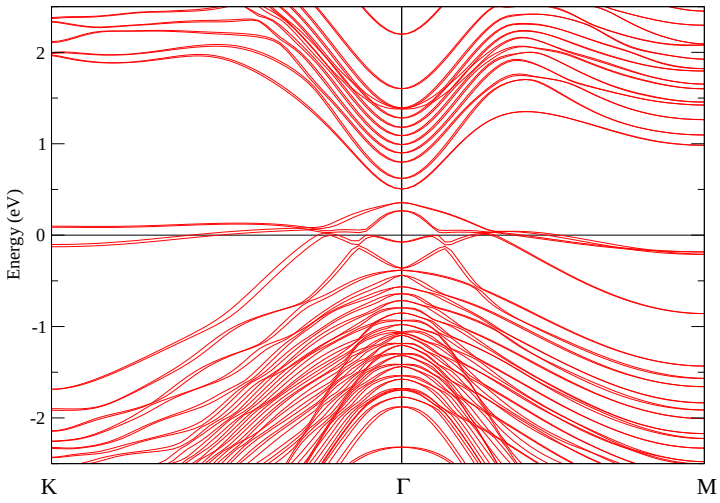

Figure 7.4. Electronic band structure of 24 atomic layer thick InP slab with 80 Å vacuum, calculated using GGA with DFT+D2 vdW method.

InP. The H atom is first relaxed so that it settles in a position which reproduces the 'bulk' chemical environment for the atoms at the passivated surface, in the sense of providing a compensating charge density that is similar to the bulk. We then treat the passivated surface as bulk, and only consider the other surface to be a true surface.

The electronic band structure for the passivated InP slab is shown below. We can see that the number of bands near the chemical potential has significantly reduced, confirming our finding that at least some of the flat bands near μ arise from the charged In surface. It is clear that the passivation, in addition to leading to the disappearance of some of the flat bands, has reduced the shifting of the 'bulk-like' bands with respect to each other, both above and below the chemical potential. This indicates that there is much less charge redistribution happening than in the unpassivated slab.

Thus, passivating the surface and calculating the slab band structure reveals that some of the flat bands crossing the chemical potential are localized at the surface, indicating that charges have been pushed there from the bulk. This is because the number of bands crossing the chemical potential has reduced, compared to the unpassivated slab. Our understanding of this is that providing atoms (in this case, by passivation) that can contribute to the charge density reduces the significant charge accumulation at the slab surfaces. This also motivates the question of what the effect of including dopant atoms which contribute more charges will be.

While we have not tried passivating the P-terminated surface of the InP slab, we imagine that it would have similar behavior, where it would result in some of the flat bands near the chemical potential not forming, and the charge redistribution would being reduced. We want to construct an interface between the TI and one of the surfaces of the semiconductor, which is why we passivate the other surface.

The next step is to investigate how the two materials stack with respect to each other.

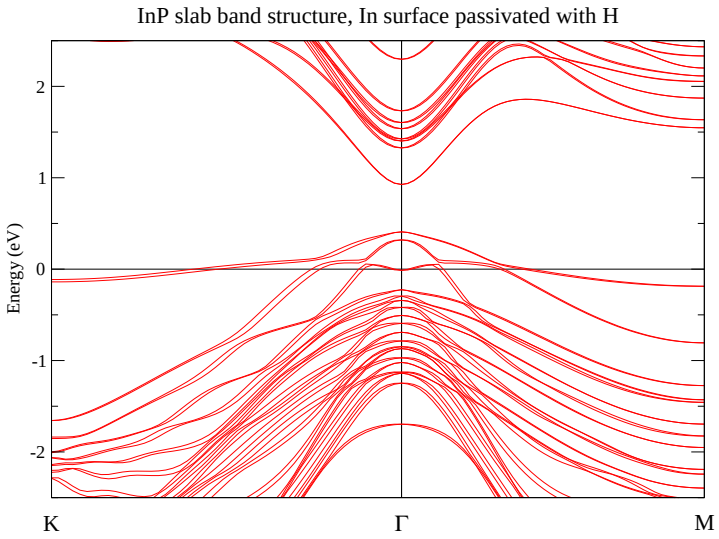

Figure 7.5. Electronic band structure of 16 atomic layer thick InP slab with 60 Å vacuum and passivated In-terminated surface, calculated using GGA with DFT+D2 vdW method.

7.4 Stacking configuration

The two materials in the heterostructure can be deposited in different configurations. For the Bi_2Se_3/InP(111) structure, we investigate the different possible stacking arrangements by simulating Se adsorption on the P-terminated surface of InP, starting at four possible positions - 'top', 'bridge', 'fcc' and 'hcp'. The positions are shown in Figure 7.6 for the various adsorption sites on the surface of InP. The unit cell of the substrate lattice is also shown (black lines). The slightly smaller lilac atoms in the lattice represent the top-most surface atomic layer, and the larger magenta atoms represent the substrate atomic layer immediately beneath the surface. The top position lies right on top of the atoms in the surface atomic layer of the substrate. The bridge position lies overhead, halfway between the atoms in the surface atomic layer of the substrate. The fcc and hcp positions are both 'holes', where there is a small hollow in the surface where an atom can fit. We use these four positions as they are the positions that respect some of the underlying crystallographic symmetries of the lattice with respect to the substrate atoms.

We relax the adsorbate atom as well as the six atomic layers of the substrate that are closest to the surface. This is done to try and mimic experimental conditions where the adsorbate atom might cause the surface atomic layers of the substrate to reconstruct.

The ground-state energies of the resultant configurations are shown in Table 7.3. We find that the top configuration has the lowest ground-state energy. This is surprising because one might expect that with the adsorbate atom not lying in a hole, it would experience the most repulsion. However, likely due to the atomic radius of Se with respect to those of P and In, the orientation of the orbitals of the adsorbate atom (Se) with respect to those of surface P atoms, as well as its valence, the top configuration is preferred. This result is in agreement with other studies [61].

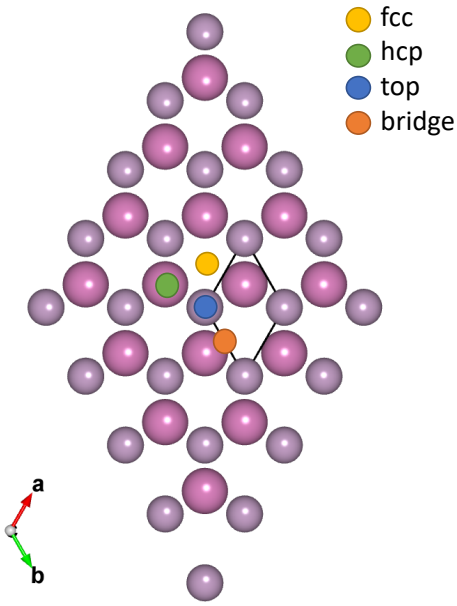

Figure 7.6. Schematic figure showing the different possible adsorption sites. The fcc, top, bridge and hcp sites are indicated, as well as the surface substrate layer (smaller atoms in the lattice) and the substrate atomic layer beneath the surface (larger atoms in the lattice).

Table 7.3. Results for the relaxation of a single Se atom on the P-terminated surface of a passivated InP slab, using the DFT+D2 method. For each configuration we show the ground-state energy and the P-Se bond length.

Site	Ground-state energy (eV)	P-Se bond length (Å)
fcc	-77.687533	2.547
hcp	-77.261900	2.533
top	-78.749785	2.153
bridge	-78.112261	2.340

Table 7.4. Results for the relaxation of a single Cd atom on the surface of a slab of Bi_2Se_3, using the DFT+D2 method. For each configuration we show the ground-state energy and the Cd-Se bond length.

Site	Ground-state energy (eV)	Cd-Se bond length (Å)
fcc	-116.95335	3.372
hcp	-116.95199	3.461
top	-116.77981	3.207
bridge	-116.90186	3.290

For the Bi_2Se_3/CdSe structure, we investigate the different possible stacking configurations by simulating Cd adsorption on the surface of Bi_2Se_3, starting at four possible positions - 'top', 'bridge', 'fcc' and 'hcp'. We relax the adsorbate atom (Cd) as well as the six atomic layers of the substrate (Bi_2Se_3) that are closest to the surface.

The ground-state energies of the resultant configurations are shown in Table 7.4. We find that the fcc and hcp stacking are both favorable when compared to the other positions. They are both very close in energy: 0.00136 eV apart, which corresponds to a very low temperature of $\approx$ 16 K, and thus both configurations must be taken into consideration when building interfaces. This will be implemented by making separate interfaces using each configuration, and comparing the ground-state energies of the two.

In these studies, I have acquired the skill of how to passivate dangling bonds at surfaces. I have also learned how to simulate the adsorption of atoms on a surface, which can be useful in predicting the configuration which a material prefers to stack in.

In summary, while the calculations on Bi_2Se_3/InP(111) and Bi_2Se_3/CdSe heterostructures are ongoing, we have found that the topological state hybridizes significantly with the trivial surface states, and we are still analyzing our results for these systems.

CHAPTER 8.

CONCLUSION AND OPEN QUESTIONS

In this dissertation, we studied, using first-principles calculations, the tuning of properties of topological insulators under various effects such as strain, alloying, and interfacing with topologically trivial materials.

In particular, we first set up a comprehensive framework to run ab initio calculations, including the van der Waals interactions, on topological insulators in bulk and surface geometries, and simultaneously obtain the correct structural and electronic properties. We next investigated the tuning of topological phase transitions under strain by varying the c/a ratio of lattice constants in the 3D topological insulator family of materials, and found that it was primarily the Coulomb repulsion competing with the van der Waals attraction that drove the transitions. The related topological phase transitions arising from disorder were next studied, in which the ground-states of the alloy $(Bi_{1-x}Sb_x)_2Se_3$ were studied for different compositions x. In ongoing work, the alloys $(Bi_{1-x}Sb_x)_2Y_3$ and $X_2(Te_ySe_{1-y})_3$ (X=Bi/Sb, Y=Te/Se) are being studied for different compositions, to gain insight into the effects of disorder and investigate topological transitions in these materials. Other ongoing work includes the study of lattice-matched heterostructures of topological insulators and topologically trivial materials. The results from this thesis can be used to make predictions on tuning the properties of novel setups involving topological insulators.

There are many interesting and open questions that remain, including investigating whether the structural optimization using various types of van der Waals corrections is affected by the different atomic sizes of the Se and Te atoms. In addition, the alloying of Se/Te is more nuanced than that of Bi/Sb, since there are two distinct sublattices on which the substitution can take place. Finally, the hybridization of the topological interfacial state in heterostructures with the trivial surface states leads to a complex band structure, and isolating the topological states will be essential to study various topological properties such as spin-momentum locking and Dirac velocity. These questions will be addressed in future studies.

APPENDIX. COPYRIGHT INFORMATION

Follow the instructions before completing and submitting the agreement. Click the "Save as Draft" button to save it and return to it later, or the "Submit" button to submit it to the journal. Please email permissions@ioppublishing.org with any questions, quoting the Article reference number.

Copyright and Publication Agreement

IOP Publishing Limited ("IOP") agrees to publish:

Manuscript Title: Importance of van der Waals interactions for ab initio studies of topological insulators (the "Article") written by

Names of all authors: Shirali, Karunya; Shelton, William; Vekhter, Ilya ("the Named Authors") in the following journal Journal of Physics: Condensed Matter ("the Journal")

If the Named Authors do NOT own the copyright in the Article, please write the full name of the organization/institution/company which owns the copyright here (see instructions here).

THIS BOX SHOULD BE LEFT BLANK IF THE NAMED AUTHORS OWN THE COPYRIGHT

(the "Copyright Owner")

IOP Ref: JPCM-117120.R1

Part 1: Publication on a Subscription Basis

1 In consideration for acceptance and publication of the Article, the Named Authors and/or the Copyright Owner assign, where necessary by present assignment of future copyright, to IOP with full title guarantee the entire copyright in all original material published as part of the Article (which expression includes but is not limited to the text, abstract, tables, figures and graphs, related corrigenda or "comments" and multimedia content but excludes any other item referred to as supplementary material and/or any video abstract) throughout the world for the full term of copyright (including any extensions or renewals thereof) for all media and formats, whether known or unknown. Such assignment shall be effective only if the Article (or any resubmission of the Article) is accepted for publication. For the avoidance of doubt, copyright does not subsist in any fundamental data underlying the Article and nothing in this agreement is intended to limit access to or use of such data.

2 The Named Authors' rights.

2.1 IOP grants the Named Authors the rights specified in https://publishingsupport.iopscience.iop.org/author-rights-policies/.

2.2 In summary, the Named Authors may only include the Final Published Version of the Article in certain prescribed circumstances. The Accepted Manuscript of the Article may be included in more instances, provided in all cases use is in accordance with the Author Rights set out at https://publishingsupport.iopscience.iop.org/author-rights-policies/ on the date of submission of the agreement.

Part 2: Publication on a Gold Open Access Basis

1.1 In consideration for acceptance and publication of the Article, the Named Authors of the Article and/or the Copyright Owner grant IOP a royalty-free, non-exclusive, freely transferrable, worldwide, perpetual licence for the full term of copyright (including any extensions or renewals) for all media and formats, whether known or unknown, to do in relation to the Article (which expression includes the text, abstract, tables, figures and graphs, related corrigenda or "comments" and multimedia content but excludes any other item referred to as supplementary material and/or any video abstract) all acts restricted by copyright worldwide. Such licence shall be effective only if the Article (or any resubmission of it) is accepted for publication. Copyright does not subsist in any fundamental data underlying the Article and nothing in the agreement is intended to limit access to or use of such data.

1.2 Each of the Named Authors and, where relevant, the Copyright Owner consents to the publication of the Article under the Creative Commons Attribution 4.0 International licence (CC BY 4.0) or any successor to that licence.

Part 3: General (Applicable to both Subscription and Gold Open Access Articles)

1.1 If the Article, or any part of it, is protected by Crown copyright, in consideration for acceptance and publication of the Article, the relevant Named Authors and/or the originating department or agency grant IOP a non-exclusive royalty-free worldwide freely-transferrable perpetual licence for the full term of copyright (including any extensions or renewals) for all media and formats, whether known or unknown, to do in relation to the Article all acts restricted by copyright worldwide including the right of action under section 101A of the Copyright Designs and Patents Act 1988.

1.2 If any of the Named Authors are employees of the US Government, please refer to the US Government policy.

1.3 In consideration for acceptance and publication of the Article, the Named Authors and/or the Copyright Owner grant IOP a royalty-free non-exclusive worldwide freely transferrable worldwide perpetual licence for the full term of copyright (including any extensions or renewals) for all media and formats, whether known or unknown, to do in relation to any supplementary material not deemed to be part of the Article, and/or any video abstract, all acts restricted by copyright worldwide. This shall include making the material available under any licence that IOP deems appropriate for purposes including the maximisation of visibility and the long-term preservation of the content.

1.4 IOP shall process and publish the personal data of each Named Author, as that data is displayed on the Article, including the names and affiliations of the Named Authors and the email address of the Submitting Author, wherever IOP chooses to display it, whether themselves or via a third party, to provide a lasting record of publication and for archiving purposes in the public interest. IOP will process the personal data of Named Authors in accordance with its privacy policy, the current version of which can be accessed via its website.

Representations and warranties

2.1 The Copyright Owner and/or the Submitting Author and/or the US Government Signatory on behalf of the Named Authors and/or the US Government (as appropriate) represent and warrant that with regard to the Article:

2.1.1 it is the original work of the Named Authors;

2.1.2 it has not been published previously in any form, other than in accordance with IOP's Preprint pre-publication policy;

2.1.3 each of the Named Authors has made a material contribution to its conception and/or writing, has received the final version, has agreed to its submission on these terms and takes responsibility

for it and submission has been approved as necessary by the authorities at the establishment where the research was carried out;

2.1.4 the Submitting Author completes and returns this agreement as authorised agent for and on behalf of all the Named Authors and the Copyright Owner (as applicable) and has the full power to enter into it and to make the grants and assignments and/or licences it contains;

2.1.5 the US Government Signatory (where applicable) completes and returns this agreement for and on behalf of the US Government and all the Named Authors who are employees of the US Government and has the full power to enter into this agreement and to make the grants it contains;

2.1.6 it has not been and shall not be submitted to another publisher prior to withdrawal or rejection by IOP;

2.1.7 it does not infringe any third party rights, contains nothing libelous or unlawful, all factual statements are to the best of the Named Authors' knowledge and belief true or based on valid research conducted according to accepted norms and all required permissions have been obtained in writing;

2.1.8 it expressly acknowledges any third-party funding and/or potential conflicts of interest; and

2.1.9 any supplementary material or video abstract is the original work of the Named Authors, or the property of the Copyright Owner, or permission has been obtained from its owner(s) for its publication by IOP and permission has been obtained for the inclusion of any third-party content.

2.2 The Named Authors and/or the Copyright Owner (as appropriate) indemnify and shall keep indemnified IOP against all costs and expenses suffered or incurred by IOP as a result of and/or arising out of any breach of the representations and/or warranties in this section 2.

Miscellaneous

3.1 To the extent that there are moral rights in the Article, all the Named Authors expressly reserve and assert their moral rights to be identified as the authors.

3.2 The Named Authors and/or the Copyright Owner and/or the US Government Signatory on behalf of the US Government shall execute such further documents, and take such actions and do such things, as may be requested by IOP at IOP's reasonable expense to give full effect to the terms of the agreement.

3.3 The grants and assignment or licence in this agreement shall become effective only upon acceptance of the Article for publication. If the Article is withdrawn prior to acceptance, or is rejected, this agreement shall have no effect and no party shall be bound by it.

Confirmation

4.1 By selecting to publish on a subscription basis, the Submitting Author shall ensure that, where relevant, all Named Authors who are affiliated to a university/institution which has an open access policy incompatible with IOP's green open access policy, obtain a waiver for the Article from that open access policy and retain it as evidence of compliance. These Named Authors shall obtain such waivers and provide them to IOP promptly on request. By selecting to publish Gold Open Access, the Submitting Author is responsible for ensuring that the Article Publication Charge of the Journal is paid in full to IOP, pursuant to IOP's payment terms, unless otherwise agreed in writing with IOP.

4.2 By typing the Submitting Author's name into the box at Part 3 below and clicking "Submit", the Named Authors agree to the terms. Where the Article was created as part of a work for hire and/or as part of a Named Author(s)' employment, the Authorised signatories of any third party Copyright Owner(s) and/or the Submitting Author agree, on behalf of such Copyright Owner(s), to these terms by typing the Copyright Owner's name into the "Copyright Owner" box at the top of the page.

Part 4: Confirmation and Execution

Please tick the appropriate boxes in section A, section B and section C below. For help on this section, click here.

req **Section A**

Please tick one of the boxes below to confirm how you would like the Article published (if it is accepted):

Subscription – Parts 1 and 3 Apply

req **Section B**

Please tick one of the boxes below to confirm your choice. For help on this section, click here.

For Subscription - Please tick this box to confirm that each Named Author, who is affiliated to a university/institution which has an open access policy incompatible with IOP's green open access policy, has obtained a waiver for the Article from that open access policy. For more information refer to this page.

req **Section C**

Please ALSO tick one of the boxes below to confirm the basis upon which you are granting IOP the right to publish the article (if it is accepted). For help on this section, click here.

Standard transfer of copyright (assignment) – please select this box for subscription articles unless one of the exceptions below applies.

req Type your name here:

Karunya Shirali (The "Submitting Author")

req Date:

24-Sep-2020

By clicking "Submit" and typing your name above, you shall be assumed to have read and understood all of the terms and conditions of the relevant part of this agreement and you will be agreeing to all of the terms and conditions and assignment (as the case may be) detailed above.

LAST UPDATED October 2019

WORKS CITED

[1] M. Z. Hasan and C. L. Kane. Colloquium: Topological insulators. *Reviews of Modern Physics*, 82(4):3045–3067, nov 2010.

[2] C. L. Kane and E. J. Mele. Z2 topological order and the quantum spin hall effect. *Physical Review Letters*, 95(14):146802, sep 2005.

[3] C. L. Kane and E. J. Mele. Quantum Spin hall effect in graphene. *Physical Review Letters*, 95(22):226801, nov 2005.

[4] B Andrei Bernevig, Taylor L Hughes, and Shou-Cheng Zhang. Quantum spin hall effect and topological phase transition in hgte quantum wells. *Science*, 314(5806):1757–1761, 2006.

[5] Liang Fu, C. L. Kane, and E. J. Mele. Topological insulators in three dimensions. *Physical Review Letters*, 98(10):106803, mar 2007.

[6] Liang Fu and C. L. Kane. Topological insulators with inversion symmetry. *Physical Review B - Condensed Matter and Materials Physics*, 76(4):045302, jul 2007.

[7] Rahul Roy. Topological phases and the quantum spin Hall effect in three dimensions. *Physical Review B - Condensed Matter and Materials Physics*, 79(19):195322, may 2009.

[8] Haijun Zhang, Chao-Xing Liu, Xiao-Liang Qi, Xi Dai, Zhong Fang, and Shou-Cheng Zhang. Topological insulators in Bi2Se3, Bi2Te3 and Sb2Te3 with a single Dirac cone on the surface. *Nature Physics*, 5(6):438–442, jun 2009.

[9] Markus König, Steffen Wiedmann, Christoph Brüne, Andreas Roth, Hartmut Buhmann, Laurens W. Molenkamp, Xiao Liang Qi, and Shou Cheng Zhang. Quantum spin hall insulator state in HgTe quantum wells. *Science*, 318(5851):766–770, nov 2007.

[10] Y. Xia, D. Qian, D. Hsieh, L. Wray, A. Pal, H. Lin, A. Bansil, D. Grauer, Y. S. Hor, R. J. Cava, and M. Z. Hasan. Observation of a large-gap topological-insulator class with a single Dirac cone on the surface. *Nature Physics*, 5(6):398–402, may 2009.

[11] D. Hsieh, D. Qian, L. Wray, Y. Xia, Y. S. Hor, R. J. Cava, and M. Z. Hasan. A topological Dirac insulator in a quantum spin Hall phase. *Nature 2008 452:7190*, 452(7190):970–974, apr 2008.

[12] Y. L. Chen, J. G. Analytis, J. H. Chu, Z. K. Liu, S. K. Mo, X. L. Qi, H. J. Zhang, P. H. Lu, X. Dai, Z. Fang, S. C. Zhang, I. R. Fisher, Z. Hussain, and Z. X. Shen. Experimental realization of a three-dimensional topological insulator, Bi2Te3. *Science*, 325(5937):178–181, jul 2009.

[13] D. Hsieh, Y. Xia, D. Qian, L. Wray, J. H. Dil, F. Meier, J. Osterwalder, L. Patthey, J. G. Checkelsky, N. P. Ong, A. V. Fedorov, H. Lin, A. Bansil, D. Grauer, Y. S. Hor, R. J. Cava, and M. Z. Hasan. A tunable topological insulator in the spin helical Dirac transport regime. *Nature*, 460(7259):1101–1105, aug 2009.

[14] D. Hsieh, Y. Xia, D. Qian, L. Wray, F. Meier, J. H. Dil, J. Osterwalder, L. Patthey, A. V. Fedorov, H. Lin, A. Bansil, D. Grauer, Y. S. Hor, R. J. Cava, and M. Z. Hasan. Observation of time-reversal-protected single-dirac-cone topological-insulator states in Bi2Te3 and Sb2Te3. *Physical Review Letters*, 103(14):146401, sep 2009.

[15] Chang Liu, Yongchao Wang, Hao Li, Yang Wu, Yaoxin Li, Jiaheng Li, Ke He, Yong Xu, Jinsong Zhang, and Yayu Wang. Robust axion insulator and Chern insulator phases in a two-dimensional antiferromagnetic topological insulator. *Nature Materials 2020 19:5*, 19(5):522–527, jan 2020.

[16] Yosuke Satake, Junichi Shiogai, Daichi Takane, Keiko Yamada, Kohei Fujiwara, Seigo Souma, Takafumi Sato, Takashi Takahashi, and Atsushi Tsukazaki. Fermi-level tuning of the dirac surface state in $(\mathrm{bi}_{1-x}\mathrm{sb}_x)_2\mathrm{se}_3$ thin films. *Journal of Physics: Condensed Matter*, 30(8):085501, feb 2018.

[17] Y. Liu, Y. Y. Li, S. Rajput, D. Gilks, L. Lari, P. L. Galindo, M. Weinert, V. K. Lazarov, and L. Li. Tuning Dirac states by strain in the topological insulator Bi2Se3. *Nature Physics 2014 10:4*, 10(4):294–299, mar 2014.

[18] Ilija Zeljkovic, Daniel Walkup, Badih A. Assaf, Kane L. Scipioni, R. Sankar, Fangcheng Chou, and Vidya Madhavan. Strain engineering Dirac surface states in heteroepitaxial topological crystalline insulator thin films. *Nat. Nanotechnol.*, 10(10):849–853, aug 2015.

[19] David Flötotto, Yang Bai, Yang Hao Chan, Peng Chen, Xiaoxiong Wang, Paul Rossi, Cai Zhi Xu, Can Zhang, Joseph A. Hlevyack, Jonathan D. Denlinger, Hawoong Hong, Mei Yin Chou, Eric J. Mittemeijer, James N. Eckstein, and Tai Chang Chiang. In Situ Strain Tuning of the Dirac Surface States in Bi2Se3 Films. *Nano Letters*, 18(9):5628–5632, sep 2018.

[20] Won Jun Yang, Chang Woo Lee, Da Sol Kim, Hyun Sik Kim, Jong Hyeon Kim, Hwan Young Choi, Young Jai Choi, Jae Hoon Kim, Kyungwha Park, and Mann Ho Cho. Tuning of Topological Dirac States via Modification of van der Waals Gap in Strained Ultrathin Bi2Se3 Films. *Journal of Physical Chemistry C*, 122(41):23739–23748, oct 2018.

[21] Jinsong Zhang, Cui Zu Chang, Zuocheng Zhang, Jing Wen, Xiao Feng, Kang Li, Minhao Liu, Ke He, Lili Wang, Xi Chen, Qi Kun Xue, Xucun Ma, and Yayu Wang. Band structure engineering in (Bi1?xSbx)2Te3 ternary topological insulators. *Nature Communications 2011 2:1*, 2(1):1–6, dec 2011.

[22] Desheng Kong, Yulin Chen, Judy J. Cha, Qianfan Zhang, James G. Analytis, Keji Lai, Zhongkai Liu, Seung Sae Hong, Kristie J. Koski, Sung Kwan Mo, Zahid Hussain, Ian R.

Fisher, Zhi Xun Shen, and Yi Cui. Ambipolar field effect in the ternary topological insulator (BixSb1?x)2Te3 by composition tuning. *Nature Nanotechnology 2011 6:11*, 6(11):705–709, oct 2011.

[23] Wonhee Ko, Insu Jeon, Hyo Won Kim, Hyeokshin Kwon, Se Jong Kahng, Joonbum Park, Jun Sung Kim, Sung Woo Hwang, and Hwansoo Suh. Atomic and electronic structure of an alloyed topological insulator, Bi1.5Sb0.5Te1.7Se1.3. *Scientific Reports 2013 3:1*, 3(1):1–5, sep 2013.

[24] K. W. Post, Y. S. Lee, B. C. Chapler, A. A. Schafgans, Mario Novak, A. A. Taskin, Kouji Segawa, M. D. Goldflam, H. T. Stinson, Yoichi Ando, and D. N. Basov. Infrared probe of the bulk insulating response in Bi2-x Sbx Te3-y Sey topological insulator alloys. *Physical Review B - Condensed Matter and Materials Physics*, 91(16):165202, apr 2015.

[25] Y. Tung, Y. F. Chiang, C. W. Chong, Z. X. Deng, Y. C. Chen, J. C.A. Huang, C. M. Cheng, T. W. Pi, K. D. Tsuei, Z. Li, and H. Qiu. Growth and characterization of molecular beam epitaxy-grown Bi2Te3?xSex topological insulator alloys. *Journal of Applied Physics*, 119(5):055303, feb 2016.

[26] Hyoungdo Nam, Yang Xu, Ireneusz Miotkowski, Jifa Tian, Yong P. Chen, Chang Liu, M. Zahid Hasan, Wenguang Zhu, Gregory A. Fiete, and Chih Kang Shih. Microscopic investigation of Bi2-xSbxTe3-ySey systems: On the origin of a robust intrinsic topological insulator. *Journal of Physics and Chemistry of Solids*, 128:251–257, may 2019.

[27] Jianpeng Liu and David Vanderbilt. Topological phase transitions in (Bi1-xInx) 2Se3 and (Bi1-xSbx) 2Se3. *Physical Review B - Condensed Matter and Materials Physics*, 88(22):224202, dec 2013.

[28] M. Z. Hasan and C. L. Kane. Colloquium : Topological insulators. *Reviews of Modern Physics*, 82(4):3045–3067, nov 2010.

[29] Xiao-Liang Qi and Shou-Cheng Zhang. Topological insulators and superconductors. *Reviews of Modern Physics*, 83(4):1057–1110, oct 2011.

[30] Fan Zhang, C. L. Kane, and E. J. Mele. Surface states of topological insulators. *Phys. Rev. B*, 86:081303(R), Aug 2012.

[31] M. M. Asmar, D. E. Sheehy, and I. Vekhter. Interface symmetry and spin control in topological-insulator–semiconductor heterostructures. *Phys. Rev. B*, 95:241115(R), 2017.

[32] Y. Xia, D. Qian, D. Hsieh, R. Shankar, H. Lin, A. Bansil, A. V. Fedorov, D. Grauer, Y. S. Hor, R. J. Cava, and M. Z. Hasan. Topological Control: Systematic control of topological insulator Dirac fermion density on the surface of Bi2Te3, jul 2009.

[33] Y. Xia, L. Wray, D. Qian, D. Hsieh, A. Pal, H. Lin, A. Bansil, D. Grauer, Y. S. Hor, R. J. Cava, and M. Z. Hasan. Electrons on the surface of Bi2Se3 form a topologically-ordered two dimensional gas with a non-trivial Berry's phase, dec 2008.

[34] L. Andrew Wray, Su Yang Xu, Yuqi Xia, Yew San Hor, Dong Qian, Alexei V. Fedorov, Hsin Lin, Arun Bansil, Robert J. Cava, and M. Zahid Hasan. Observation of topological order in a superconducting doped topological insulator. *Nature Physics 2010 6:11*, 6(11):855–859, sep 2010.

[35] Felix Bloch. Über die Quantenmechanik der Elektronen in Kristallgittern. *Zeitschrift für Physik 1929 52:7*, 52(7):555–600, jul 1929.

[36] Michael Victor Berry. Quantal phase factors accompanying adiabatic changes. *Proceedings of the Royal Society of London. A. Mathematical and Physical Sciences*, 392(1802):45–57, 1984.

[37] Hanna Lind, Sven Lidin, and Ulrich Häussermann. Structure and bonding properties of (Bi 2 Se 3) m (Bi 2) n stacks by first-principles density functional theory. *Physical Review B*, 72(18):184101, nov 2005.

[38] Chao Xing Liu, Xiao Liang Qi, Haijun Zhang, Xi Dai, Zhong Fang, and Shou Cheng Zhang. Model Hamiltonian for topological insulators. *Physical Review B - Condensed Matter and Materials Physics*, 82(4):045122, jul 2010.

[39] W. Kohn and L. J. Sham. Self-consistent equations including exchange and correlation effects. *Phys. Rev.*, 140:A1133–A1138, Nov 1965.

[40] P. Hohenberg and W. Kohn. Inhomogeneous electron gas. *Phys. Rev.*, 136:B864–B871, Nov 1964.

[41] Stefan Grimme. Semiempirical GGA-type density functional constructed with a long-range dispersion correction. *Journal of Computational Chemistry*, 27(15):1787–1799, nov 2006.

[42] Stefan Grimme, Jens Antony, Stephan Ehrlich, and Helge Krieg. A consistent and accurate ab initio parametrization of density functional dispersion correction (DFT-D) for the 94 elements H-Pu. *The Journal of Chemical Physics*, 132(15):154104, apr 2010.

[43] Alexandre Tkatchenko and Matthias Scheffler. Accurate molecular van der waals interactions from ground-state electron density and free-atom reference data. *Phys. Rev. Lett.*, 102:073005, Feb 2009.

[44] Tomáš Bučko, S. Lebègue, Jürgen Hafner, and J. G. Ángyán. Tkatchenko-scheffler van der waals correction method with and without self-consistent screening applied to solids. *Phys. Rev. B*, 87:064110, Feb 2013.

[45] Alexandre Tkatchenko, Robert A. DiStasio, Roberto Car, and Matthias Scheffler. Accurate and efficient method for many-body van der waals interactions. *Phys. Rev. Lett.*, 108:236402, Jun 2012.

[46] Alberto Ambrosetti, Anthony M. Reilly, Robert A. Distasio, and Alexandre Tkatchenko. Long-range correlation energy calculated from coupled atomic response functions. *Journal of Chemical Physics*, 140(18), may 2014.

[47] Jianwei Sun, Adrienn Ruzsinszky, and John P. Perdew. Strongly constrained and appropriately normed semilocal density functional. *Phys. Rev. Lett.*, 115:036402, Jul 2015.

[48] Haowei Peng, Zeng-Hui Yang, John P. Perdew, and Jianwei Sun. Versatile van der waals density functional based on a meta-generalized gradient approximation. *Phys. Rev. X*, 6:041005, Oct 2016.

[49] Kyuho Lee, Éamonn D. Murray, Lingzhu Kong, Bengt I. Lundqvist, and David C. Langreth. Higher-accuracy van der waals density functional. *Phys. Rev. B*, 82:081101(R), Aug 2010.

[50] Karunya Shirali, William A Shelton, and Ilya Vekhter. Importance of van der Waals interactions for ab initio studies of topological insulators. *Journal of Physics: Condensed Matter*, 33(3):035702, oct 2020.

[51] Cui-Zu Chang, Peizhe Tang, Xiao Feng, Kang Li, Xu-Cun Ma, Wenhui Duan, Ke He, and Qi-Kun Xue. Band Engineering of Dirac Surface States in Topological-Insulator-Based van der Waals Heterostructures. *Physical Review Letters*, 115(13):136801, sep 2015.

[52] Oleg V. Yazyev, Joel E. Moore, and Steven G. Louie. Spin polarization and transport of surface states in the topological insulators bi_2se_3 and bi_2te_3 from first principles. *Phys. Rev. Lett.*, 105:266806, Dec 2010.

[53] Oleg V. Yazyev, Emmanouil Kioupakis, Joel E. Moore, and Steven G. Louie. Quasiparticle effects in the bulk and surface-state bands of bi_2se_3 and bi_2te_3 topological insulators. *Phys. Rev. B*, 85:161101(R), Apr 2012.

[54] Jason M. Crowley, Jamil Tahir-Kheli, and William A. Goddard. Accurate Ab Initio Quantum Mechanics Simulations of Bi ₂ Se ₃ and Bi ₂ Te ₃ Topological Insulator Surfaces. *The Journal of Physical Chemistry Letters*, 6(19):3792–3796, oct 2015.

[55] Jifeng Sun and David J. Singh. Using gapped topological surface states of bi2se3 films in a field effect transistor. *Journal of Applied Physics*, 121(6):064301, 2017.

[56] Matteo Michiardi, Irene Aguilera, Marco Bianchi, Vagner Eustáquio de Carvalho, Luiz Orlando Ladeira, Nayara Gomes Teixeira, Edmar Avellar Soares, Christoph Friedrich, Stefan Blügel, and Philip Hofmann. Bulk band structure of Bi 2 Te 3. *Physical Review B*, 90(7):075105, aug 2014.

[57] S. J. Youn and A. J. Freeman. First-principles electronic structure and its relation to thermoelectric properties of bi_2te_3. *Phys. Rev. B*, 63:085112, Feb 2001.

[58] Hua Chen, Wenguang Zhu, Di Xiao, and Zhenyu Zhang. CO oxidation facilitated by robust surface states on Au-covered topological insulators. *Physical Review Letters*, 107(5):056804, jul 2011.

[59] I. A. Nechaev, R. C. Hatch, M. Bianchi, D. Guan, C. Friedrich, I. Aguilera, J. L. Mi, B. B. Iversen, S. Blügel, Ph. Hofmann, and E. V. Chulkov. Evidence for a direct band gap in the topological insulator bi_2se_3 from theory and experiment. *Phys. Rev. B*, 87:121111(R), Mar 2013.

[60] Irene Aguilera, Christoph Friedrich, Gustav Bihlmayer, and Stefan Blügel. G W study of topological insulators Bi 2 Se 3 , Bi 2 Te 3 , and Sb 2 Te 3 : Beyond the perturbative one-shot approach. *Physical Review B*, 88(4):045206, jul 2013.

[61] Hyungjun Lee and Oleg V. Yazyev. Lattice-matched heterojunctions between topological and normal insulators: A first-principles study. *Phys. Rev. B*, 95:085304, Feb 2017.

[62] Jia Zhang, Julian P. Velev, Xiaoqian Dang, and Evgeny Y. Tsymbal. Band structure and spin texture of $bi_2se_3 3d$ ferromagnetic metal interface. *Phys. Rev. B*, 94:014435, Jul 2016.

[63] Xin Luo, Michael B. Sullivan, and Su Ying Quek. First-principles investigations of the atomic, electronic, and thermoelectric properties of equilibrium and strained Bi 2 Se 3 and Bi 2 Te 3 including van der Waals interactions. *Physical Review B*, 86(18):184111, nov 2012.

[64] L. Cheng, H. J. Liu, J. Zhang, J. Wei, J. H. Liang, J. Shi, and X. F. Tang. Effects of van der waals interactions and quasiparticle corrections on the electronic and transport properties of bi_2te_3. *Phys. Rev. B*, 90:085118, Aug 2014.

[65] T. Björkman, A. Gulans, A. V. Krasheninnikov, and R. M. Nieminen. van der waals bonding in layered compounds from advanced density-functional first-principles calculations. *Phys. Rev. Lett.*, 108:235502, Jun 2012.

[66] Thomas K. Reid, S. Pamir Alpay, Alexander V. Balatsky, and Sanjeev K. Nayak. First-principles modeling of binary layered topological insulators: Structural optimization and exchange-correlation functionals. *Phys. Rev. B*, 101:085140, Feb 2020.

[67] Y. N. Zhang. Communication: Surface stability and topological surface states of cleaved bi2se3: First-principles studies. *The Journal of Chemical Physics*, 143(15):151101, 2015.

[68] K. Govaerts, K. Park, C. De Beule, B. Partoens, and D. Lamoen. Effect of Bi bilayers on the topological states of Bi 2 Se 3 : A first-principles study. *Physical Review B*, 90(15):155124, oct 2014.

[69] Wenliang Liu, Xiangyang Peng, Xiaolin Wei, Hong Yang, G. Malcolm Stocks, and Jianxin Zhong. Surface and substrate induced effects on thin films of the topological insulators Bi2Se3 and Bi2Te3. *Physical Review B - Condensed Matter and Materials Physics*, 87(20):205315, may 2013.

[70] H. Aramberri and M. C. Muñoz. Strain effects in topological insulators: Topological order and the emergence of switchable topological interface states in Sb2 Te3/ Bi2 Te3 heterojunctions. *Physical Review B*, 95(20):205422, may 2017.

[71] Guohua Cao, Huijun Liu, Jinghua Liang, Long Cheng, Dengdong Fan, and Zhenyu Zhang. Rhombohedral Sb_2Se_3 as an intrinsic topological insulator due to strong van der waals interlayer coupling. *Phys. Rev. B*, 97:075147, Feb 2018.

[72] G. Kresse and J. Hafner. Ab initio molecular dynamics for liquid metals. *Phys. Rev. B*, 47:558(R), 1993.

[73] G. Kresse and J. Hafner. Ab initio molecular-dynamics simulation of the liquid-metal-amorphous-semiconductor transition in germanium. *Phys. Rev. B*, 49:14251, 1994.

[74] G. Kresse and J. Furthmüller. Efficiency of ab-initio total energy calculations for metals and semiconductors using a plane-wave basis set. *Comput. Mat. Sci.*, 6:15, 1996.

[75] G. Kresse and J. Furthmüller. Efficient iterative schemes for ab initio total-energy calculations using a plane-wave basis set. *Phys. Rev. B*, 54:11169, 1996.

[76] Seizo Nakajima. The crystal structure of $\mathrm{bi_2te_{3-x}se_x}$. *Journal of Physics and Chemistry of Solids*, 24(3):479–485, 1963.

[77] Andrius Merkys, Antanas Vaitkus, Justas Butkus, Mykolas Okulič-Kazarinas, Visvaldas Kairys, and Saulius Gražulis. *COD::CIF::Parser*: an error-correcting CIF parser for the Perl language. *J. Appl. Cryst.*, 49(1), Feb 2016.

[78] Saulius Gražulis, Andrius Merkys, Antanas Vaitkus, and Mykolas Okulič-Kazarinas. Computing stoichiometric molecular composition from crystal structures. *Journal of Applied Crystallography*, 48(1):85–91, Feb 2015.

[79] Saulius Gražulis, A. Daškevič, Andrius Merkys, D. Chateigner, L. Lutterotti, M. Quirós, N. R. Serebryanaya, P. Moeck, R. T. Downs, and A. Le Bail. Crystallography open database (cod): an open-access collection of crystal structures and platform for world-wide collaboration. *Nucleic Acids Research*, 40:D420–D427, 2012.

[80] Saulius Gražulis, Daniel Chateigner, Robert T. Downs, A. F.T. Yokochi, Miguel Quirós, Luca Lutterotti, Elena Manakova, Justas Butkus, Peter Moeck, and Armel Le Bail. Crystallography Open Database – an open-access collection of crystal structures. *Journal of Applied Crystallography*, 42(Pt 4):726, 2009.

[81] R. T. Downs and M. Hall-Wallace. The american mineralogist crystal structure database. *American Mineralogist*, 88:247–250, 2003.

[82] SA Semiletov and ZG Pinsker. The electron diffraction analysis of the system of alloys Bi-Se. *Dokl. AN SSSR*, 100:1079–1082, 1955.

[83] RWG Wyckoff. Structures of complex binary compounds RnXm. *Crystal Structures; J. Wiley and Sons: New York, NY, USA*, 2, 1964.

[84] P. E. Blochl. Projector augmented-wave method. *Phys. Rev. B*, 50:17953, 1994.

[85] G. Kresse and D. Joubert. From ultrasoft pseudopotentials to the projector augmented-wave method. *Phys. Rev. B*, 59:1758, 1999.

[86] V. Wang. Vaspkit — postprocessing tool for vasp code, 2013.

[87] J. P. Perdew, K. Burke, and M. Ernzerhof. Generalized gradient approximation made simple. *Phys. Rev. Lett.*, 77:3865, 1996.

[88] J. P. Perdew, K. Burke, and M. Ernzerhof. Erratum: Generalized gradient approximation made simple. *Phys. Rev. Lett.*, 78:1396, 1997.

[89] J. P. Perdew and A. Zunger. Self-interaction correction to density-functional approximations for many-electron systems. *Phys. Rev. B*, 23:5048, 1981.

[90] Abdullahi Lawal, A. Shaari, R. Ahmed, and Norshila Jarkoni. First-principles investigations of electron-hole inclusion effects on optoelectronic properties of Bi2Te3, a topological insulator for broadband photodetector. *Physica B: Condensed Matter*, 520:69–75, sep 2017.

[91] John P. Perdew. Density functional theory and the band gap problem. *International Journal of Quantum Chemistry*, 28(S19):497–523, 1985.

[92] M. K. Y. Chan and G. Ceder. Efficient band gap prediction for solids. *Phys. Rev. Lett.*, 105:196403, Nov 2010.

[93] C. Lamuta, D. Campi, A. Cupolillo, Z. S. Aliev, M. B. Babanly, E. V. Chulkov, A. Politano, and L. Pagnotta. Mechanical properties of Bi2Te3 topological insulator investigated by density functional theory and nanoindentation. *Scripta Materialia*, 121:50–55, aug 2016.

[94] The Elk Code. `http://elk.sourceforge.net/`.

[95] I. G. Austin. The optical properties of bismuth telluride. *Proceedings of the Physical Society*, 72(4):545–552, 1958.

[96] Miyoung Kim, A. J. Freeman, and Clint B. Geller. Screened exchange lda determination of the ground and excited state properties of thermoelectrics: bi_2te_3. *Phys. Rev. B*, 72:035205, Jul 2005.

[97] J Betancourt, S Li, X Dang, J D Burton, E Y Tsymbal, and J P Velev. Complex band structure of topological insulator bi2se3. *Journal of Physics: Condensed Matter*, 28(39):395501, aug 2016.

[98] Takehiro Kato, Hiroki Kotaka, and Fumiyuki Ishii. First-principles study of surface states in topological insulators bi2te3 and bi2se3: film thickness dependence. *Molecular Simulation*, 41(10-12):892–895, 2015.

[99] James G. Analytis, Jiun Haw Chu, Yulin Chen, Felipe Corredor, Ross D. McDonald, Z. X. Shen, and Ian R. Fisher. Bulk Fermi surface coexistence with Dirac surface state in Bi2 Se3: A comparison of photoemission and Shubnikov-de Haas measurements. *Physical Review B - Condensed Matter and Materials Physics*, 81(20):205407, may 2010.

[100] J. Chen, H. J. Qin, F. Yang, J. Liu, T. Guan, F. M. Qu, G. H. Zhang, J. R. Shi, X. C. Xie, C. L. Yang, K. H. Wu, Y. Q. Li, and L. Lu. Gate-voltage control of chemical potential and weak antilocalization in bi_2se_3. *Phys. Rev. Lett.*, 105:176602, Oct 2010.

[101] Tobias Förster, Peter Krüger, and Michael Rohlfing. G W calculations for Bi 2 Te 3 and Sb 2 Te 3 thin films: Electronic and topological properties. *Physical Review B*, 93(20):205442, may 2016.

[102] T R Devidas, E P Amaladass, Shilpam Sharma, Awadhesh Mani, R Rajaraman, C S Sundar, and A Bharathi. Effect of sb substitution on the topological surface states in bi2se3single crystals: a magneto-transport study. *Materials Research Express*, 4(2):026101, feb 2017.

[103] A. Pertsova, C. M. Canali, and A. H. MacDonald. Quantum hall edge states in topological insulator nanoribbons. *Phys. Rev. B*, 94:121409(R), Sep 2016.

[104] K. Kuroda, M. Arita, K. Miyamoto, M. Ye, J. Jiang, A. Kimura, E. E. Krasovskii, E. V. Chulkov, H. Iwasawa, T. Okuda, K. Shimada, Y. Ueda, H. Namatame, and M. Taniguchi. Hexagonally Deformed Fermi Surface of the 3D Topological Insulator Bi 2 Se 3. *Physical Review Letters*, 105(7):076802, aug 2010.

[105] Helin Cao, Suyang Xu, Ireneusz Miotkowski, Jifa Tian, Deepak Pandey, M. Zahid Hasan, and Yong P. Chen. Structural and electronic properties of highly doped topological insulator Bi ₂ Se ₃ crystals. *physica status solidi (RRL) - Rapid Research Letters*, 7(1-2):133–135, feb 2013.

[106] Dong Xia Qu, Y. S. Hor, Jun Xiong, R. J. Cava, and N. P. Ong. Quantum oscillations and hall anomaly of surface states in the topological insulator Bi2Te3. *Science*, 329(5993):821–824, aug 2010.

[107] M. Nomura, S. Souma, A. Takayama, T. Sato, T. Takahashi, K. Eto, Kouji Segawa, and Yoichi Ando. Relationship between Fermi surface warping and out-of-plane spin polarization in topological insulators: A view from spin- and angle-resolved photoemission. *Physical Review B*, 89(4):045134, jan 2014.

[108] Liang Yang, Zhenhua Wang, Mingze Li, Xuan P. A. Gao, and Zhidong Zhang. The dimensional crossover of quantum transport properties in few-layered bi2se3 thin films. *Nanoscale Adv.*, 1:2303–2310, 2019.

[109] Yi Zhang, Ke He, Cui Zu Chang, Can Li Song, Li Li Wang, Xi Chen, Jin Feng Jia, Zhong Fang, Xi Dai, Wen Yu Shan, Shun Qing Shen, Qian Niu, Xiao Liang Qi, Shou Cheng Zhang, Xu Cun Ma, and Qi Kun Xue. Crossover of the three-dimensional topological insulator Bi 2 Se 3 to the two-dimensional limit. *Nature Physics*, 6(8):584–588, jun 2010.

[110] Karunya Shirali, William A. Shelton, and Ilya Vekhter. Inter-quintuple layer coupling and topological phase transitions in the chalcogenide topological insulators, feb 2022.

[111] Yoichi Ando. Topological insulator materials. *J. Phys. Soc. Jpn*, 82(10):102001, oct 2013.

[112] Wenliang Liu, Xiangyang Peng, Chao Tang, Lizhong Sun, Kaiwang Zhang, and Jianxin Zhong. Anisotropic interactions and strain-induced topological phase transition in Sb 2Se 3 and Bi 2Se 3. *Physical Review B - Condensed Matter and Materials Physics*, 84(24):245105, dec 2011.

[113] Wei Li, Xin Yuan Wei, Jian Xin Zhu, C. S. Ting, and Yan Chen. Pressure-induced topological quantum phase transition in Sb 2 Se 3. *Physical Review B - Condensed Matter and Materials Physics*, 89(3):035101, jan 2014.

[114] Junwei Liu, Yong Xu, Jian Wu, Bing Lin Gu, S. B. Zhang, and Wenhui Duan. Manipulating topological phase transition by strain. *Acta Crystallographica Section C: Structural Chemistry*, 70(2):118–122, jan 2014.

[115] Steve M Young, Sugata Chowdhury, Eric J Walter, Eugene J Mele, Charles L Kane, and Andrew M Rappe. Theoretical investigation of the evolution of the topological phase of Bi 2 Se 3 under mechanical strain. *PHYSICAL REVIEW B*, 84:85106, 2011.

[116] Achintya Bera, Koushik Pal, D. V.S. Muthu, Somaditya Sen, Prasenjit Guptasarma, U. V. Waghmare, and A. K. Sood. Sharp Raman anomalies and broken adiabaticity at a pressure induced transition from band to topological insulator in Sb2Se3. *Physical Review Letters*, 110(10):107401, mar 2013.

[117] Sudip Kumar Saha, Hrishit Banerjee, and Manoranjan Kumar. Topological transitions to Weyl states in bulk Bi2Se3: Effect of hydrostatic pressure and doping. *Journal of Applied Physics*, 129(8):085103, feb 2021.

[118] Thomas K. Reid, Sanjeev K. Nayak, and S. Pamir Alpay. Strain-induced surface modalities in pnictogen chalcogenide topological insulators. *Journal of Applied Physics*, 129(1):015304, jan 2021.

[119] Hyungjun Lee and Oleg V. Yazyev. Interplay between spin-orbit coupling and crystal-field effect in topological insulators. *Journal of Physics Condensed Matter*, 27(28):285801, jul 2015.

[120] Mathias Rosdahl Brems, Jens Paaske, Anders Mathias Lunde, and Morten Willatzen. Symmetry analysis of strain, electric and magnetic fields in the Bi2Se3-class of topological insulators. *New Journal of Physics*, 20(5):053041, may 2018.

[121] Joon Seok Kim, Rinkle Juneja, Nilesh P. Salke, Witold Palosz, Venkataraman Swaminathan, Sudhir Trivedi, Abhishek K. Singh, Deji Akinwande, and Jung Fu Lin. Structural, vibrational, and electronic topological transitions of Bi1.5Sb0.5Te1.8Se1.2 under pressure. *Journal of Applied Physics*, 123(11):115903, mar 2018.

[122] Paolo Giannozzi, Stefano Baroni, Nicola Bonini, Matteo Calandra, Roberto Car, Carlo Cavazzoni, Davide Ceresoli, Guido L Chiarotti, Matteo Cococcioni, Ismaila Dabo, Andrea Dal Corso, Stefano de Gironcoli, Stefano Fabris, Guido Fratesi, Ralph Gebauer, Uwe Gerstmann, Christos Gougoussis, Anton Kokalj, Michele Lazzeri, Layla Martin-Samos, Nicola Marzari, Francesco Mauri, Riccardo Mazzarello, Stefano Paolini, Alfredo Pasquarello, Lorenzo Paulatto, Carlo Sbraccia, Sandro Scandolo, Gabriele Sclauzero, Ari P Seitsonen, Alexander Smogunov, Paolo Umari, and Renata M Wentzcovitch. Quantum espresso: a modular and open-source software project for quantum simulations of materials. *Journal of Physics: Condensed Matter*, 21(39):395502 (19pp), 2009.

[123] P Giannozzi, O Andreussi, T Brumme, O Bunau, M Buongiorno Nardelli, M Calandra, R Car, C Cavazzoni, D Ceresoli, M Cococcioni, N Colonna, I Carnimeo, A Dal Corso, S de Gironcoli, P Delugas, R A DiStasio Jr, A Ferretti, A Floris, G Fratesi, G Fugallo, R Gebauer, U Gerstmann, F Giustino, T Gorni, J Jia, M Kawamura, H-Y Ko, A Kokalj, E Küçükbenli, M Lazzeri, M Marsili, N Marzari, F Mauri, N L Nguyen, H-V Nguyen, A Otero de-la Roza, L Paulatto, S Poncé, D Rocca, R Sabatini, B Santra, M Schlipf, A P Seitsonen, A Smogunov, I Timrov, T Thonhauser, P Umari, N Vast, X Wu, and S Baroni. Advanced capabilities for materials modelling with quantum espresso. *Journal of Physics: Condensed Matter*, 29(46):465901, 2017.

[124] Paolo Giannozzi, Oscar Baseggio, Pietro Bonfà, Davide Brunato, Roberto Car, Ivan Carnimeo, Carlo Cavazzoni, Stefano de Gironcoli, Pietro Delugas, Fabrizio Ferrari Ruffino, Andrea Ferretti, Nicola Marzari, Iurii Timrov, Andrea Urru, and Stefano Baroni. Quantum espresso toward the exascale. *The Journal of Chemical Physics*, 152(15):154105, 2020.

[125] T. L. Anderson and H. B. Krause. Refinement of the Sb_2Te_3 and Sb_2Te_2Se structures and their relationship to nonstoichiometric $Sb_2Te_{3-y}Se_y$ compounds. *Acta Crystallographica Section B*, 30(5):1307–1310, May 1974.

[126] Vei Wang, Nan Xu, Jin Cheng Liu, Gang Tang, and Wen Tong Geng. VASPKIT: A user-friendly interface facilitating high-throughput computing and analysis using VASP code. *Computer Physics Communications*, 267:108033, oct 2021.

[127] Uthpala Herath, Pedram Tavadze, Xu He, Eric Bousquet, Sobhit Singh, Francisco Muñoz, and Aldo H. Romero. Pyprocar: A python library for electronic structure pre/post-processing. *Computer Physics Communications*, 251:107080, 2020.

[128] N. P. Butch, K. Kirshenbaum, P. Syers, A. B. Sushkov, G. S. Jenkins, H. D. Drew, and J. Paglione. Strong surface scattering in ultrahigh-mobility Bi2 Se 3 topological insulator crystals. *Physical Review B - Condensed Matter and Materials Physics*, 81(24):241301, jun 2010.

[129] Rahul Singh, Aayush Sharma, Prashant Singh, Ganesh Balasubramanian, and Duane D. Johnson. Accelerating computational modeling and design of high-entropy alloys. *Nature Computational Science*, 1(1):54–61, jan 2021.

[130] L. Vegard. Die Konstitution der Mischkristalle und die Raumfüllung der Atome. *Zeitschrift für Physik*, 5(1):17–26, jan 1921.

[131] Zhiyi Chen, Lukas Zhao, Kyungwha Park, Thor Axtmann Garcia, Maria C. Tamargo, and Lia Krusin-Elbaum. Robust Topological Interfaces and Charge Transfer in Epitaxial Bi2Se3/II-VI Semiconductor Superlattices. *Nano Letters*, 15(10):6365–6370, oct 2015.

[132] R. Yoshimi, A. Tsukazaki, K. Kikutake, J. G. Checkelsky, K. S. Takahashi, M. Kawasaki, and Y. Tokura. Dirac electron states formed at the heterointerface between a topological insulator and a conventional semiconductor. *Nature Materials*, 13(3):253–257, feb 2014.

[133] D. K. Freeman, S. L. Mair, and Z. Barnea. The structure and Bijvoet ratios of cadmium selenide. *Acta Crystallographica Section A*, 33(3):355–359, may 1977.

[134] Quanqin Dai, Yanli Song, Dongmei Li, Haiyong Chen, Shihai Kan, Bo Zou, Yingnan Wang, Yongqiang Deng, Yuanyuan Hou, Shidan Yu, Lixue Chen, Bingbing Liu, and Guangtian Zou. Temperature dependence of band gap in CdSe nanocrystals. *Chemical Physics Letters*, 439(1-3):65–68, may 2007.

[135] L.A. Egorov and O.D. Torbova. Crystallization of solid solutions of in as1-x px from the gas phase. *Inorganic Materials*, 5:144–145, 1969.

[136] L. Pavesi, F. Piazza, A. Rudra, J. F. Carlin, and M. Ilegems. Temperature dependence of the InP band gap from a photoluminescence study. *Physical Review B*, 44(16):9052–9055, oct 1991.

[137] Luis C.O. Dacal and Andrs Cantarero. Ab initio electronic band structure calculation of InP in the wurtzite phase. *Solid State Communications*, 151(10):781–784, may 2011.

VITA

Karunya Shirali was born in Hyderabad, India. She lived in and did her schooling in Andhra Pradesh, India. In 2011, she joined the Indian Institute of Science Education and Research Thiruvananthapuram to pursue an Integrated BS-MS degree in Physics. Upon completion, she immediately joined a PhD program in 2016 at Louisiana State University, Baton Rouge. She worked in the field of theoretical condensed matter physics with Ilya Vekhter and William A. Shelton. She anticipates graduating in May 2022 and beginning a postdoctoral appointment at Virginia Tech.